Applications of Topology in Magnetic Fields

Mahboubeh Asgari-Targhi

Submitted for the degree of PhD

Supervisor: Prof Mitchell A. Berger
Department of Mathematics
University College London
Gower Street
London WC1E 6BT

April 2009

Declaration

I Mahboubeh Asgari-Targhi confirm that the work presented in this thesis is my own. Where information has been derived from other sources, I confirm that this has been indicated in the thesis.

Dedication

This thesis is dedicated to the memory of my father whose altruism, generosity and warmth have been my true inspiration in life. And to the memory of my sister who was a gift to my heart and a golden thread to the meaning of my life. Her kindness, affection, appreciation of life in her beautiful short life has taught me how to love. I am grateful to life for having known and love them as simply the best father and sister in the world.

Abstract

This thesis concerns applications of topology in magnetic fields. First, we examine the influence of writhe in the stretch-twist-fold dynamo. We consider a thin flux tube distorted by simple stretch, twist, and fold motions and calculate the helicity and energy spectra. The writhe number assists in the calculations, as it tells us how much the internal twist changes as the tube is distorted. In addition it provides a valuable diagnostic for the degree of distortion. Non mirror-symmetric dynamos typically generate magnetic helicity of one sign on large-scales and of the opposite sign on small-scales. The calculations presented here confirm the hypothesis that the large-scale helicity corresponds to writhe and the small-scale corresponds to twist. In addition, the writhe helicity spectrum exhibits an interesting oscillatory behaviour.

Second, we examine the effect of reconnection on the structure of a braided magnetic field. A prominent model for both heating of the solar corona and the source of small flares involves reconnection of braided magnetic flux elements. Much of this braiding is thought to occur at as yet unresolved scales, for example braiding of threads within an EUV or X-ray loop. However, some braiding may be still visible at scales accessible to Trace or the EIS imager on Hinode. We suggest that attempts to estimate the amount of braiding at these scales must take into account the degree of coherence of the braid structure. We demonstrate that simple models of braided magnetic fields which balance input of topological structure with reconnection evolve to a self-organized critical state. An initially random braid can become highly ordered, with coherence lengths obeying power law distributions. The energy released during reconnection also obeys a power law.

Acknowledgements

I would like to warmly thank my family for their absolute and unconditional love: my mother, my long winter night's companion during the writing up, for reciting Persian poetry (Rumi, Hafez) at "our breaks", for her fantastic sense of humour and for her heavenly cooking, the exquisite taste of some of her foods hopefully has enriched my thoughts for my research, she is the most wonderful and warm-hearted mother I could ever wish for, my darling sister Amene, the youngest child of our family, for bringing so much lights, love, happiness and laughter to our family, she is the extraordinary love we all needed so badly, dearest Masoud for being such a big-hearted, generous brother without him our family is meaningless, Amir for being so kind and funny, for making me laugh from miles away when we talk on the phone, Mahmoud for his playfulness, sarcasm and amazing ability to make one laugh even in sleep, Marzieh for being extremely kind and supportive and (annoyingly) getting things right when she shouldn't, she, as my grandfather used to say, shares my soul, we are one soul in two bodies, Mansoure and her beautiful family for being simply the loveliest and the most caring big sister one can think of, and again my parents for giving me seven superb siblings and best friends.

I am most grateful to Prof Berger for supervising this work, and for reading and correcting my draft. I am also immensely indebted to Dr Nick Ovenden for reading my draft with great precision.

I would also like to thank the following people. Ms Beverley Thompson for her warmth and for showing so much respect for learning. Father Ronald Fennel for being truly inspirational and optimistic, a rare trait in our today's world. Dr Alexander Voss for being a lovely brother in law (to be) and for providing me with technical assistance. And all my friends in particular Dr Hossein Lajevardi for his sympathy and support during my family tragedy that happened while studying for this research. Last but not least many thanks to Richard Hoyle, for his IT support.

Contents

List of Figures

List of Tables

Preface

This thesis considers the topology of magnetic field lines in solar dynamos and the solar atmosphere. We begin in chapter 1 by reviewing turbulence theory and magnetohydrodynamics (MHD). A description of the statistical quantities observed in MHD turbulence is presented in chapter 1 to give a tangible picture of the phenomena discussed in the rest of the thesis. The properties of magnetic field lines are also discussed using the idea of flux surfaces in MHD equilibrium.

In chapter 2, we review magnetic dynamos and their energetics. In sections 2.2-2.7, we describe large and small-scale dynamos as well as fast and slow dynamos and their energies. We proceed in sections 2.8-2.10 to review the stretch-twist-fold (STF) picture in solar dynamos. We investigate the influence of writhe in the STF process in chapter 3, where our model is a thin flux tube distorted by stretch, twist and fold motions. Section 3.2 reviews helicity, twist and writhe. In section 3.3, we calculate the magnetic field inside a twisted torus, followed by magnetic energy and magnetic helicity calculation for a thin tube. Numerical simulations concerning the behaviour of helicity in the STF picture are presented in section 3.4.

We review the structure of magnetic field lines in the solar corona in chapter 4. Sections 4.2-4.4 provide a review of a number of different models representing coronal loops and their energy transfer. In chapter 5 we review the trigger and energy release process of solar flares. The discussion in section 5.2 reviews the collision and reconnection of twisted magnetic flux tubes that result in solar flares before proceeding in section 5.3 to review the frequency distribution of solar flares. Chapter 6 examines the effect of reconnection on the structure of braided magnetic field. Sections 6.2-6.4 provide an estimate of braiding inside coronal loops. Section 6.5 presents a model of braided field lines in a self-organized critical state. A numerical model involving complex braiding pattern is given in section 6.6.

Chapter 1

A Survey of Turbulence Theory

1.1 Introduction

This chapter aims to give an overview of turbulence theory. Following this, we provide an overview of magnetohydrodynamics (MHD) and MHD turbulence that form the basis of our research in solar dynamo. We will primarily follow the treatments of Uriel Frisch [88] for turbulence theory, and Glenn Bateman [22] for MHD.

The equations used to describe the behaviour of an incompressible fluid in a flow are the Navier-Stokes equations:

$$\partial_t v_i + v_j \, \partial_j v_i = -\partial_i p + \nu \, \partial_{jj} v_i, \tag{1.1}$$

$$\partial_i v_i = 0. \tag{1.2}$$

Equation (1.2) describes the velocity field v divergence free condition and p and ν are the pressure and the viscosity respectively. The above equations are sufficient to describe many turbulent flows; however it is important to look at experimental data and numerical simulations in order to find out the consequences of the equations.

For a given geometrical shape of the boundaries, the Reynolds number is the only control parameter of the flow and is defined as

$$R = \frac{Lv}{\nu}, \tag{1.3}$$

where L and v are the characteristic scale and velocity of the flow, and ν is the kinematic viscosity. Similar equations for magnetic Reynolds number are defined in chapter (2).

Table 1.1: Typical Reynolds numbers for various flows.

	$L[m]$	$v[ms^{-1}]$	$\nu[m^2s^{-1}]$	R
Flow past wing of a Jumbo jet	3	200	1.5×10^{-5}	4×10^7
Moving a finger through water	10^{-2}	3×10^{-2}	10^{-6}	3×10^2
Spin-down of a stirred cup of tea	5×10^{-2}	10^{-1}	10^{-6}	5×10^3
Glycerine draining from a spoon	3×10^{-2}	10^{-2}	1.8×10^{-3}	2×10^{-1}

Table 1.1 provides a summary of Reynolds numbers for various flows. There typically exists a Reynolds number threshold beyond which the flow becomes chaotic in its time-dependence.

1.2 Symmetries and Turbulence

Symmetry considerations are central to the study of the transition phenomena and fully developed turbulence. Here, we give a brief review of symmetry in turbulence theory by Frisch [88]. Consider a flow of uniform velocity $\mathbf{v} = (v, 0, 0)$ (at infinity), parallel to the x-axis, incident from the left on an infinite cylinder, of circular cross-section with diameter L where the axis is along the z-direction and the boundary conditions are fixed (figure 1.1). This flow has the following symmetries:
Left-right (x-reversal),
Up-down (y-reversal),
Time-translation (t-invariance),
Space-translation parallel to the axis of the cylinder (z-invariance).

All of the above symmetries, except the first, are consistent with the Navier-Stokes equations and the boundary conditions. To be more specific, consider the velocity field with components (u, v, w). The left-right symmetry is

$$(x, y, z) \to (-x, y, z), \quad (u, v, w) \to (-u, v, w), \tag{1.4}$$

and the up-down symmetry is

$$(x, y, z) \to (x, -y, z), \quad (u, v, w) \to (u, -v, w). \tag{1.5}$$

The left-right symmetry $(x, y, z) \to (-x, y, z)$ is not consistent in this case with the Navier-Stokes equations. However it is consistent with the Stokes equation for slow viscous flow which is obtained by dropping the non-linear term and time derivative in the Navier-Stokes equations

$$0 = -\partial_i p + \nu\, \partial_{jj} v_i, \qquad \partial_i v_i = 0. \tag{1.6}$$

A symmetry is spontaneously broken if it is consistent with the equations of motion and the boundary conditions, but is not present in the solution. As the Reynolds number is increased, the various symmetries permitted by the equations (Navier-Stokes or Stokes) and the boundary conditions are broken. However, at very high Reynolds number the symmetries are restored in a statistical sense far from the boundaries. Fully developed turbulence occurs when at very high Reynolds numbers, all or some of the possible symmetries are restored in a statistical sense. For this to happen, the flow should not be subjected to any constraint such as a long-scale shear, which would prevent it from accepting all possible symmetries.

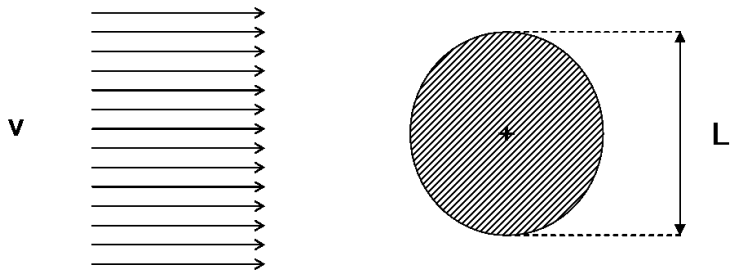

Figure 1.1: Uniform flow with velocity $\mathbf{v}$, incident on a cylinder of diameter L.

1.2.1 Periodic Boundary Conditions

To achieve maximum symmetry, it is useful not to have any boundaries. However, since the unboundedness of the space leads to mathematical difficulties, we assume periodic boundary conditions in the space variable $\mathbf{r} = (x, y, z)$:

$$\mathbf{v}(x + nL, y + mL, z + qL) = \mathbf{v}(x, y, z), \tag{1.7}$$

for all x, y, z and the integers m, n, q. The positive real number L is called the period. It is then possible to consider the restriction of the flow to a periodic box such as $\mathbf{B}_L : 0 \leq x < L$, $0 \leq y < L$, $0 \leq z < L$ (figure 1.2) with the the case of a fluid in unbounded space R^3 obtained by letting $L \to \infty$. The space of L-periodic boundary functions $\mathbf{v}(\mathbf{r})$ satisfying $\nabla \cdot \mathbf{v} = 0$ is denoted by $\mathcal{H}$.

Let $\mathbf{G}$ denote a group of transformations acting on space-time functions $\mathbf{v}(t, \mathbf{r})$, that are spatially periodic and divergence-free. $\mathbf{G}$ is a symmetry group of the Navier-Stokes equations if, for all $\mathbf{v}$ that are solutions of the Navier-Stokes equations, and for all $g \in \mathbf{G}$, the function $g\mathbf{v}$ is also a solution. Here is a list of known symmetries of the Navier-Stokes equations:

- Space-translations g_ρ^{space}: $(\mathrm{t}, \mathbf{r}, \mathbf{v}) \longmapsto (t, \quad \mathbf{r} + \rho, \mathbf{v}) \quad \rho \in R^3$.

- Time-translations g_τ^{time}: $(\mathrm{t},\, \mathbf{r},\, \mathbf{v}) \longmapsto (t+\tau,\, \mathbf{r}, \mathbf{v}) \quad \tau \in R$.
- Galilean transformations $g_{\mathbf{U}}^{Gal} : (t, \mathbf{r}, \mathbf{v}) \longmapsto (t, \mathbf{r} + \mathbf{U}\, t, \mathbf{v} + \mathbf{U}) \quad \mathbf{U} \in R^3$.
- Parity $\mathbf{P} : (t, \mathbf{r}, \mathbf{v}) \longmapsto (t, -\mathbf{r}, -\mathbf{v})$.
- Rotations $g_A^{rot} : (t, \mathbf{r}, \mathbf{v}) \longmapsto (t, A\mathbf{r}, A\mathbf{v}) \quad \mathrm{A} \in \mathrm{SO}(R^3)$ (three dimensional rotation group) but not in T^3 ($T^3 = 3$ - torus).
- Scaling $g_\lambda^{scal} : (t, \mathbf{r}, \mathbf{v}) \longmapsto (\lambda^{1-h} t, \lambda\mathbf{r}, \lambda^h \mathbf{v}) \quad \lambda \in R_+,\, h \in R$.

The space and time-translation symmetries are obvious. In the Galilean transformations, we substitute $\mathbf{v}(t, \mathbf{r} - \mathbf{U}t) + \mathbf{U}$ for $\mathbf{v}(t, \mathbf{r})$, and there is a cancellation of terms between $\partial_t \mathbf{v}$ and $\mathbf{v} \cdot \nabla \mathbf{v}$.

Under parity, all the terms in the Navier-Stokes equations change sign (in particular $\nabla \longmapsto -\nabla$). The symmetry $\mathbf{v} \longmapsto -\mathbf{v}$ is not consistent with the equations, except when the non-linear term is negligible. Continuous rotational invariance is not consistent with periodic boundary conditions, since the latter singles out certain directions. For the scaling transformations, when t is changed into $\lambda^{1-h}t$, $\mathbf{r}$ into $\lambda\mathbf{r}$, and $\mathbf{v}$ into $\lambda^h \mathbf{v}$, all the terms in the Navier-Stokes equations are multiplied by λ^{2h-1}, except the viscous term which is multiplied by λ^{h-2}. Therefore for finite viscosity, only $h = -1$ is permitted. The corresponding symmetry is then equivalent to the well-known similarity principle of fluid dynamics, since the scaling transformations must keep the Reynolds number unchanged. If the viscous term is ignored or if it tends to zero, as it may be justified at very high Reynolds numbers, then there are infinitely many scaling groups, labelled by their scaling exponent h, which can be any real number.

We finally note that all the listed symmetries, except the scaling symmetries are just macroscopic consequences of the basic symmetries of Newton's equations governing microscopic molecular motion. The pressure can be eliminated from the Navier-Stokes equations in a number of ways. Firstly we have

$$\partial_i \left(v_j\, \partial_j v_i\right) = \partial_{ij} \left(v_i v_j\right) = -\partial_{ii} p = -\nabla^2 p, \tag{1.8}$$

which is an instance of the Poisson equation:

$$\nabla^2 p = \sigma. \tag{1.9}$$

The Poisson equation can be solved within the class of L-periodic functions provided that $\sigma(\mathbf{r})$ has a vanishing average:

$$\langle \sigma \rangle = \frac{1}{L^3} \int_{B_L} \sigma(\mathbf{r}) \mathrm{d}\mathbf{r} = 0. \tag{1.10}$$

The function, $\sigma = -\partial_{ij}(v_i v_j)$, being composed of space-derivatives of periodic functions, satisfies (1.10).

The solution of the Poisson equation can be found by going from the physical space (**r**-space) to the Fourier space (**k**-space), using Fourier transforms. Let

$$\sigma(\mathbf{r}) = \sum_k e^{\mathrm{i}\mathbf{k}\cdot\mathbf{r}}\,\hat{\sigma}_{\mathbf{k}}, \quad \mathbf{k} \in \frac{2\pi}{L}\mathbf{Z}^3, \tag{1.11}$$

$$p\,(\mathbf{r}) = \sum_k e^{\mathrm{i}\mathbf{k}\cdot\mathbf{r}}\,\hat{p}_{\mathbf{k}}, \tag{1.12}$$

where $\mathbf{Z}$ is the set of signed integers and the Fourier coefficients are given by

$$\hat{\sigma}_{\mathbf{k}} = \left\langle e^{-\mathrm{i}\mathbf{k}\cdot\mathbf{r}}\sigma(\mathbf{r})\right\rangle, \tag{1.13}$$

$$\hat{p}_{\mathbf{k}} = \left\langle e^{-\mathrm{i}\mathbf{k}\cdot\mathbf{r}}p(\mathbf{r})\right\rangle. \tag{1.14}$$

According to (1.10), σ_0 vanishes and from (1.9), we have

$$\hat{p}_{\mathbf{k}} = -\frac{\hat{\sigma}_{\mathbf{k}}}{\mathrm{k}^2} \quad \mathrm{k} \neq 0, \tag{1.15}$$

where k is the modulus of the wave-vector $\mathbf{k}$. The coefficient $\hat{p}_0$ is arbitrary. The solution of the Poisson equation is defined up to an additive constant. Adding this constant to the pressure does not change the Navier-Stokes equations. This solution will be denoted in the physical space as $\nabla^{-2}\sigma$. In physical space, this is a non-local operator. After eliminating the pressure by solving the Poisson equation and using

$$\partial_l\,\nabla^{-2} = \nabla^{-2}\,\partial_l, \tag{1.16}$$

we write the Navier-Stokes equation as

$$\partial_t v_i + (\delta_{il} - \partial_{il}\nabla^{-2})\partial_j(v_j\,v_l) = \nu\nabla^2 v_i. \tag{1.17}$$

It is now sufficient to impose the divergence condition $\partial_j v_j = 0$ at $t = 0$, since (1.17) will propagate this condition at all times.

Another way to eliminate the pressure is to use the definition of vorticity

$$\underline{\omega} = \nabla \wedge \mathbf{v}. \tag{1.18}$$

From taking the curl of the Navier-Stokes equation (1.1), and using the identity $\nabla v^2 = 2\mathbf{v}\cdot\nabla\mathbf{v} + 2\mathbf{v}\wedge(\nabla\wedge\mathbf{v})$, the vorticity is obtained as follows

$$\partial_t\underline{\omega} = \nabla\wedge(\mathbf{v}\wedge\underline{\omega}) + \nu\nabla^2\underline{\omega}. \tag{1.19}$$

In order to rewrite (1.19) in terms of the vorticity field only, we solve (1.18) for the velocity. This is done by taking the curl of (1.18) and solving the resulting Poisson equation. Thus, the same non-local operator ∇^{-2} appears as in the velocity formalism of (1.17).

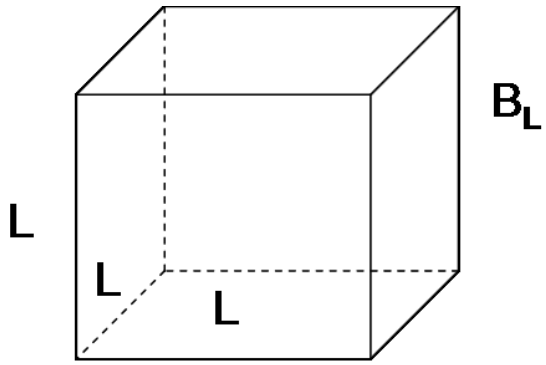

Figure 1.2: The periodic box.

1.2.2 Laws of Conservation

The conservation laws are usually discussed with symmetries. Noether's theorem [163] gives a rationale for this association. This theorem states that for each symmetry there is a corresponding conservation law. For example, momentum conservation corresponds to the invariance of the Lagrangian under space-translations.

Here, we discuss the global conservation laws. These involve an integration over the whole volume occupied by the fluid. Consider an arbitrary periodic function $f(\mathbf{r})$ described over a fundamental periodicity box:

$$\langle f \rangle \equiv \frac{1}{L^3} \int_{B_L} f(\mathbf{r}) \mathrm{d}\mathbf{r}, \tag{1.20}$$

where $f(\mathbf{r})$ is an arbitrary periodic function. First, we list some useful identities of functions that are periodic.

$$\langle \partial_i f \rangle = 0. \tag{1.21}$$

$$\langle (\partial_i f) g \rangle = - \langle f \partial_i g \rangle . \tag{1.22}$$

$$\left\langle (\nabla^2 f) g \right\rangle = - \langle (\partial_i f)(\partial_i g) \rangle . \tag{1.23}$$

$$\langle \mathbf{u} \cdot (\nabla \wedge \mathbf{v}) \rangle = \langle (\nabla \wedge \mathbf{u}) \cdot \mathbf{v} \rangle . \tag{1.24}$$

$$\left\langle \mathbf{u} \cdot \nabla^2 \mathbf{v} \right\rangle = - \left\langle (\nabla \wedge \mathbf{u}) \cdot (\nabla \wedge \mathbf{v}) \right\rangle, \quad \text{if } \nabla \cdot \mathbf{v} = 0. \tag{1.25}$$

We list the main known conservation laws as:
Conservation of momentum (space translation symmetry)

$$\frac{\mathrm{d}}{\mathrm{d}t} \langle \mathbf{v} \rangle = 0. \tag{1.26}$$

Conservation of energy (time translation symmetry)

$$\frac{\mathrm{d}}{\mathrm{d}t} \left\langle \frac{1}{2} v^2 \right\rangle = -\frac{1}{2} \nu \left\langle \sum_{ij} (\partial_i v_j + \partial_j v_i)^2 \right\rangle = -\nu \left\langle \left| \underline{\omega}^2 \right| \right\rangle = 0, \tag{1.27}$$

where $\underline{\omega} = \nabla \wedge \mathbf{v}$.
Conservation of helicity (Moreau [158] gives a complicated symmetry ; translation along vortex direction)

$$\frac{\mathrm{d}}{\mathrm{d}t} \left\langle \frac{1}{2} \mathbf{v} \cdot \underline{\omega} \right\rangle = -\nu \left\langle \underline{\omega} \cdot \nabla \wedge \underline{\omega} \right\rangle = 0. \tag{1.28}$$

We now introduce some important notations:

$$E \equiv \left\langle \frac{1}{2} |\mathbf{v}|^2 \right\rangle, \quad \Omega \equiv \left\langle \frac{1}{2} |\underline{\omega}|^2 \right\rangle, \tag{1.29}$$

$$H \equiv \left\langle \frac{1}{2} \mathbf{v} \cdot \underline{\omega} \right\rangle, \quad H_\omega = \left\langle \frac{1}{2} \underline{\omega} \cdot \nabla \wedge \underline{\omega} \right\rangle. \tag{1.30}$$

Also, the energy and helicity balance equations may be written as:

$$\frac{\mathrm{d}}{\mathrm{d}t} E = -2\nu \, \Omega, \quad \frac{\mathrm{d}}{\mathrm{d}t} H = -2\nu H_\omega, \tag{1.31}$$

where we consider E as the mean energy per unit mass, H the mean kinetic helicity, Ω the mean enstrophy and H_ω is the mean vortical helicity. The mean energy dissipation per unit mass

$$\epsilon \equiv -\frac{\mathrm{d}E}{\mathrm{d}t}, \tag{1.32}$$

is one of the most frequently used quantities in turbulence.

1.2.3 Energy Scale

We start by introducing another energy balance equation

$$\frac{\mathrm{d}}{\mathrm{d}t} \Omega = -2\nu P, \qquad P \equiv \left\langle \frac{1}{2} |\nabla \wedge \underline{\omega}|^2 \right\rangle, \tag{1.33}$$

where P is called the mean palinstrophy, Ω the mean enstrophy and $\underline{\omega}$ as introduced earlier is vorticity. Equation (1.33) does not have any contribution from non-linear terms in the Navier-Stokes equations. The important question is then: what is the role of non-linearities in relation to the energy? We show in this section that the non-linear term redistributes energy among various scales of motion without affecting the global energy budget. In a similar manner, the non-linear term in the MHD equations (section 1.4) redistributes magnetic helicity and energy among various scales [192]. For that we need a definition for the concept of scale. As an example, consider figure 1.3, and imagine it is shown using an overhead projector somewhat out of focus. It is obvious that the finest details will be blurred. Defocusing amounts approximately to a linear filtering which removes or attenuates high harmonics in the spatial Fourier decomposition of the image above a cut-off K which depends on the defocusing. There is an associated scale $l \sim K^{-1}$ over which there is smoothing. This can be formalized if we restrict ourselves to L-periodic functions. Given a function f and its Fourier series

$$f(\mathbf{r}) = \sum_k \hat{f}_k \, e^{\mathrm{i}\mathbf{k}\cdot\mathbf{r}}, \qquad \mathbf{k} \in \frac{2\pi}{L}\mathbf{Z}^3, \tag{1.34}$$

there are two families of functions depending on $\mathbf{r}$ and on the additional parameter $K > 0$. One is the low-pass filtered function

$$f_K^<(\mathbf{r}) \equiv \sum_{k \le K} \hat{f}_k \, e^{\mathrm{i}\mathbf{k}\cdot\mathbf{r}}, \tag{1.35}$$

and the other is the high-pass filtered function

$$f_K^>(\mathbf{r}) \equiv \sum_{k > K} \hat{f}_k \, e^{\mathrm{i}\mathbf{k}\cdot\mathbf{r}}. \tag{1.36}$$

The length $l = K^{-1}$ is the scale of filtering. Also

$$f(\mathbf{r}) = f_K^<(\mathbf{r}) + f_K^>(\mathbf{r}), \tag{1.37}$$

where $f^<$ and $f^>$ are known as f 'lesser' and f 'greater' respectively. Using the above definitions, we describe the magnetic field in terms of its Fourier transform in section 3.2.2. To illustrate the idea of low/high pass filtering, consider the example of a one-dimensional function (figure 1.4). The function possesses structures on two very different scales: a small-scale (of the order of a few millimetres) and a large-scale (of the order of a few centimetres). Choose $l = K^{-1}$ to be 1cm. The corresponding low- and high-pass functions are shown in figures 1.4(b) and 1.4(c).

It is important to note that $f_K^<(\mathbf{r})$ and $f_K^>(\mathbf{r})$ are not Fourier transforms of $f(\mathbf{r})$: they depend on the same space variable $\mathbf{r}$ as $f(\mathbf{r})$ and they also depend on an additional scale variable.

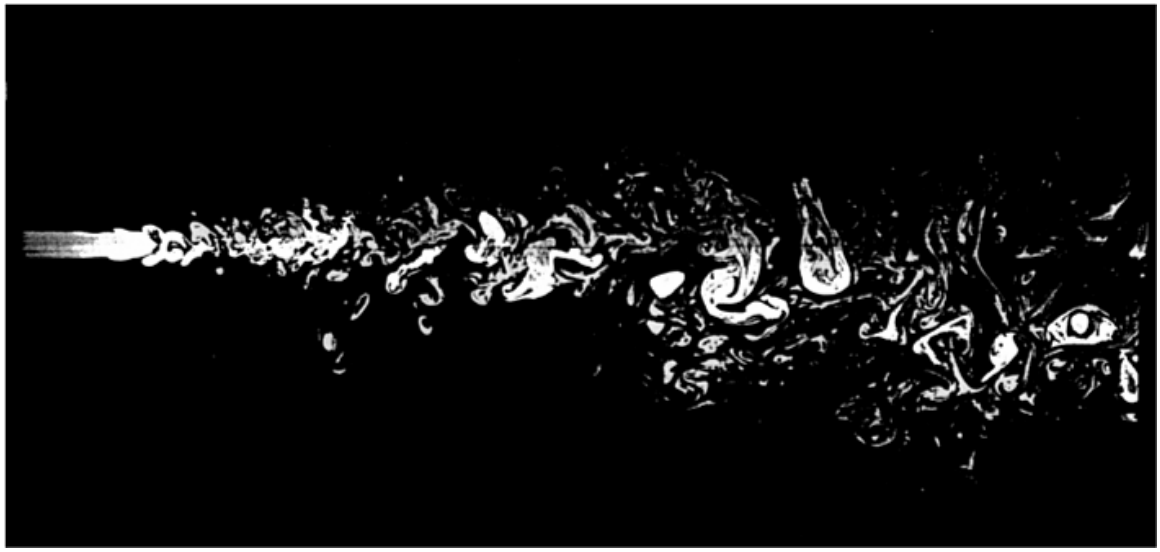

Figure 1.3: Turbulent water jet (Van Dyke 1982). Photograph P. Dimotakis, R. Lye and D. Papantoniou.

When the concept of filtering is applied to a three-dimensional turbulent velocity field, two functions $\mathbf{v}_K^<(\mathbf{r})$ and $\mathbf{v}_K^>(\mathbf{r})$ are obtained. The former is described as eddies of scale larger than l and the latter as eddies of scale less than l. Additional properties of filtering are presented in Appendix A.

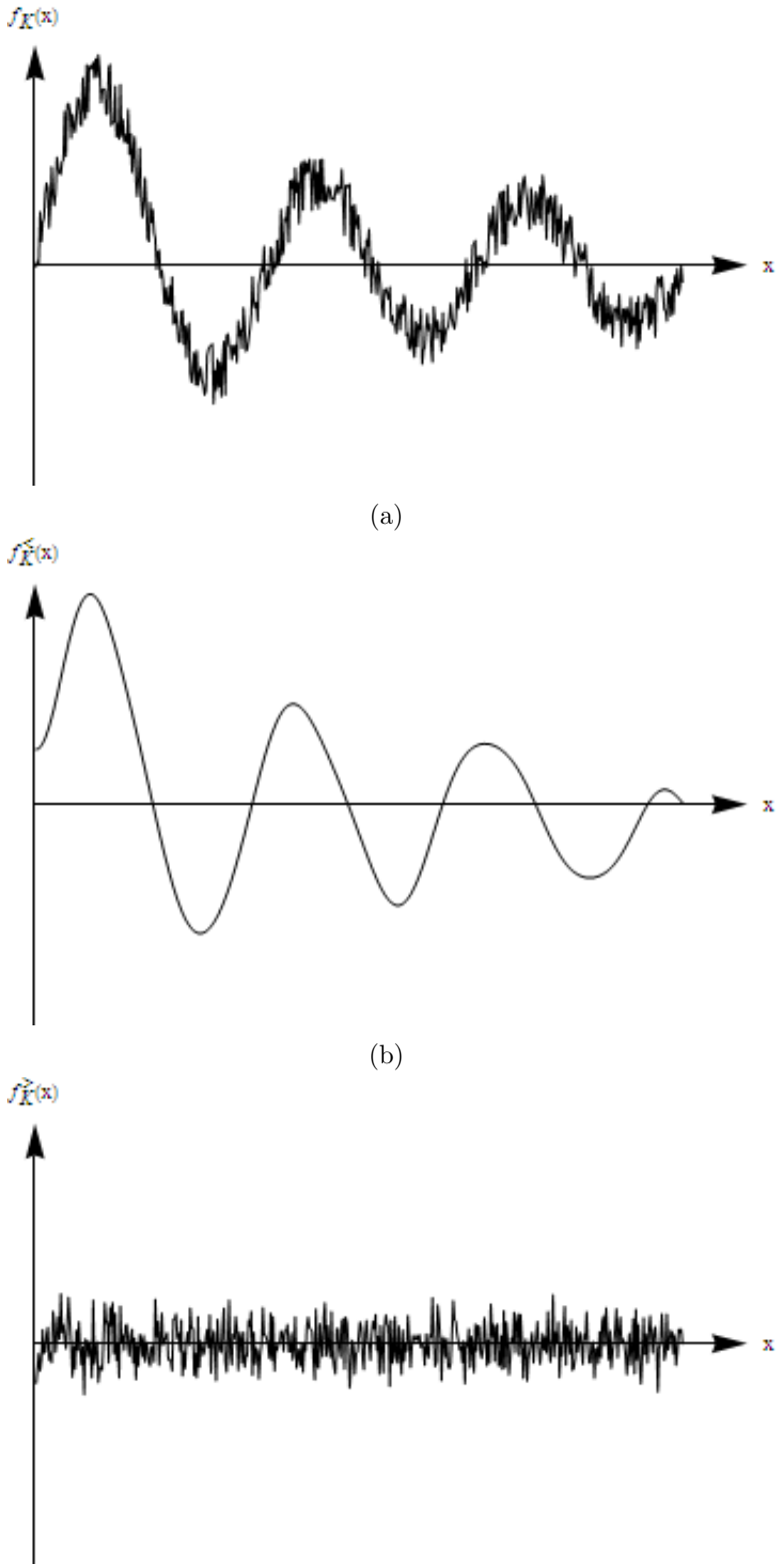

Figure 1.4: Signal (a) subject to low-pass filtering (b) and high-pass filtering (c).

1.3 The Kolmogorov Theory

There are two laws established by experiment of the fully developed turbulence:
1. Two-thirds law:
In a turbulent flow at very high Reynolds number, the mean square velocity increment $\langle(\delta v(l))^2\rangle$ between two points separated by a distance l behaves approximately as the two-thirds power of the distance.
2. Law of finite energy dissipation:
If, in an experiment on turbulent flow, all the control parameters are kept the same, except for viscosity, which is lowered as much as possible, the energy dissipation per unit mass $\mathrm{d}E/\mathrm{d}t$ behaves in a way consistent with a finite positive limit.

There is currently no fully deductive theory that starts from the Navier-Stokes equations and leads to the two basic experimental laws stated above. However, it is still possible to formulate hypotheses, compatible with these laws that results in leading to additional predictions. This was the purpose of the Kolmogorov 1941 theory (in short **K41**). In the next section, we emphasize on postulated symmetries.

Forcing Terms

Kolmogorov assumes a freely decaying turbulent flow in his 1941 paper on the four-fifths law. In order to maintain 'Realistic turbulence', mechanisms used are the interaction of an incoming flow with boundaries, thermal convective instability, etc. The inhomogeneities induced by the maintaining mechanism may be weak enough to be partially ignored at small-scales and far from boundaries. To renew the energy dissipated by viscosity, a simple device is to add a forcing term $\mathbf{f}(t,\mathbf{r})$ in the Navier-Stokes equations:

$$\begin{aligned} \partial_t \mathbf{v} + \mathbf{v}\cdot\nabla\mathbf{v} &= -\nabla p + \nu\nabla^2\mathbf{v} + \mathbf{f}, \\ \nabla\cdot\mathbf{v} &= 0. \end{aligned} \tag{1.38}$$

The 'stirring force' is assumed to be active only at large-scales, so as to model the mechanism of production of turbulence which often involves some large-scale instability [76, 77]. The random force $\mathbf{f}(t,\mathbf{r})$ is considered to be stationary and homogeneous, i.e. its statistical properties are invariant under translations in time and space. Also the solution of the Navier-Stokes equations is assumed to be homogeneous, but not necessarily stationary, so as to cover instances where the external force vanishes. And finally we consider that all moments required in subsequent manipulations are finite as long as $\nu > 0$.

We define $\epsilon(\mathbf{l})$ as

$$\epsilon(\mathbf{l}) \equiv -\partial_t \frac{1}{2} \langle \mathbf{v}(\mathbf{r}) \cdot \mathbf{v}(\mathbf{r}+\mathbf{l}) \rangle |_{NL}, \tag{1.39}$$

where the notation $\partial_t(.)|_{NL}$ stands for 'contribution to the time-rate-of-change stemming from the non-linear terms (advection and pressure) in the Navier-Stokes equations' [88]. $\epsilon(\mathbf{l})$ has the dimension of a time-rate-of-change of an energy per unit mass and will be called the physical-space energy flux.

1.3.1 Kolmogorov 1941 and Symmetries

In section 1.2 we made a list of known symmetries for the Navier-Stokes equations (time -and space-translations, rotations, Galilean transformations, scaling transformations, etc). Here, we investigate their implications for turbulence.

First consider time-translations. For a laminar flow, at low Reynolds numbers, if the boundary conditions and any external driving force are time-independent, the flow is steady and therefore does not break the time-invariance symmetry. When we increase the Reynolds number, bifurcation may occur. This makes the flow time-periodic and results in turning the continuous time-invariance symmetry into a discrete one. Once the Reynolds number is increased further the flow will eventually at some point, become chaotic. The continuous time-invariance symmetry is then restored, not for individual solutions but at the level of the invariant measure of the dynamical system.

It is important to see if this result can be extended to other symmetries of the Navier-Stokes equations. Consider, for example, the invariance under space-translations. The difficulty associated with this case is, in instances where the turbulence is generated by flow around a rigid body such as a cylinder. The presence of the cylinder will trivially break the translation symmetry and the root mean square (r.m.s.) velocity fluctuations at the point very close to the cylinder cannot be the same as at the point somewhere in the wake, since the velocity and its fluctuations must vanish at rigid boundaries. Therefore such a turbulent flow can never be strictly homogeneous (i.e. statistically invariant under space-translations). However, it is possible to develop discrete translation-invariance if the bodies generating the turbulence are arranged in a spatially periodic fashion, such as for the flow past a grid. The geometry of the flow is preserved by translations parallel to the grid by a multiple of the mesh. This leaves the flow invariant as long as the Reynolds number is sufficiently low. As the Reynolds number is increased and the flow becomes turbulent, its statistical properties will be invariant under such translations.

The same can be said about all the other symmetries of the Navier-Stokes equations where one can conclude that the mechanisms responsible for the generation of the turbulent flow are usually not consistent with most of the possible symmetries presented in section 1.2. However, the qualitative aspect of many turbulent flows suggests some form of homogeneity, isotropy and possibly scale-invariance. The power law behaviour of the second order structure function resulting from Kolmogorv's two-thirds law (section 1.3) is an indication of some form of scale invariance. We will discuss power law distribution of solar flares in chapters 5 and 6.

The following hypothesis will help to reconcile some of the conflicting aspects of symmetries of Navier-Stokes equations.

H1 In the limit of infinite Reynolds number, all possible symmetries of the Navier-Stokes equations, usually broken by the mechanisms producing the turbulent flow, are restored in a statistical sense at small-scales and away from boundaries.

Small-scales are scales of $l \ll l_0$ where l_0, the integral scale, is characteristic of the production of turbulence. Small-scale homogeneity is considered to be the property of having homogeneous increments, i.e. in terms of velocity increments:

$$\delta\mathbf{v}(\mathbf{r},\mathbf{l}) \equiv \mathbf{v}(\mathbf{r}+\mathbf{l}) - \mathbf{v}(\mathbf{r}). \tag{1.40}$$

It is assumed that

$$\delta\mathbf{v}(\mathbf{r}+\rho,\mathbf{l}) = \delta\mathbf{v}(\mathbf{r},\mathbf{l}), \tag{1.41}$$

for all increments $\mathbf{l}$ and all displacements ρ which are small compared to the integral scale.

In this context by isotropy, we mean that the statistical properties of velocity increments are invariant under simultaneous rotations of $\mathbf{l}$ and $\delta\mathbf{v}$. For parity, $\mathbf{l}$ and $\delta\mathbf{v}$ can be reversed simultaneously.

H2 Under the same assumptions as in **H1**, the turbulent flow possesses a unique scaling exponent h, i.e. it is self-similar at small-scales. This is what is needed to describe the scale-invariance since there are infinitely many scaling groups which depend on the choice of the scaling exponent h. Therefore, there exists a scaling exponent $h \in R$ such that

$$\delta\mathbf{v}(\mathbf{r},\lambda\mathbf{l}) = \lambda^h \delta\mathbf{v}(\mathbf{r},\mathbf{l}), \qquad \forall\lambda \in R_+, \tag{1.42}$$

for all $\mathbf{r}$ and all increments $\mathbf{l}$ and $\lambda\mathbf{l}$ small compared to the integral scale.

As described below, the unique scaling exponent h in Kolmogorov's four-fifths law is equal to 1/3.

H3 Under the same assumptions as in **H1**, the turbulent flow has a finite non-vanishing mean rate of dissipation ϵ per unit mass. For **H3**, the integral scale l_0 and the r.m.s velocity fluctuations v_0 are fixed and $\nu \to 0$. Otherwise, ϵ must be non-dimensionalised through division by v_0^3/l_0.

It is important to mention that in his 1941 paper, Kolmogorov postulated the following hypothesis which is quite different from the hypotheses listed so far and is described thus:

Kolmogorov's second universality assumption

In the limit of infinite Reynolds number, all the small-scale statistical properties are uniquely and universally determined by scale l and the mean energy dissipation rate ϵ. The first universality assumption of Kolmogorov will be described in section 1.3.4.

To illustrate the universality assumption clearly, consider the second-order structure function $\langle(\delta\mathbf{v}(l))^2\rangle$. Simple dimensional analysis shows that this quantity has dimensions $[L]^2[T]^{-2}$, where $[L]$ and $[T]$ are units of length and time. Since the mean energy dissipation rate per unit mass ϵ, has the dimensions $[L]^2[T]^{-3}$, it follows from the universality assumption that

$$\left\langle(\delta\mathbf{v}(l))^2\right\rangle = C\epsilon^{2/3}\, l^{2/3}, \tag{1.43}$$

where C is a universal dimensionless constant. Also, by the Hypothesis **H2**, the second order structure function should be proportional to l^{2h}. Hence $h = 1/3$ is the only consistent value.

Kolmogorov's four-fifths law

Kolmogorov found in his 1941 turbulence paper how an exact relation can be derived for the third-order longitudinal structure function which is the average of the cube of the longitudinal velocity increment. His assumptions were homogeneity, isotropy and hypothesis **H3** about the finiteness of the energy dissipation. He obtained the following result from the Navier-Stokes equations without any further assumptions:

Four-fifths law: In the limit of infinite Reynolds number, the third-order (longitudinal) structure function of homogeneous isotropic turbulence, evaluated for increments l small compared to the integral scale, is given in terms of the mean energy dissipation per unit mass ϵ by

$$\left\langle (\delta v_{\parallel}(\mathbf{r},\mathbf{l}))^3 \right\rangle = -\frac{4}{5}\,\epsilon l, \tag{1.44}$$

where ϵ is assumed to remain finite and non-vanishing. The above equation is one of the most important results in fully developed turbulence. Uriel Frisch [88] calls this a 'boundary condition' on theories of turbulence: for these theories to be acceptable, they must either satisfy the four-fifths law, or explicitly violate the assumptions made in deriving it. There is not much detail in Kolmogorov's derivation of the four-fifths law since he used a previously derived relation of Kármán and Howarth [116].

1.3.2 The Energy Flux for Homogeneous Turbulence

The starting point here is the scale-by-scale energy budget equation (A.11) which relates the (mean) cumulative energy ζ_K, the (mean) cumulative enstrophy Ω_K, the (mean) cumulative energy injection $\mathcal{F}_K$ and the (mean) energy flux Π_K. Here, we use random homogeneous functions rather than periodic functions. The Fourier series used in Section 1.2.3 to define filtering is replaced by Fourier integrals. For instance, the low-pass filtered velocity $\mathbf{v}_K^<$ is related to the velocity field $\mathbf{v}$ and its Fourier transform $\hat{\mathbf{v}}$ by the following relations

$$\begin{aligned}
\mathbf{v}(\mathbf{r}) &= \int_{R^3} \mathrm{d}^3k\, e^{\mathrm{i}\mathbf{k}\cdot\mathbf{r}}\hat{\mathbf{v}}_k, \\
\hat{\mathbf{v}}_k &= \frac{1}{(2\pi)^3}\int_{R^3} \mathrm{d}^3\mathbf{r}\, e^{-\mathrm{i}\mathbf{k}\cdot\mathbf{r}}\mathbf{v}(\mathbf{r}), \\
\mathbf{v}_K^<(\mathbf{r}) &= \int_{|k|\le K} \mathrm{d}^3k\, e^{\mathrm{i}\mathbf{k}\cdot\mathbf{r}}\,\hat{\mathbf{v}}_k.
\end{aligned} \tag{1.45}$$

Angular brackets are interpreted as ensemble averages rather than spatial averages over the periodicity box. With this reinterpretation, all the results from Section 1.2.3 remain literally true.

For convenience, the scale-by-scale energy budget relation (A.11) is written as

$$\partial_t \zeta_K + \Pi_K = \mathcal{F}_K - 2\nu\Omega_K, \tag{1.46}$$

and the energy flux through wave-number K is expressed in terms of third order velocity moments by

$$\Pi_K = -\frac{1}{8\pi^2}\int_{R^3} \mathrm{d}^3l\, \frac{\sin(Kl)}{l}\,\nabla_l \cdot \left[\frac{\mathbf{l}}{l^2}\nabla_l \cdot \left\langle |\delta\mathbf{v}(\mathbf{l})|^2\,\delta\mathbf{v}(\mathbf{l})\right\rangle\right]. \tag{1.47}$$

The energy flux through wave-number K is expressed in terms of the third-order longitudinal structure function $S_3(l) = \left\langle (\delta v_\parallel(\mathbf{r}, \mathbf{l}))^3 \right\rangle$ by

$$\Pi_K = -\frac{1}{6\pi} \int_0^\infty \mathrm{d}l \, \frac{\sin(Kl)}{l} \, (1 + l\partial_l) \, (3 + l\partial_l) \, (5 + l\partial_l) \, \frac{S_3(l)}{l}, \tag{1.48}$$

where $\partial_l \equiv \partial/\partial l$.

Homogeneous isotropic turbulence satisfies the following energy transfer relation:

$$\partial_t E(k) = T(k) + F(k) - 2\nu k^2 E(k), \tag{1.49}$$

where

$$\begin{aligned} T(k) &\equiv -\frac{\partial}{\partial_k} \Pi_k \\ &= \int_0^\infty \cos(kl)(1 + l\partial_l) \, (3 + l\partial_l) \, (5 + l\partial_l) \, \frac{S_3(l)}{6\pi l} \mathrm{d}l, \end{aligned} \tag{1.50}$$

and

$$E(k) = \frac{\partial}{\partial_k} \frac{1}{2} \left\langle |\mathbf{v}_k^<|^2 \right\rangle, \qquad F(k) = \frac{\partial}{\partial_k} \left\langle \mathbf{f}_k^< \cdot \mathbf{v}_k^< \right\rangle, \tag{1.51}$$

are the energy spectrum and the energy injection spectrum respectively [88].

1.3.3 From the Energy Flux Relation to the Four-Fifths Law

In our calculations so far, we have considered homogeneity and isotropy. Here, we introduce additional assumptions specific to fully developed turbulence.
(i) The driving force $\mathbf{f}(t, \mathbf{r})$ is acting only at large-scales. The force has no essential contributions coming from wave numbers $\gg K_c \sim l_0^{-1}$, where l_0 is the integral scale. In fact,

$$\mathbf{f}_K^<(t, \mathbf{r}) \simeq \mathbf{f}(t, \mathbf{r}), \qquad \text{for } K \gg K_c, \tag{1.52}$$

where $\mathbf{f}_K^<(t, \mathbf{r})$ is the low-pass filtered force defined in Appendix A.
(ii) For large times, the solution of the Navier-Stokes equations reaches a statistically stationary state with finite mean energy per unit mass.
(iii) In the infinite Reynolds number limit ($\nu \to 0$), the mean energy dissipation per unit mass $\epsilon(\nu)$ tends to a finite positive limit (hypothesis **H3** of section 1.3.1)

$$\lim_{\nu \to 0} \epsilon(\nu) = \epsilon > 0. \tag{1.53}$$

(iv) Scale-invariance (hypotheses **H1** and **H2**) is not assumed.
It is important to look at the consequences of these assumptions. Item (ii) results in the omission of the time-derivative terms in both the global energy budget equation

$$\partial_t \frac{1}{2} \left\langle \mathbf{v}^2 \right\rangle = \langle \mathbf{f}(\mathbf{r}) \cdot \mathbf{v}(\mathbf{r}) \rangle + \nu \left\langle \mathbf{v}(\mathbf{r}) \cdot \nabla^2 \mathbf{v}(\mathbf{r}) \right\rangle, \tag{1.54}$$

and in the scale-by-scale energy budget equation (1.46), which become respectively

$$\langle \mathbf{f} \cdot \mathbf{v} \rangle = -\nu \left\langle \mathbf{v} \cdot \nabla^2 \mathbf{v} \right\rangle = \epsilon(\nu), \tag{1.55}$$

and

$$\Pi_K = \mathcal{F}_K - 2\nu\Omega_K. \tag{1.56}$$

Consider the energy injection term $\mathcal{F}_K$ for $K \gg K_c$, using properties of (i) and (A.14), we have

$$\mathcal{F}_K = \left\langle \mathbf{f}_K^< \cdot \mathbf{v} \right\rangle \simeq \langle \mathbf{f} \cdot \mathbf{v} \rangle = \epsilon(\nu). \tag{1.57}$$

And, considering the energy dissipation term $2\nu\Omega_K$, for fixed K,

$$\lim_{\nu \to 0} 2\nu\Omega_K = 0, \tag{1.58}$$

and

$$\begin{aligned} 2\nu\Omega_K &= \nu \left\langle |\underline{\omega}_K^<|^2 \right\rangle \leq \nu K^2 \left\langle |\mathbf{v}_K^<|^2 \right\rangle \\ &\leq \nu K^2 \left\langle |\mathbf{v}|^2 \right\rangle = 2\nu K^2 E, \end{aligned} \tag{1.59}$$

where E is the mean energy assumed bounded by (ii). The first equality follows from the cumulative enstrophy (A.13) and the first inequality follows from the fact that the curl operator, acting on low-pass filtered vector fields with a cut-off at wave-number K, has a norm bounded by K.

In equation (1.56) if we take K to be $K \gg K_c$ and let $\nu \to 0$, using (1.53), (1.57), (1.58), we have

$$\lim_{\nu \to 0} \Pi_K = \epsilon, \qquad \forall K \gg K_c. \tag{1.60}$$

We can now conclude that in a statistically stationary state, the energy flux is independent of the scale under consideration and is equal to the energy input/dissipation, provided that there is no direct energy injection ($K \gg K_c$) and no direct dissipation ($\nu \to 0$). Combining (1.60) with the relation (1.48) for the energy flux and changing the integration variable from l to $x = Kl$, results in

$$\Pi_K = -\int_0^\infty \mathrm{d}x \, \frac{\sin x}{x} \, F(\frac{x}{K}) = \epsilon, \qquad \forall K \gg K_c, \tag{1.61}$$

where

$$F(l) \equiv (1 + l\partial_l)\,(3 + l\partial_l)\,(5 + l\partial_l)\,\frac{S_3(l)}{6\pi l}. \tag{1.62}$$

The large-K behaviour of the integral in (1.61) involves only the small-l behaviour of $F(l)$ and we have $\int_0^\infty \mathrm{d}x \, (\sin x/x) = \pi/2$. Therefore, for small l

$$F(l) \simeq -\frac{2}{\pi}\,\epsilon, \tag{1.63}$$

and after substituting (1.63) into (1.62), we have a linear third-order differential equation for $S_3(l)$. This equation can be solved using $\ln l$ as the independent variable and $S_3(l)/l$ as the dependent variable. The only solution which tends to zero as $l \to 0$ is

$$S_3(l) = -\frac{4}{5}\,\epsilon l, \tag{1.64}$$

and this completes the derivation of the four-fifths law [88].

1.3.4 Main Results of the Kolmogorov 1941 Theory

The four-fifths law can be rewritten as

$$\left\langle (\delta v_\parallel(l))^3 \right\rangle = -\frac{4}{5}\,\epsilon\, l, \tag{1.65}$$

where $\delta v_\parallel(l)$ is the longitudinal velocity increment and is defined as

$$\delta v_\parallel(\mathbf{r}, \mathbf{l}) \equiv [\mathbf{v}(\mathbf{r}+l) - \mathbf{v}(\mathbf{r})] \cdot \frac{\mathbf{l}}{l}, \tag{1.66}$$

with $l = |\mathbf{l}|$. With hypothesis **H2** from section (1.3.1), under rescaling of the increment l by a factor of λ, the left hand side of (1.65) changes by a factor λ^{3h}, while the right hand side changes by a factor λ. This implies that $h = 1/3$. Also from (1.47), which is valid irrespective of isotropy, and from the assumption of a scale invariant velocity with exponent h, it can be shown that $\Pi_k \propto K^{1-3h}$. This is independent of K only if $h = 1/3$. One must remember that it is not correct to infer $h = 1/3$ from the expression (A.15) for the energy flux. In fact this expression involves both $\mathbf{v}_K^< s$ and $\mathbf{v}_K^> s$. Using the hypothesis **H2** of section 1.3.1, it can also be shown that $\mathbf{v}_{K/\lambda}^> = \lambda^h \mathbf{v}_K^>$. Note that $\mathbf{v}_K^>$ involves only small-scales. Since there is no simple transformation property for $\mathbf{v}_K^<$, one cannot conclude the argument. This observation confirms how important it is to reexpress the energy flux solely in terms of velocity increments.

Now we examine the consequences for the moments of the longitudinal velocity increments at inertial-range separations, assuming homogeneity and isotropy. A further assumption that the moments of arbitrary positive order $p > 0$ are finite, is required. The longitudinal structure function of order p is then defined by

$$S_p(l) \equiv \left\langle (\delta v_\parallel(l))^p \right\rangle. \tag{1.67}$$

It is important to note that the argument of the structure functions is taken to be positive here, since l is the absolute value of the increment $\mathbf{l}$. One alternative definition, allowing for both positive and negative arguments x, is

$$S_p(x) \equiv \left\langle [(\mathbf{v}(\mathbf{r} + x\mathbf{l}^0) - \mathbf{v}(\mathbf{r})) \cdot \mathbf{l}^0]^p \right\rangle, \tag{1.68}$$

where $\mathbf{l}^0$ is an arbitrary unit vector. The above relation reduces to $S_p(l)$ for positive x.

From the hypothesis **H2** and $h = 1/3$, one can deduce that $S_p(l) \propto l^{p/3}$. Since $(\epsilon\, l)^{p/3}$ has exactly the same dimension as S_p, then

$$S_p(l) = C_p\, \epsilon^{p/3}\, l^{p/3}, \tag{1.69}$$

where C_ps are dimensionless. The C_ps are independent of the Reynolds number, since the limit of infinite Reynolds number is already taken. For $p = 3$ and from (1.64), it follows that $C_3 = -4/5$. This result is universal since it is independent of the particular flow under consideration. Observe that in the derivation shown here nothing requires the C_ps for $p \neq 3$ to be universal.

The important point here is that the expression (1.69) for the structure functions involves only the energy dissipation rate ϵ, the scale l and not the integral scale l_0. It therefore follows from the K41 that, if the limits $\nu \to 0$ and $l_0 \to \infty$ are taken, while holding $\epsilon > 0$ fixed, all the structure functions have finite limits. Also if the structure functions have finite non-vanishing limits when $\nu \to 0$ and $l_0 \to \infty$ while holding $\epsilon > 0$ fixed, then these limits display K41 scaling. In fact, for finite l_0, dimensional analysis suggests that the structure function of order p is given by the right hand side of (1.69) times a dimensionless function $\tilde{S}_p(l/l_0)$; this function has a finite non-vanishing limit as $l_0 \to \infty$, or, equivalently, as $l \to 0$, thereby ensuring K41 scaling. Therefore, deviations from K41 require that structure functions of order other than 3 have an explicit dependence on the integral scale at inertial-range separations.

Returning to the consequences of K41, the fact that the second-order structure function follows an $l^{2/3}$ law implies a $k^{-5/3}$ law for the energy spectrum. Considering (B.17), (B.18) and (1.69) results in

$$E(k) \sim \epsilon^{2/3} k^{-5/3}. \tag{1.70}$$

We will introduce the magnetic energy spectrum in section 3.2.2.

The experimental results support the K41 theory as far as the second-order structure function is concerned. However, the consistency between the K41 theory and experimental data on structure functions is questionable when $p > 3$ [88].

More remarks on Kolmogorov's four-fifths law are given in Appendix C.

Effect of a finite viscosity

When the viscosity ν is small, there is an 'inertial range' in which direct energy injection and energy dissipation are both negligible. This inertial range extends to scales comparable to the Taylor scale $\lambda = (5E/\Omega)^{1/2}$. Using the results of section 1.3.4, we can show that in the K41 framework, the inertial range extends down to the 'Kolmogorov dissipation scale'

$$\eta \equiv (\frac{\nu^3}{\epsilon})^{1/4}. \tag{1.71}$$

Consider the energy flux-relation (1.56), and assume that $K \gg K_c$ so that $\mathcal{F}_K \simeq \epsilon$. The dissipation term involves the cumulative enstrophy

$$\Omega_K = \frac{1}{2}\left\langle |\underline{\omega}_K^<|^2 \right\rangle = \int_0^K k^2 E(k) \mathrm{d}k, \tag{1.72}$$

and after substituting the inertial-range value (1.70) of the energy spectrum $E(k)$ into (1.72), we find the wave-number up to which the dissipation term $2\nu\Omega_K$ in (1.56) is negligible compared to the energy flux ϵ. This results in the following 'dissipation wave-number' (order unity constants have been omitted)

$$K_d = \left(\frac{\nu^3}{\epsilon}\right)^{-1/4}, \tag{1.73}$$

which is precisely the inverse of the 'Kolmogorov dissipation scale' η defined above. The range of scales comparable to or less than η is known as the 'dissipation range'. In this range the energy input from non-linear interactions and the energy drain from viscous dissipation are in exact balance.

Kolmogorov's first universality assumption

The first universality assumption states that at very high, but not infinite Reynolds numbers, all the small-scale statistical properties are uniquely and universally determined by the scale l, the mean energy dissipation rate ϵ and the viscosity ν (or, equivalently, by l, ϵ and η).

'Small-scale' is considered to be scales small compared to the integral scale, i.e. inertial range and dissipation-range scales. The first universality assumption results in the following universal form for the energy spectrum at large wave-numbers

$$E(k) = \epsilon^{2/3} k^{-5/3} F(\eta k), \tag{1.74}$$

where $F(\cdot)$ is a universal dimensionless function of a dimensionless argument. By the second universality assumption of Kolmogorov (section 1.3.1), $F(\cdot)$ tends to a finite positive limit (Kolmogorov constant) for vanishing argument. The universality of the function $F(\cdot)$ has been questioned by Frisch and Morf [89].

There have been several attempts to determine the functional form of $F(\cdot)$ at high wave-numbers. The most interesting result is by von Neumann [161]. He observed that an analytic function has a Fourier transform which decays exponentially at high wave-numbers. The logarithmic decrement is equal to the modulus δ of the imaginary part of the position of the singularity in complex space nearest to the real domain. Hence, in von Neumann's view, exponential decay at high k is more likely than the rapid algebraic decay proposed by Heisenberg [104]. For a random homogeneous function, the situation is a bit more complicated: since there is a probability distribution $P(\delta)$ and therefore the form of the energy spectrum at high k is the Laplace transform of $P(\delta)$ near its minimum value δ_* [89]. An exponential decay is obtained only if $\delta_* > 0$, i.e. if there is a tubular region around the real domain in which almost all realizations are analytic. This is known as uniform analyticity. The experimental results suggest that this condition may be satisfied [90].

1.4 Magnetohydrodynamics (MHD)

1.4.1 Introduction

Magnetohydrodynamics (MHD) studies the dynamics of electrically conducting fluids. Examples of such fluids are plasmas and liquid metals. Here, we present the equations used to describe MHD model. In this section we allow compressibility (div $\mathbf{v} \neq 0$) [22]. The ideal MHD equations are

$$\rho \frac{\mathrm{d}\,\mathbf{v}}{\mathrm{d}t} = -\nabla p + \mathbf{J} \times \mathbf{B}, \tag{1.75}$$

$$\mathbf{J} = \frac{1}{\mu} \nabla \times \mathbf{B}, \tag{1.76}$$

$$\frac{\partial}{\partial t}\,\mathbf{B} = -\nabla \times \mathbf{E}, \tag{1.77}$$

$$\mathbf{E} = -\mathbf{v} \times \mathbf{B}, \tag{1.78}$$

$$-\frac{\partial}{\partial t}\,p = -\mathbf{v} \cdot \nabla p - \Gamma p \nabla \cdot \mathbf{v}, \tag{1.79}$$

$$\frac{\partial}{\partial t}\,\rho = -\mathbf{v} \cdot \nabla \rho - \rho \nabla \cdot \mathbf{v}, \tag{1.80}$$

where (1.80) is derived from the following relation

$$\frac{\partial \rho}{\partial t} + \nabla \cdot \rho \mathbf{v} = 0. \tag{1.81}$$

The state of the system at any point in space and time is given by the variables $\mathbf{v}$, $\mathbf{B}$, p and ρ, where $\mathbf{v}$ is the macroscopic fluid velocity, $\mathbf{B}$ is the magnetic field, p is the thermal pressure and ρ is the mass density. The MHD equations represent how this state advances in time. The electric field $\mathbf{E}$ and the current density $\mathbf{J}$ are treated as auxiliary quantities, where $\mathbf{E}$ is measured in the laboratory frame of reference. The first MHD equation (1.75) describes the acceleration of the fluid in response to local forces. The convective derivative

$$\frac{\mathrm{d}}{\mathrm{d}t} = \frac{\partial}{\partial t} + \mathbf{v} \cdot \nabla, \tag{1.82}$$

appearing on the left in (1.75), represents the time rate of change at a point that follows the flow of fluid. The pressure gradient on the right in (1.75) is the force resulting from a difference in thermal pressure on opposite sides of an infinitesimal element of fluid. The $\mathbf{J} \times \mathbf{B}$ force is the sum of Lorentz magnetic forces $Z_i e \mathbf{v}_i \times \mathbf{B}$ on the individual charged particles that make up the plasma ($Z_i e$ is the charge and $\mathbf{v}_i$ is the velocity of each particle).

Equation (1.76) is Ampere's law with displacement current $\epsilon \partial \mathbf{E}/\partial t$ ignored. This magnetostatic approximation is valid when the Alfvén velocity $v_A \equiv B/\sqrt{\mu\rho}$ is much smaller than the speed of light. It is important to note that all electrical currents are assumed to be explicit, i.e. we are not in a magnetized medium, therefore μ stands for magnetic permeability in a vacuum

$$\mu \equiv \mu_0 = 4\pi \times 10^{-7} \,\text{Henrys/meter}. \tag{1.83}$$

Equation (1.77) is Faraday's law for the evolution of the magnetic field. A magnetic field must be divergence free

$$\nabla \cdot \mathbf{B} = 0. \tag{1.84}$$

If $\nabla \cdot \mathbf{B} = 0$ is used as an initial condition, Faraday's law guarantees that $\nabla . \mathbf{B}$ will be zero for all time. The electric field appearing in Faraday's law is the electric field in the laboratory frame of reference. In order to change to a frame of reference moving with the fluid, the electric field must be transformed by the addition of a $\mathbf{v} \times \mathbf{B}$ term. This transformation can be derived by assuming the Galilean invariance of Faraday's law as an approximation to its relativistic invariance. In fact (1.78) follows from this transformation by taking the electric field to be zero in the frame of reference moving with the perfectly conducting fluid. Therefore, (1.78) is a special

form of Ohm's law. The motion of the plasma changes the magnetic field through Faraday's law (1.77) and Ohm's law (1.78), while the magnetic field acts on the motion of the plasma through the equation of motion (1.75).

The mass density and pressure are altered by the plasma motion through the thermodynamic equations (1.79) and (1.80). The $\mathbf{v}\,.\,\nabla p$ and $\mathbf{v}.\,\nabla\rho$ terms on the right side of these equations represent the effect of convection and the effect of compression and expansion is described by $\Gamma\, p\,\nabla.\,\mathbf{v}$ and $\rho\,\nabla.\,\mathbf{v}$. As a result of these terms, the pressure and density change as the fluid elements change size in response to changes in pressure. The constant $\Gamma = 5/3$ represents the ratio of specific heat for an ideal gas with three degrees of freedom.

In next section, we are concerned with the consequences of Faraday's law (1.77) in a perfectly conducting fluid.

1.4.2 Magnetic Flux

The magnetic field has the form of any three-dimensional vector field that is divergence free ($\nabla.\,\mathbf{B} = 0$). The divergence free property is the indicator of the fact that there are no sources or sinks of magnetic field and it does not imply that all magnetic field lines close upon themselves. A magnetic field line is everywhere tangent to the magnetic field.

Magnetic flux is the amount of magnetic field passing through any given surface

$$\psi \equiv \int \mathrm{d}\mathbf{S}\,\cdot\,\mathbf{B}. \tag{1.85}$$

The divergence-free property of magnetic fields results in each of the following statements:
1. The amount of flux leaving a volume is the same as the amount entering it.
2. The flux through any surface spanning a given closed curve is the same.
The above statements are proved using Gauss's theorem

$$\oint \mathrm{d}\mathbf{S}\,\cdot\,\mathbf{B} = \int \mathrm{d}^3x\,\nabla\,\cdot\,\mathbf{B} = 0. \tag{1.86}$$

Note that the equation $\nabla\,\cdot\,\mathbf{B} = 0$ is in fact the differential form of conservation of magnetic flux. This can be shown by writing the expression $(\nabla\,\cdot\,\mathbf{B})\,\mathrm{d}x\;\mathrm{d}y\;\mathrm{d}z$ in finite difference form within an arbitrary small rectangular box with surface areas $\mathrm{d}x\,\mathrm{d}y$, $\mathrm{d}y\,\mathrm{d}z$, and $\mathrm{d}z\,\mathrm{d}x$. To prove the second statement, consider that there is a volume enclosed between any two surfaces spanning the same closed curve and apply Gauss's theorem.

Faraday's law (1.77) is the result of the following experimental observation: As the flux through any closed loop of wire is changed, the electric field observed around the wire is given by

$$\oint \mathrm{d}\mathbf{I} \cdot \mathbf{E} = -\frac{\mathrm{d}}{\mathrm{d}t}\,\psi. \tag{1.87}$$

It does not matter if the flux is changing because the field is changing or the wire is moving. The wire may be replaced by any closed contour in space.

Now consider the case where the field is changing and the contour is moving or deforming. In a differential interval of time, each element of the contour moves a distance $\mathbf{v} \cdot \mathrm{d}t$, and each differential length of the contour sweeps out an area $\mathrm{d}\mathbf{I} \times \mathbf{v} \cdot \mathrm{d}t$. The flux through the new contour is equal to the flux through the old contour minus the flux leaving the differential area swept out by the motion of the contour. The total rate of change of flux is given by

$$\frac{\mathrm{d}}{\mathrm{d}t}\,\psi = \int \mathrm{d}\mathbf{S} \cdot \frac{\partial \mathbf{B}}{\partial t} - \oint \mathrm{d}\mathbf{I} \times \mathbf{v} \cdot \mathbf{B}, \tag{1.88}$$

and this with (1.87) leads to

$$\oint \mathrm{d}\mathbf{I} \cdot [\mathbf{E} - \mathbf{v} \times \mathbf{B}] = -\int \mathrm{d}\mathbf{S} \cdot \frac{\partial \mathbf{B}}{\partial t}, \tag{1.89}$$

where the electric field in (1.89) is the electric field moving with the contour.

The electric field around the fixed contour, which is coincident with any instantaneous position of the moving contour, is

$$\oint \mathrm{d}\mathbf{I} \cdot \mathbf{E}_{\text{fixed}} = -\int \mathrm{d}\mathbf{S} \cdot \frac{\partial \mathbf{B}}{\partial t}. \tag{1.90}$$

Here, the Galilean invariance of Faraday's law is an approximation to its relativistic invariance. That is, the magnetic field at any point in space and time is independent of the observer's frame of reference. However the electric field is a function of velocity at which the observer is moving. The difference between fixed and the moving electric field is obtained by comparing (1.89) and (1.90) for arbitrarily chosen contours so that

$$\mathbf{E}_{\text{fixed}} = \mathbf{E}_{\text{moving}} - \mathbf{v} \times \mathbf{B}. \tag{1.91}$$

For a perfectly conducting plasma, the electric field is zero in the frame of reference moving with each fluid element. From (1.91) the electric field observed in the laboratory frame of reference must be

$$\mathbf{E}_{\text{fixed}} = -\mathbf{v} \times \mathbf{B}, \tag{1.92}$$

where $\mathbf{v}$ is the velocity of the fluid. Therefore, the ideal MHD Ohm's law (1.78) is the result of the Galilean invariance of Faraday's law and the assumption that the electric field moving with the plasma is zero.

It is important to note that the force acting on any moving charged particle is $Z_i e\mathbf{E}$. Considering the fixed frame of reference, the force is $Z_i e\mathbf{E}_{\text{fixed}} + Z_i e\mathbf{v} \times \mathbf{B}$, where the second term is the Lorentz force acting on a moving particle in a magnetic field. Summing over all the charged particles that make up the plasma, the $\mathbf{v} \times \mathbf{B}$ term leads to the $\mathbf{J} \times \mathbf{B}$ force in the MHD equation of motion (1.75).

1.4.3 Motion of Magnetic Field Lines

The motion of magnetic field lines within a perfectly conducting fluid is consistent with Faraday's law. The position of field lines at any instant in time is unique, but the motion of field lines from one instant to the next is a matter of interpretation. Consider a representation of the magnetic field in the form of

$$\mathbf{B} = \nabla\alpha \times \nabla\beta, \tag{1.93}$$

where α and β are Euler potentials. One can prove that (1.93) results in $\nabla.\,\mathbf{B} = 0$, by rearranging (1.93) to form $\mathbf{B} = \nabla \times (\alpha\nabla\beta)$ or $\mathbf{B} = -\nabla \times (\beta\,\nabla\alpha)$, and note that $\nabla.\nabla \times \ldots = 0$. To prove that a divergence-free vector field can be represented by (1.93), consider a pair of functions α', β' that are constant along each magnetic field line. That is, the magnetic field is everywhere tangent to the surfaces of constant α' and constant β', and these surfaces never coincide. It follows that $\nabla\alpha' \times \nabla\beta'$ is in the direction of the magnetic field at every point and it can be multiplied by an appropriate function of space and time $f(\mathbf{x}, t)$ to make the magnitudes agree,

$$\mathbf{B} = f(\mathbf{x}, t)\ \cdot \nabla\alpha'(\mathbf{x}, t) \times \nabla\beta'(\mathbf{x}, t). \tag{1.94}$$

Also, since the magnetic field must be divergence-free,

$$\nabla.\,\mathbf{B} = \nabla f\ \cdot \nabla\alpha' \times \nabla\beta' = 0, \tag{1.95}$$

then $f(\mathbf{x}, t)$ must be a function of α' and β' alone, $f = f(\alpha', \beta', t)$. And f can be absorbed into the cross product $\nabla\alpha' \times \nabla\beta'$ by defining,

$$\alpha = \int_0^{\alpha} d\alpha' f(\alpha', \beta') \qquad \beta = \beta', \tag{1.96}$$

in order to obtain (1.93).

Note that α and β are not unique for any given magnetic field. For instance, any function of β can be added to α, or any function of α can be added to β, without changing $\nabla\alpha \times \nabla\beta$, thus

$$\mathbf{B} = \nabla\alpha \times \nabla\beta = \nabla[\alpha + f(\beta)] \times \nabla\beta = \nabla\alpha \times \nabla[\,\beta + f(\alpha)]. \tag{1.97}$$

An equation for the time evolution of α and β can be derived by substituting $\mathbf{B} = \nabla\alpha \times \nabla\beta$ into Faraday's law for a perfectly conducting fluid

$$\frac{\partial \mathbf{B}}{\partial t} = \nabla \times (\mathbf{v} \times \mathbf{B}), \tag{1.98}$$

$$\nabla\frac{\partial\alpha}{\partial t} \times \nabla\beta + \nabla\alpha \times \nabla\frac{\partial\beta}{\partial t} = \nabla \times [\,\mathbf{v} \times (\nabla\alpha \times \nabla\beta)], \tag{1.99}$$

$$\nabla \times [\frac{\partial\alpha}{\partial t}\nabla\beta - \frac{\partial\beta}{\partial t}\nabla\alpha - \mathbf{v} \cdot \nabla\beta\nabla\alpha + \mathbf{v} \cdot \nabla\alpha\nabla\beta] = 0, \tag{1.100}$$

$$\nabla \times [\,\frac{\mathrm{d}\alpha}{\mathrm{d}\beta}\nabla\beta - \frac{\mathrm{d}\beta}{\mathrm{d}t}\nabla\alpha\,] = 0, \tag{1.101}$$

where $\mathrm{d}/\mathrm{d}\,t$ is the convective derivative defined for any velocity field $\mathbf{v}(x,t)$. Then we must have

$$\frac{\mathrm{d}\alpha}{\mathrm{d}t}\nabla\beta - \frac{\mathrm{d}\beta}{\mathrm{d}t}\nabla\alpha = \nabla\vartheta, \tag{1.102}$$

where ϑ is an arbitrary function of space and time. A perfectly valid choice for ϑ is when $\vartheta = 0$ and this leads to

$$\frac{\mathrm{d}}{\mathrm{d}t}\,\alpha = 0, \quad \frac{\mathrm{d}}{\mathrm{d}t}\,\beta = 0. \tag{1.103}$$

For this particular choice of ϑ, the scalar fields $\alpha(x,t)$ and $\beta(x,t)$ move with the fluid. Also, the lines of constant α and β, and therefore the magnetic field lines, must move with the fluid. Hence field lines cannot break or change topology as long as the fluid motion is continuous, in the sense that adjacent elements of fluid always remain adjacent. Since this topological invariance is a conclusion about field lines, which are unique regardless of the α, β representation, this conclusion must be true for any choice of ϑ [22].

The physical interpretation of the arbitrariness of the motion of field lines is subtle. When there is finite resistivity: at limit zero magnetic diffusivity, i.e. $\eta = 0$, field lines can move uniquely.

1.4.4 The Magnetic Force

The motion of a perfectly conducting fluid acts on a magnetic field through Faraday's law and the magnetic field, in turn, acts on the fluid through the $\mathbf{J} \times \mathbf{B}$ force in the equation of motion (1.75). The $\mathbf{J} \times \mathbf{B}$ force can be written in terms of the curvature of the magnetic field lines and the gradient of the magnetic field strength by writing

$$\mu \, \mathbf{J} \times \mathbf{B} = (\nabla \times \mathbf{B}) \times \mathbf{B} = \mathbf{B} \cdot \nabla \mathbf{B} - \frac{1}{2} \nabla B^2. \tag{1.104}$$

The unit vector along the magnetic field line is $\hat{\mathbf{B}} = \mathbf{B} / |\mathbf{B}|$ and thus

$$\mu \, \mathbf{J} \times \mathbf{B} = B^2 \, \hat{\mathbf{B}} \cdot \nabla \hat{\mathbf{B}} + \frac{1}{2} (\hat{\mathbf{B}} \hat{\mathbf{B}} \cdot \nabla B^2 - \nabla B^2). \tag{1.105}$$

The gradient of $\hat{\mathbf{B}}$ along the field line is just the curvature κ of the field line

$$\kappa = \hat{\mathbf{B}} \cdot \nabla \hat{\mathbf{B}}, \tag{1.106}$$

whose magnitude is equal to the reciprocal of the radius of curvature. One can write the other two terms in (1.105) as the perpendicular gradient

$$\nabla_\perp \equiv \nabla - \hat{\mathbf{B}} \hat{\mathbf{B}} \cdot \nabla, \tag{1.107}$$

of B^2 and therefore

$$\mathbf{J} \times \mathbf{B} = \frac{1}{\mu} [B^2 \kappa - \frac{1}{2} \nabla_\perp B^2]. \tag{1.108}$$

The tension of the magnetic field lines produces a force $(1/\mu) B^2 \kappa$ that is directed toward the centre of curvature, in the same way as tension acts on a string. Then the pressure of the magnetic field produces a force $(1/2\mu) \nabla_\perp B^2$ directed away from the region of high field strength. Bending the magnetic field produces tension and compressing it produces a restoring pressure.

1.4.5 Conservative Forms of the MHD Equation

The conservative form of an equation is when the temporal rate of change of a quantity is set equal to the divergence of its flux. The conservative form of the ideal MHD equations in a fixed coordinate system can be written as,

$$\frac{\partial}{\partial t} (\rho \, \mathbf{v}) = \nabla \cdot \left[-\rho \, \mathbf{v}\mathbf{v} + \frac{1}{\mu} \mathbf{B}\mathbf{B} - (p + B^2/2\mu) \right], \tag{1.109}$$

$$\frac{\partial}{\partial t} \mathbf{B} = \nabla \times (\mathbf{v} \times \mathbf{B}) = \nabla \cdot (\mathbf{v}\mathbf{B} - \mathbf{B}\mathbf{v}), \tag{1.110}$$

$$\frac{\partial}{\partial t} \rho = -\nabla \cdot (\rho \, \mathbf{v}), \tag{1.111}$$

$$\begin{aligned}
\frac{\partial}{\partial t}\left(\rho\mathbf{v}^2 + \frac{p}{\Gamma-1} + \frac{1}{2\mu}B^2\right) &= \text{kinetic + potential energy} \\
&= -\nabla\cdot\left[\left(\frac{1}{2}\rho\mathbf{v}^2 + \frac{p}{\Gamma-1} + p\right)\mathbf{v} + \frac{1}{\mu}\,\mathbf{E}\times\mathbf{B}\right] \\
&= \text{(convection of kinetic + thermodynamic energy + pressure)} \\
&+ \text{Poynting flux.} \qquad (1.112)
\end{aligned}$$

The above equations represent the time evolution of momentum, magnetic flux, mass density, and total energy at any point in space. Integrating each equation over any fixed volume and using Gauss's theorem will result in the right hand side of each equation representing a flux through the boundaries of the closed volume.

Conservative forms of equations like these are specially useful in computational work. They can also be useful for determining the natural boundary conditions which isolate the system under study from the outside world. Although the system is isolated if the net fluxes through all the boundaries are zero, it is customary to require that all the fluxes are zero through each differential element of the boundary.

For example, to conserve total mass, there must be no convection across the boundary $\mathbf{v}_\perp = 0$. To conserve energy, the Poynting flux must also be zero

$$(\mathbf{E}\times\mathbf{B})_\perp = 0. \qquad (1.113)$$

To conserve magnetic flux, there must be no electric field parallel to the boundary $\mathbf{E}_\parallel = 0$. To prove this final boundary condition, one can integrate Faraday's law (1.77) over any fixed differential area of the boundary

$$\frac{\partial}{\partial t}\int \mathrm{d}\mathbf{S}\cdot\mathbf{B} = -\int \mathrm{d}\mathbf{S}\cdot\nabla\times\mathbf{E} = -\oint \mathrm{d}\mathbf{I}\cdot\mathbf{E}. \qquad (1.114)$$

To determine the boundary conditions, the momentum equation is not generally used, since the force that may have to be exerted by the wall on the plasma in order to hold $\mathbf{v}_\perp = 0$ as the system evolves, is not explicitly written into momentum equation (1.109).

It is important to note that the boundary condition $\mathbf{E}_\parallel = 0$ implies $(\mathbf{E}\times\mathbf{B})_\perp = 0$. Also, if the boundary is initially a flux surface, $\mathbf{B}_\perp = 0$, and if the adjacent fluid is perfectly conducting, then $\mathbf{E} = -\mathbf{v}\times\mathbf{B}$, and the boundary condition $\mathbf{v}_\perp = 0$ implies $\mathbf{E}_\parallel = 0$, and the boundary always remains a flux surface. Under these conditions a rigid wall $\mathbf{v}_\perp = 0$ is the only boundary condition needed. Alternatively, if the boundary is separated from the plasma by a vacuum region, or if the plasma

adjacent to the boundary has zero pressure and density, then the condition $\mathbf{v}_\perp = 0$ can be dropped and a perfectly conducting wall $\mathbf{E}_\parallel = 0$ is all that is required. Under all these conditions a rigid, perfectly conducting wall will completely isolate the plasma in the MHD model.

Also, one can write the conservative forms of the MHD equations in a Lagrangian coordinate system moving with the fluid. We have already shown that the elements of magnetic flux, α and β, can be considered fixed in each perfectly conducting fluid element (1.103). Also one can combine the equations for pressure (1.79) and mass density (1.80) in order to show that the entropy, defined by $e(\mathbf{x}, t) \equiv p/\rho^\Gamma$, is conserved in each fluid element so that $\mathrm{d}/\mathrm{d}t\,(p/\rho^\Gamma) = 0$. However, this equation does not mean that the entropy is uniform over the plasma volume.

1.4.6 MHD Equilibrium

In the MHD theory of magnetically confined plasmas, equilibrium means the complete balance of forces. The standard MHD equilibrium equations are

$$\nabla p = \mathbf{J} \times \mathbf{B}, \tag{1.115}$$

$$\mathbf{J} = \frac{1}{\mu} \nabla \times \mathbf{B}, \tag{1.116}$$

$$\nabla \cdot \mathbf{B} = 0. \tag{1.117}$$

These equations apply to plasmas with scalar pressure in a steady state $(\partial/\partial t) = 0$, with no flow $(\mathbf{v} = 0)$, and no body forces such as gravity or neutral gas pressure. These are the most commonly used assumptions for tokamaks and pinches.

These equilibrium equations can be written differently. For instance, when the $\mathbf{J} \times \mathbf{B}$ force is written as the sum of magnetic pressure and magnetic tension , as in (1.108), the equations become

$$\nabla_\perp (p + B^2/2\mu) = \frac{1}{\mu} B^2 \kappa, \tag{1.118}$$

where as stated before $\kappa = \hat{\mathbf{B}}.\nabla\hat{\mathbf{B}}$ is the curvature of the field lines. Alternatively, using (1.104) it can be written

$$\nabla (p + B^2/2\mu) = \frac{1}{\mu} \mathbf{B} \cdot \nabla \mathbf{B}. \tag{1.119}$$

The stress tensor form of $\mathbf{J} \times \mathbf{B}$ results in

$$\nabla \cdot [\frac{1}{\mu}\mathbf{BB} - (p + B^2/2\mu)] = 0, \tag{1.120}$$

and integrating this divergence of the stress tensor over an arbitrary volume and using Gauss's theorem provides an integral form of the equilibrium equations

$$\oint \mathrm{d}\mathbf{S} \cdot [(p + B^2/2\mu)\hat{\mathbf{n}} - \hat{\mathbf{n}} \cdot \mathbf{BB}] = 0, \tag{1.121}$$

where S is any closed surface with normal $\hat{\mathbf{n}}$.

1.4.7 Magnetic Surface

If a magnetic field line is followed long enough, it will either close upon itself or continue indefinitely to cover a surface, or fill a volume, or leave the bounded domain. Here, the magnetically confined plasmas of concern are those in which most of the field lines continue indefinitely, ergodically covering a set of simply nested toroidal surfaces. Any surface that is covered by a magnetic field line is considered to be a magnetic surface. A field line covers a magnetic surface ergodically if it passes arbitrarily close to any point on the surface. Magnetic surfaces covered ergodically are topologically equivalent to a torus.

For some tori, the magnetic field lines close upon themselves after a finite number of transits the long way around the torus. These closed field lines lie on toroidal magnetic surfaces, called rational surfaces, in between the ergodically covered toroidal magnetic surfaces in much the same way as rational numbers are interspersed between irrational numbers. When the field lines on a particular rational surface have the same topology as that of an instability being considered, the surface is called a mode-rational surface. These surfaces play an important role in the theory of instabilities.

There are many possibilities for magnetic fields besides the simply nested toroidal configuration. Magnetic surfaces can break up into thin filaments called magnetic islands that twist through the plasma. The islands themselves can carry smaller islands within them and these smaller islands can, in turn, carry successively finer and finer island structures. Alternatively, a magnetic field line can fill a volume quasi-ergodically-randomly wandering around so that it comes arbitrarily close to any point in the volume. At the other extreme, it is possible for all the field lines to be closed, leaving no well-defined flux surfaces.

Consider a given toroidal magnetic surface and consider the cut surfaces which span across the hole in the toroid, S_{pol}, and across a cross section of the toroid, S_{tor}, as shown in figure 1.5. The toroidal flux ψ_{tor}, through any cross section of the toroid S_{tor}, is

$$\psi_{tor} \equiv \int_{S_{tor}} \mathrm{d}\mathbf{S} \cdot \mathbf{B} = \text{flux the long way around}, \tag{1.122}$$

and through any cut surface spanning the centre of the toroid, S_{pol}, the poloidal flux is

$$\psi_{pol} \equiv \int_{S_{pol}} \mathrm{d}\mathbf{S} \cdot \mathbf{B} = \text{flux the short way around}. \tag{1.123}$$

The flux is the same for all surfaces spanning the same contour, and there is no flux through the toroidal magnetic surface since the magnetic field is everywhere tangent to it. Hence, the flux is the same through any topologically equivalent contour (C_{tor} or C_{pol}) on the flux surface. It follows that both ψ_{tor} and ψ_{pol} are surface quantities, where a surface quantity is any variable that is uniform over a magnetic surface. Conversely, it can be shown that all flux surfaces (surfaces of constant ψ_{tor} and ψ_{pol}) are magnetic surfaces.

There are many other surface quantities used in the theory of MHD equilibria. For instance, the fact that pressure is a surface quantity follows from $\mathbf{B}.\nabla p = 0$, which is a direct consequence of $\nabla p = \mathbf{J} \times \mathbf{B}$. If the pressure changes from surface to surface, so that $|\nabla p| \neq 0$ except at isolated magnetic surfaces, then the toroidal and poloidal currents are also surface quantities

$$I_{tor} \equiv \int_{S_{tor}} \mathrm{d}\mathbf{S} \cdot \mathbf{J} = \frac{1}{\mu} \oint_{C_{pol}} \mathrm{d}\mathbf{I} \cdot \mathbf{B}, \tag{1.124}$$

which equals total current the long way around within a magnetic surface, and

$$I_{pol} \equiv \int_{S_{tor}} \mathrm{d}\mathbf{S} \cdot \mathbf{J} = \frac{1}{\mu} \oint_{C_{pol}} \mathrm{d}\mathbf{I} \cdot \mathbf{B}, \tag{1.125}$$

which equals total current through the hole in a toroidal magnetic surface.

These follow from the fact that $\mathbf{J}.\nabla p = \mathbf{J} \cdot \mathbf{J} \times \mathbf{B} = 0$ implies that no current passes through the magnetic surfaces [22].

1.5 MHD Turbulence

Most astrophysical flows such as solar winds are often in a turbulent state and are coupled to magnetic fields. The ubiquity of turbulence in the universe is the direct

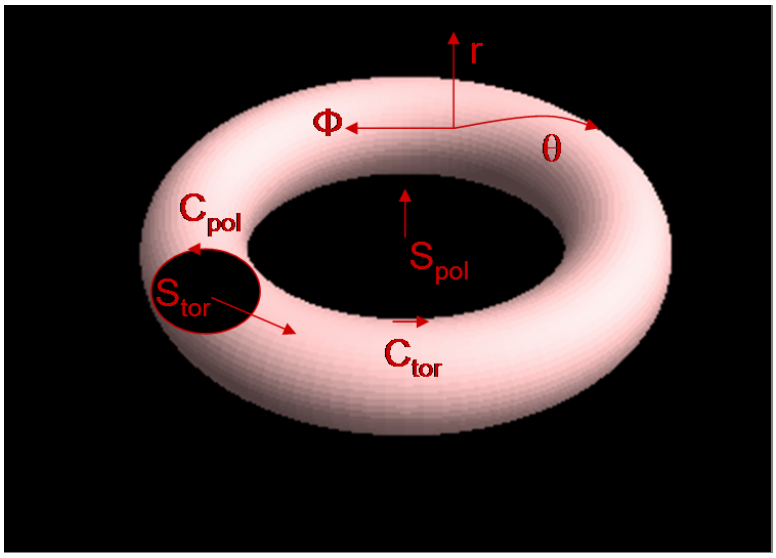

Figure 1.5: Toroidal flux surface showing cut surfaces and contours.

result of the fact that the dynamics of most non-stationary astrophysical plasma flows are characterized by a wide range of length scales and velocities [81]. Therefore understanding and quantifying the properties of MHD turbulence is crucial to explain these physical processes in the Cosmos and in industrial flows [1, 63]. The theoretical description of these flows is one of the major keys for a better understanding of many diverse phenomena such as the generation of large-scale magnetic fields accompanying many celestial objects by the turbulent dynamo effect [38, 255]. A few specific examples are: the dynamics of stellar winds and their action with planetary magnetospheres [97]; the discrepancy between observed and predicted life-times of star-forming molecular clouds in the interstellar medium [258]; and the angular transport within accretion disks prone to magnetorotational instability [103].

It has been a major challenge to characterize the complexity associated with turbulence from first principles based on theoretical treatment [81]. The development of a rigorous statistical formalism for hydrodynamic turbulence was first initiated in the 1930s by Taylor et al. [21], and it culminated during the 1970s in a variety of stochastic models and statistical approximations [81]. For instance, Kraichnan's direct interaction approximation (DIA) [121] represents a self-consistent expansion of the Navier-Stokes and MHD equations discussed in the previous sections. However, the problem with the DIA formalism is that it is not invariant under random Galilean transformations and this results in an incorrect energy scaling spectrum in the hydrodynamic (HD) case [81]. There are two assumptions used in the HD case that are not necessarily true for the MHD case. In the MHD case, the assumption of

isotropy used in the HD case breaks down because of the imposed uniform magnetic field. Also, in the HD case, there is a local interaction between different scales, and the effect of large eddies on smaller eddies is the advection of the smaller eddies (this effect is taken away by Galilean Transformation). However, in MHD the effects of large-scale fluctuations of the magnetic field cannot be eliminated. Therefore, in MHD, smaller scales also interact and affect the larger scales [1].

The only statistical approximation that is being applied fruitfully to MHD turbulence is the eddy-damped quasi-normal Markovian approximation (EDQNM) in the field of dynamo theory [181]. The EDQNM approach results in evolution equations for the second-order statistical moments of the turbulent fields by modelling the fourth order cumulants as linear damping terms where the associated eddy damping rate acts as a free parameter [81].

For the remainder of this section, we outline the current state of MHD turbulence and review some of the recent theoretical developments.

1.5.1 Properties of MHD Turbulence

MHD flows have two fields, the velocity and magnetic fields, and there are two energies associated with these fields. The two associated energies allow many possibilities of energy transfer between smaller or larger scales. This makes the dynamics more complex to address in theory and in modelling [1].

In MHD, the effects of large-scale fluctuations of the magnetic field cannot be eliminated. Hence, this makes it possible for smaller scales to interact with larger scales. If this is the case, one can not consider a "contiguous" transfer of energy in wave-number space and cannot *a priori* follow the same arguments Kolmogorov used for HD turbulence [1]. Therefore, it is important to have the knowledge of energy transfer among different scales in order to construct MHD turbulence. The energy transfer and locality of the interactions in MHD turbulence have been investigated through various models. Present models consider Kolmogorov-like arguments and take into account the effect of the magnetic field. The energy transfer has been studied by Pouquet, Frisch and Léorat [181] within the EDQNDM and more recently by Schilling and Zhou [204] where non-local interactions have been realized. The transfer of energy in MHD turbulence has also been estimated by field-theoretical calculation methods [243, 244].

The locality of the energy transfer in MHD has been investigated through three-dimensional direct numerical simulation (DNS) recently [64]. Debliquy, Verma and Carati [64] measured the transfer of energy between different scales and fields using free decaying MHD turbulence simulations with 512^3 grid points. Their results indicate that there is a local transfer of energy between the same fields, while the transfer between different fields shows a less localised behaviour, in the sense that a wider range of scales are involved in the interactions.

Mechanically forced MHD turbulence has been investigated by Alexakis, Mininni and Pouquet [1], where they consider a mechanical external forcing that generates a well-defined large-scale flow and small-scale turbulent fluctuations. This leads to an interesting result for some astrophysical and geophysical flows where magnetic fields are believed to remain unchanged against ohmic dissipation by a dynamo process [154] and the only external source of energy driving the system is mechanical. In this case, the energy is forced through the velocity field and the system reaches a steady state with equipartition between the two fields. For this to happen there must be a nonzero flux for all times from the velocity field to the magnetic field. The result of their calculations show that the transfer of magnetic and velocity energy from large-scales to small-scales is local. This is also the case for neutral fluids and is compatible with the Kolmogorov theory of turbulence. However, the transfer of energy from kinetic (velocity field) to magnetic remains a highly non-local process in Fourier space [1].

1.5.2 Theory and Definitions

The equations describing the dynamics of an incompressible conducting fluid coupled to a magnetic field in MHD turbulence are given by

$$\partial_t \mathbf{v} + \mathbf{v} \cdot \nabla \mathbf{v} = -\nabla p + \mathbf{B} \cdot \nabla \mathbf{B} + \nu \nabla \mathbf{v} + \mathbf{f}, \tag{1.126}$$

$$\partial_t \mathbf{B} + \mathbf{v} \cdot \nabla \mathbf{B} = \mathbf{B} \cdot \nabla \mathbf{v} + \eta \nabla^2 \mathbf{B}, \tag{1.127}$$

with $\nabla \cdot \mathbf{v} = \nabla \cdot \mathbf{B} = 0$ where $\mathbf{v}$ is the velocity field, $\mathbf{B}$ is the magnetic field, p is the total pressure, ν and η are the viscosity and magnetic diffusivity, respectively and $\mathbf{f}$ is the external force that drives the MHD turbulence [1].

The dynamic state of MHD flow is characterized by the non-dimensional parameters

$$\nu = Re^{-1} = \frac{\nu_*}{Lv}, \qquad \text{and} \qquad \eta = {R_m}^{-1} = \frac{\eta_*}{Lv}, \tag{1.128}$$

where Re is the kinetic Reynolds number defined with the kinematic viscosity ν_* and R_m the magnetic Reynolds number involving the magnetic diffusivity η_* of the MHD fluid. The MHD flow undergoes a transition from a laminar state to a turbulent state if both Re and R_m become sufficiently larger than unity. This state is characterized by erratic and unpredictable fluid motions [81].

MHD turbulence is classified by the kinetic energy of the flow field

$$E^K = \frac{1}{2}\int_V \mathrm{d}V v^2, \tag{1.129}$$

and the magnetic energy

$$E^M = \frac{1}{2}\int_V \mathrm{d}V B^2, \tag{1.130}$$

where V is the spatial volume of the system. There are two extreme cases associated with these two energies. One is characterized by $E^K \gg E^M$, where the magnetic field is passively advected by the fluid, and the other is $E^K \ll E^M$, with a strong magnetic field forcing the fluid motion into quasi-two-dimensionality [81]. The former condition is typical for the dynamo problem, for example resulting in the amplification of a magnetic field by plasma turbulence. The latter is experienced in solar corona or terrestrial laboratory experiments with magnetic plasma confinement. To study the inherent properties of the non-linear interaction between turbulent fields $\mathbf{v}$ and $\mathbf{B}$, one needs to concentrate on turbulence with $E^K \sim E^M$ and a magnetic Prandtl number $P_m = \nu/\eta = 1$ [81].

1.5.3 The Ideal Invariants

If the turbulent system is closed with appropriate boundary conditions, there exists a number of invariants in the ideal limit of $\nu = \eta = 0$ [248]. For incompressible, three dimensional MHD these ideal invariants are described with their decay rates at finite viscosity and magnetic diffusivity:

total energy:

$$E = E^K + E^M = \frac{1}{2}\int_V \mathrm{d}V(v^2 + B^2), \qquad \dot{E} = -\int_V \mathrm{d}V(\mu\underline{\omega}^2 + \eta j^2), \tag{1.131}$$

magnetic helicity:

$$H^M = \frac{1}{2}\int_V \mathrm{d}V(\mathbf{A}\cdot\mathbf{B}), \qquad \dot{H}^M = -\eta\int_V \mathrm{d}V\,\mathbf{j}\cdot\mathbf{B}, \tag{1.132}$$

and

cross helicity:

$$H^C = \frac{1}{2}\int_V \mathrm{d}V(\mathbf{v}\cdot\mathbf{B}), \qquad \dot{H}^C = -\frac{\mu+\eta}{2}\int_V dV\,\underline{\omega}\cdot\mathbf{j}, \tag{1.133}$$

where $\mathbf{A}$ is the magnetic vector potential and $\mathbf{B} = \nabla\times\mathbf{A}$ [81].

The above ideal invariants play an important role in characterizing the macroscopic properties of MHD turbulence. The magnetic helicity H^M measures the linkage and twist of the magnetic field lines, while cross helicity H^C provides a measurement of the overall correlation of magnetic and velocity fields [81].

Chapter 2

Stretch-Twist-Fold in Magnetic Dynamos

2.1 Introduction

Magnetic fields are ubiquitous in the universe. Magnetic energy powers activities such as flares and coronal mass ejections in the sun and stars [195, 196, 197]. The galactic magnetic field plays an important role in star formation; in particular assisting in angular momentum transport, without which the sun and similar stars would not spin as slowly as they do today [193]. The magnetic fields in the Sun, galaxies and planets are generated and maintained by dynamo action, the process in which growth of the magnetic field is caused by the motion of the electrically conducting fluid, where the kinetic energy is converted into magnetic energy [23, 125, 127, 128, 168, 225, 247, 251, 259].

At the photosphere the solar magnetic field is concentrated into isolated elements, which are then grouped into active regions [112, 137]. The magnetic field in the Sun rises through its convective zone (**CZ**) in the form of isolated strands known as flux tubes [172]. Observations suggest that flux tubes emerging through the photosphere possess internal twist [17, 178]. This indicates that flux tubes carry electrical current (i.e. they have twisted field lines) prior to emergence. For example, Leka et al. [130] have shown that the current increases in proportion to the flux during the period of emergence. The twist in emerging flux tubes could originate deep in the convection zone as part of the dynamo process [37, 42] or could be present due to the effects of Coriolis forces on the rising flux [39, 137, 138]. Additional twist may be created in pre-existing flux due to surface motions such as differential rotation or shear motions [70, 239]. Vector magnetograms provide evidence that the coronal

magnetic field carries current. Some of these currents appear to propagate into the corona since the observations provide evidence that there is a good correlation between photospheric and coronal force-free field α coefficient [50, 177]. The linear force free field α parameter is taken as the ratio between the vertical current and the vertical magnetic field [17].

In order to calculate the linear force-free field α-coefficient, Pevtsov, Canfield, Metcalf [178] and Longcope, Fisher, Pevtsov [136] both used a photospheric active region vector magnetogram from the Haleakala Stokes Polarimeter (HSP; Mickey 1985) at Mees Solar Observatory. Their findings were, $\alpha < 0$ for 69% and 66%, respectively, of regions in the northern hemisphere and $\alpha > 0$ for $\sim 75\%$ and 62%, respectively, of those in the southern hemisphere. Pevtsov, Canfield and Metcalf [178] then concluded that magnitude of the average helicity increases with solar latitude, starting at zero near the equator, then reaching a maximum near $15^\circ - 25^\circ$ in both hemispheres, before decreasing to smaller values above $35^\circ - 40^\circ$.

The inherent twist in the emerging field lines may provide important information on the nature of the solar dynamo [198, 199]. We cannot see below the photosphere, although helioseismology [19, 109, 205, 224] provides extensive information on rotational velocities in the interior of the sun. Observing the emergence of twist and other helicity-containing structures (in either newly emerging flux or pre-existing flux) may prove to be an invaluable diagnostic for magnetic field dynamics in the solar dynamo [47, 66, 178, 179, 198].

The non-linear dynamics of a thin magnetic flux tube rising through the convection zone has been investigated by several authors [4, 56, 57, 75, 82, 215]. Numerical simulations of Spruit's equations suggest that the magnetic flux tube rises from the base of the convection zone in about 2-3 months [137]. These models follow from applying the ideal MHD equations presented in section 1.4 to a slender tube of flux. The tube is assumed slender in a sense that its cross-sectional radius is negligible compared to both the atmospheric scale height and any scale of variation along the tube. In Longcope and Klapper's model [137], the presence of some twist is essential in order to formulate a self-consistent picture of a flux tube. Without twist, a real flux tube would lack integrity and would not behave as a single object for very long [172]. Linear analysis [231] and numerical simulations [135, 206] confirm that an untwisted magnetic flux tube is quickly fragmented by hydrodynamic forces. When twisting the flux tube about its axis, the field lines provide a tension that helps to prevent this fragmentation [159].

The behaviour of thin flux tubes in a turbulent fluid provides excellent geometrical insights into the dynamo process. The stretch-twist-fold (STF) dynamo (figure 2.1) is a simple qualitative example of a fast dynamo [55, 155, 232, 233, 234, 255]. This dynamo starts by first stretching a closed flux tube in two dimensions to twice its length. If the flow is incompressible then the volume of the tube is preserved. In the next step, the rope is twisted into a figure 8 and then it is folded so that there are two loops with their fields pointing in the same direction and they occupy the same volume as the original flux tube. The two loops merge through small diffusive effects. This last step is important in the sense that the new field can not easily undo itself and therefore the whole process becomes irreversible. The newly merged loops are topologically the same as the original loop, with the field strength scaled up by a factor of 2.

After repeating the algorithm n times, the field in the flux tube grows by a factor of 2^n, or at a growth rate $T^{-1} \ln 2$ where T is the time for the STF steps. This makes the dynamo a fast dynamo, where the growth rate does not decrease with decreasing resistivity [155].

The twist part of the cycle allows the field in the folded loop to add coherently rather than cancelling. To twist the loop the motions need to leave the plane and go into the third dimension. The degree to which the flow twists the tube is important here. For instance, if the field were twisted too far, or not far enough, then the resulting field would not align itself with the original field. The net angle of rotation is governed by the geometry of the flow.

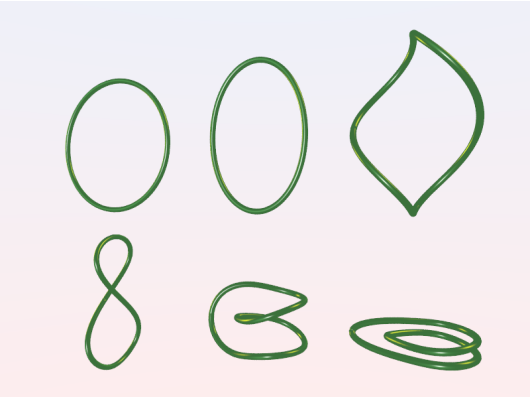

Figure 2.1: The stretch-twist-fold (STF) process.

The outline of this chapter is as follows. In sections 2.2-2.7, we analyse dynamos and their structure. Sections 2.8-2.10 then provide a review of stretch-twist-fold picture and a physical interpretation of fast dynamos.

2.2 Large and Small Scale Dynamos

The dynamo process is governed by the magnetic induction equation

$$\frac{\partial \mathbf{B}}{\partial t} = \nabla \times (\mathbf{U} \times \mathbf{B} - \eta \mathbf{J}), \tag{2.1}$$

where $\mathbf{U}$ is the fluid flow, $\mathbf{B}$ is the magnetic flux density and η is the magnetic diffusivity. The equation (2.1) has solution of the form $\mathbf{B} = \mathbf{b}(x, y, z)e^{(i\omega+p)t}$ where p is the dynamo growth rate. The induction equation gives the kinematics of the field and the dynamics of the field is given by the Lorentz force

$$\mathbf{J} \times \mathbf{B} = \mu_0^{-1}(-\nabla(\frac{1}{2}\,|\mathbf{B}|^2) + (\mathbf{B}\,.\,\nabla)\mathbf{B}), \tag{2.2}$$

where $\mathbf{J}$ is the current and μ_0 is the magnetic permeability in a vacuum.

Dynamos are divided into small-scale and large-scale dynamos. In the energy and helicity spectra calculations in chapter 3, the small wave-numbers are indicators of large-scale dynamos and large wave-numbers are the indicators of small-scale dynamos. Flows with significant amounts of kinetic helicity act as large-scale dynamos. At the largest scales there are sunspots and their active regions, extending over a significant fraction of the Sun's surface [58, 100]. Large-scale dynamos are thought to be responsible for the solar cycle [200]. They show large-scale spatial coherence, and in the case of the Sun, they show long-term temporal order. The typical length scale associated with large-scale solar magnetic field may correspond to the width of the mid-latitude toroidal flux belt [43, 45]. This belt extends about 30° in latitude, corresponding to about 300 Mm (1Mm = 1000km). The pressure scale height at the bottom of the convection zone is about 50 Mm, and all scales shorter than that may be associated with the small-scale field [46, 187]. Inhomogeneous and anisotropic flows are potential candidates for producing large-scale dynamo action [46].

The generation of large-scale magnetic field is generically accompanied by the rapid growth of small-scale fields. Small-scale dynamos produce magnetic fields that are correlated on scales smaller than the energy carrying scale of the turbulence [118]. At the smallest scale, there is evidence of a significant though intermittent field associated with active regions. Non-helical turbulent flows are an example of small-scale dynamos. Small-scale dynamos have a larger growth rate than large-scale dynamos. There may be a clear boundary between small and large-scale dynamos, however the two may interact [46, 187], and there are physical settings where large-scale dynamos do not work, for example in clusters of galaxies or in elliptical galaxies where rotation effects are negligible and therefore any turbulent flows lack helicity

and persistent shear. In such systems, the turbulence leads to small-scale dynamo action and generates relatively incoherent magnetic fields [23, 203].

2.3 The Solar Magnetic Field

The solar magnetic field appears in many different manifestations. For instance at the largest scales there are sunspots that were first systematically observed by Galileo [186]. He noted that the spots emerged in mid latitudes and they rotated at a rate dependent upon latitude (figure 2.2). He also recognized that the sunspots had a life time of about the order of one month. After Galileo, the sunspot observations became more systematic. The locations of sunspots were observed to have a cyclical component, with the median latitude decreasing in time over an 11 year cycle, and a new cycle then beginning at higher latitudes. This leads to the "butterfly diagram" (figure 2.3).

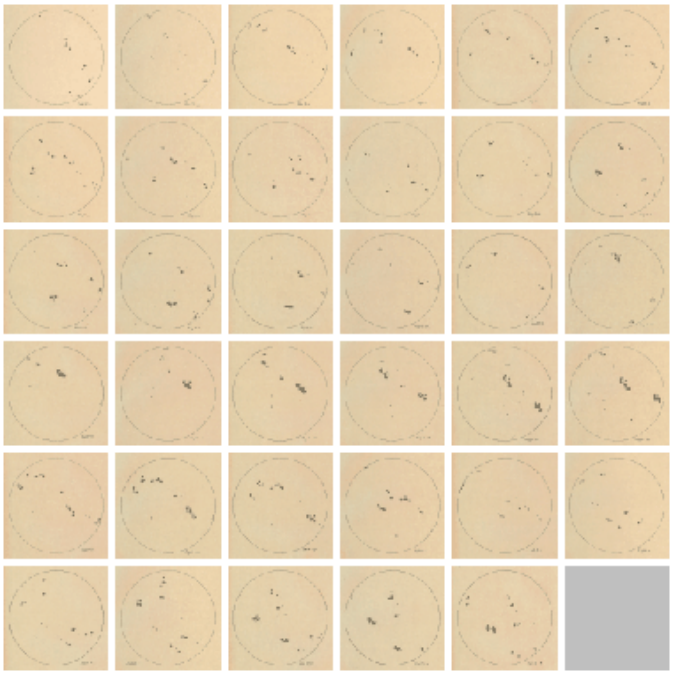

Figure 2.2: An early drawing of sunspots by Galileo. The drawings are thirty-six of Galileo's sunspot drawings and they illustrate the motion of sunspots across the disk which is actually a sequence showing the rotation of the Sun. The equator and rotation axis of the Sun can be determined after watching the direction of the sunspots over time. These observations were made at approximately the same time of day and the motion of the spots across the Sun can easily be seen. The images are taken from Professor Owen Gingerich's copy of the first edition of Istoria e Dimostrazioni.

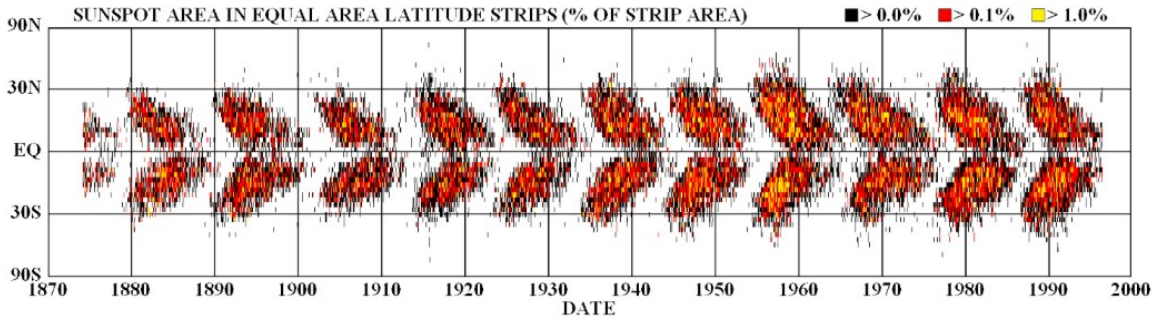

Figure 2.3: Solar butterfly diagram of the latitude of sunspot occurrence with time. Note the migration of sunspot activity from mid-latitudes toward the equator (courtesy of D. N. Hathaway).

In the butterfly diagram there is a cyclical effect, with near symmetry between the two hemispheres. The symmetry is not exact, and there are obvious modulations between cycles in the range of altitudes at which sunspots appear. Continuation of the record back in time shows that there have been periods of very low sunspot activity, such as the Maunder Minimum in the 17th century [186].

The measurements of the Sun's magnetic field started in 1913 by Hale's discovery of magnetic field lines in sunspots [186]. What followed was that sunspots are associated with large magnetic field lines of the order of 3000 Gauss. Sunspots are associated with magnetically active regions, which appear in pairs of opposite polarity, with the leading spots measured in the direction of rotation having different polarities in the north and southern hemispheres at any particular point in the cycle [46, 186]. The polarity is reversed every year, so that the approximate period of cyclic activity is about 22 years [95]. Another observation is that two sunspots in a pair tend to be tilted by $5^\circ - 10^\circ$ with respect to the equator so that the leading spot is closer to the equator (figure 2.4). This systematic effect has its origin in the dynamics of magnetic fields in a rotating system [222]. The tilt is consistent with the fact that a toroidal flux tube rises from deeper layers of the Sun to upper layers. At the upper layers of the Sun the density is less, therefore the tube develops an expanding flow field where as a result of Coriolis force reaches a clockwise swirl in the northern hemisphere and an anti-clockwise swirl in southern hemisphere [46].

It is important to note that not all active regions have a fully developed sunspot with a central dark umbra and a filamentary outer penumbra. There are smaller umbral type structures without penumbrae, typically with smaller fluxes, and sometimes there are no spots at all [186]. The sunspot number is a sensitive function of

the flux emerging in active regions.

At the solar surface the azimuthally averaged radial magnetic field is only a few Gauss. This is rather weak compared with the peak magnetic field in the sunspots. In the bulk of the convection zone, the magnetic field points mostly in the azimuthal direction because of differential rotation and is probably higher near the bottom of the convection zone due to an effect known as downward pumping [46].

The idea of downward pumping traces back to concepts such as flux expulsion, turbulent diamagnetism and topological pumping [227]. The turbulent pumping of magnetic flux by penetrative convection at the base of the convection zone is responsible for cyclical activities in the Sun [44, 73, 164, 226, 227]. The numerical simulations of three-dimensional, compressible, turbulent convection have unveiled the true dynamical nature of this pumping mechanism. The vigorous sinking plumes transport magnetic flux preferentially downwards out of the turbulent convecting region and into a stably stratified region below. This is where the flux can be increased and stored. The pumping mechanism is remarkably robust and works well when the convective stability of the low layer is reduced. Therefore one would expect the downward pumping by granular convection just beneath the solar surface to be particularly effective [223].

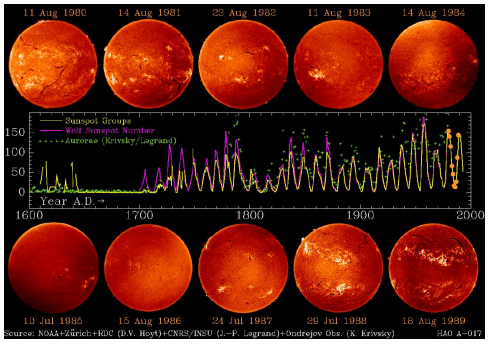

Figure 2.4: The plot is a historical reconstruction of yearly-averaged sunspot group counts (yellow curve), extending all the way back to the first telescopic sunspot observations in the early seventeenth century. The purple curve is the Zurich normalized sunspot number. The amplitude of the cycle, or the peak average number of sunspots seen in a given year, varies from one cycle to the next. Also the cycles are asymmetric, in that the rise from sunspot minimum to maximum occurs more rapidly than the subsequent fall from sunspot maximum to minimum. Another striking feature on this plot is the dramatically reduced number of sunspots observed in the time period spanning the years 1645 - 1715 (courtesy of NASA).

2.4 Fast and Slow Dynamos

The distinction between 'fast' and 'slow' dynamos was first introduced by Vainshtein and Zeldovich [234]. This distinction has been the basis for many published papers and books [55, 255]. Consider the velocity field $\mathbf{v}(x)$ that is characterized by a length scale L and a velocity scale v. We define two time-scales associated with the motion of the field, the advective time $\tau_A = L/v$ and the diffusion time $\tau_D = L^2/\eta$ (the quantity η is the magnetic diffusivity) [186]. In order to characterize the effects of a uniform magnetic field applied to a flow, using the definition of Reynolds number in section 1.1 and based on the equation (1.128), magnetic Reynolds number R_m is

$$R_m = \frac{\tau_D}{\tau_A} = \frac{vL}{\eta}, \tag{2.3}$$

where $\eta = 1/(\sigma\mu)$, σ is the electric conductivity of the fluid and μ is the fluid magnetic permeability. Also, there is a magnetic Prandtl number representing the ratio of R_m to the kinetic Reynolds number Re given by

$$P_m = \frac{\nu}{\eta} = \frac{R_m}{Re} \qquad , \qquad Re = \frac{vL}{\nu}, \tag{2.4}$$

and ν is the kinematic viscosity. The Sun operates at very large magnetic Reynolds number (table 2.1) and therefore it is important to consider its limiting behaviour when $R_m \to \infty$. A dynamo with growth rate p is said to be slow if $p \to 0$ as $R_m \to \infty$ and it is a fast dynamo if $p \to \text{const} > 0$ as $R_m \to \infty$ [95, 155]. This will be explained further in section 2.6. Also a fast dynamo is insensitive to the value of η as $\eta \to 0$. For most velocity fields that do not have chaotic paths, any resulting dynamo is always slow, however most turbulent flows result in fast dynamos. The evolved magnetic fields in fast dynamos are generally very highly structured, with a fractal or multifractal structure in the large R_m limit. If a fast dynamo reaches equilibrium due to dynamical interactions, it will not be fast or slow, but neutral since its growth rate is zero [186].

In table 2.1, the magnetic diffusivity is calculated from

$$\eta = 10^4 \left(\frac{T}{10^6 K}\right)^{-3/2} \left(\frac{\ln\Lambda}{20}\right) \text{cm}^2\text{s}^{-1}, \tag{2.5}$$

where $\ln\Lambda$ is a constant in the range of 5 and 20 (here it is assumed to be $\ln\Lambda = 20$) [46], the magnetic Prandtl number is obtained from

$$P_m = \frac{\nu}{\eta} = 1.1 \times 10^{-4} \left(\frac{T}{10^6 \text{K}}\right)^4 \left(\frac{\rho}{0.1\text{gcm}^{-3}}\right)^{-1} \left(\frac{\ln\Lambda}{20}\right)^{-2}. \tag{2.6}$$

Table 2.1: Provides summary of some important parameters in various astrophysical settings [46].

	T[K]	$\rho[gcm^{-3}]$	P_m	$\eta[cm^2s^{-1}]$	$v_{rms}[cms^{-1}]$	L[cm]	R_m
Solar CZ (upper part)	10^4	10^{-6}	10^{-7}	10^7	10^6	10^8	10^7
Solar CZ (lower part)	10^6	10^{-1}	10^{-4}	10^4	10^4	10^{10}	10^{10}
Galaxy	10^4	10^{-24}	10^{11}	10^7	10^6	10^{20}	10^{19}
Galaxy clusters	10^8	10^{-26}	10^{29}	10	10^8	10^{23}	10^{30}

The table also contains typical values of temperature and density in different astrophysical settings and rough estimates of typical rms velocities, v_{rms}, and eddy scales, L which are used in order to calculate magnetic Reynolds number R_m from equation (2.3) .

2.5 The Flow of Energy in Dynamos

The dynamo mechanism provides a means of converting kinetic energy into magnetic energy. Here, we focus on deriving the magnetic and kinetic energy equations.

By taking the dot product of equation (2.1) with $\mathbf{B}/(2\mu_0)$ and integrating over the volume V, we have

$$\frac{\mathrm{d}}{\mathrm{d}t}\int_V \frac{\mathbf{B}^2}{2\mu_0}\,\mathrm{d}V = -\int_V U\cdot(\mathbf{J}\times\mathbf{B})\,\mathrm{d}V - \int_V \frac{\mathbf{J}^2}{\sigma}\,\mathrm{d}V - \oint_{\partial V}\frac{\mathbf{E}\times\mathbf{B}}{\mu_0}\,\mathrm{d}\mathbf{S}. \tag{2.7}$$

This equation shows the magnetic energy increases if the work against the Lorentz force (the first term) increases, provided this term exceeds resistive losses or losses through the surface (the second and third terms) [46].

In order to derive the kinetic energy equation, we first define the momentum equation. It is the Navier-Stokes equation in fluid dynamics (1.1) supplemented by the Lorentz force, $\mathbf{J}\times\mathbf{B}$,

$$\rho\frac{D\mathbf{U}}{Dt} = -\nabla p + \mathbf{J}\times\mathbf{B} + \mathbf{f} + \mathbf{F}_{visc}, \tag{2.8}$$

where $\mathbf{U}$ is the velocity of gas, ρ is the density, p is the pressure, $\mathbf{F}_{visc}$ is the viscous force, and $\mathbf{f}$ subsumes all other body forces acting on the gas. By taking the dot product of the equation (2.8) with $\rho\mathbf{U}$, we arrive at the kinetic energy equation

$$\frac{\mathrm{d}}{\mathrm{d}t}\int_V \frac{1}{2}\rho\mathbf{U}^2\,\mathrm{d}V = +\int_V p\nabla\cdot\mathbf{U}\,\mathrm{d}V + \int_V \mathbf{U}\cdot(\mathbf{J}\times\mathbf{B})\,\mathrm{d}V + \int_V \rho\mathbf{U}\cdot\mathbf{g}\,\mathrm{d}V - \int_V 2\nu\rho\mathbf{S}^2\,\mathrm{d}V, \tag{2.9}$$

where $\mathbf{S}_{ij} = \frac{1}{2}(u_{i,j} + u_{j,i}) - \frac{1}{3}\delta_{ij}u_{k,k}$ is the traceless rate of strain tensor, and commas denote derivatives [46]. In order to avoid the loss of kinetic energy through the boundaries in (2.9), we have assumed stress-free boundary conditions with no surface terms. We note from the equation (2.7) and (2.9) that the generation of magnetic energy goes at the expense of kinetic energy, without loss of net energy [46].

There are four different energy reservoirs involved in the dynamo process: magnetic, kinetic, thermal, and potential energy. In accretion discs the magnetic energy comes ultimately from potential energy which is first converted into kinetic energy. In solar convection the energy comes ultimately from the nuclear reactions in the centre of the star. These act as a source of thermal energy which gets converted into kinetic energy via the convection instability.

2.6 Kinematic Dynamos

The magnetic induction equation (2.1) can be non-dimensionalised using the scale and turn-over time of the velocity field $\mathbf{U}$

$$\frac{\partial \mathbf{B}}{\partial t} = \nabla \times (\mathbf{U} \times \mathbf{B}) - R_m^{-1}\nabla^2\mathbf{B}, \tag{2.10}$$

where $R_m^{-1}\nabla^2\mathbf{B}$ is the diffusive term. In many astrophysical environments R_m is very large and in kinematic dynamo theory the velocity field $\mathbf{U}$ is fixed. There is a critical value of the magnetic Reynolds number R_m above which the magnetic field grows exponentially. A lot of work has been devoted to the question of whether the growth rate can remain finite in the limit $R_m \to \infty$. This is the so-called fast dynamo problem [55, 213, 191]. For a steady velocity field $\mathbf{U}$, the equation (2.10) has eigenfunctions of the form

$$\mathbf{B} = \mathbf{b}(x, y, z)e^{(i\omega+p)t}, \tag{2.11}$$

where p is the dynamo growth rate. As stated earlier, in the fast dynamos, p remains positive and bounded away from zero. The general motivation for the study of fast dynamo is that fast processes are observed in the non-linear solar dynamo, an example of which is the 22-year solar cycle where $R_m \sim 10^8$ [55].

In an idealized situation $R_m = \infty$, the fluid is perfectly conducting and magnetic energy will still grow in general, but magnetic helicity H is conserved as the field evolves. If for $R_m = \infty$, a growing eigenfunction of the form (2.11) can be defined, it must have zero helicity [155].

In the limit when magnetic Reynolds number is large but finite as $R_m \longrightarrow \infty$, helicity will be approximately conserved. Therefore, the normalized helicity should be small and tend to zero in this limit. Although the term R_m^{-1} multiplies the final, diffusive term in (2.10), this term is not generally neglected, since the field may adopt small-scales. Such small-scale field structures are evident in the Sun.

2.7 Magnetic Helicity

Magnetic helicity plays an important role in dynamo theory. It is an important observational tool in quantifying the complexity of the Sun's magnetic fields [46, 47]. The main information about the magnetic helicity of the Sun available to date is from surface magnetic fields, and these help us to identify some systematic trends. In particular, the vector magnetograms of active regions show negative (positive) current helicity in the northern (southern) hemisphere [18, 178, 179, 207].

Here, we give a brief account of magnetic helicity properties. It is the sum of the Gauss linking number over every pair of field lines within a volume [33]. The Gauss linking number is

$$\mathcal{L}_{12} = -\frac{1}{4\pi} \oint_1 \oint_2 \frac{d\mathbf{x}}{d\sigma} \cdot \frac{\mathbf{r}}{r^3} \times \frac{\mathrm{d}\mathbf{y}}{\mathrm{d}\tau}\, \mathrm{d}\tau\, \mathrm{d}\sigma, \tag{2.12}$$

where 1 and 2 are two interlinked curves, parametrized by σ and τ. The points on curve 1 and 2 are labelled $\mathbf{x}(\sigma)$ and $\mathbf{y}(\tau)$ and $\mathbf{r} = \mathbf{y} - \mathbf{x}$. The magnetic field contains an infinite number of field lines, each of them of infinitesimal flux. Some of these field lines fill a volume or surface while others form simple closed curves. Hence, the magnetic field is approximated in a closed volume as a set of N thin tubes. A closed volume is one in which magnetic field lines are fully contained, so the field has no component normal to the boundary, i.e. $\mathbf{B} \,.\, \mathbf{n} = 0$ [33]. If there are N tubes, each tube will carry a flux ψ_i, $i = 1, \ldots, N$, and the helicity is given by

$$H = \sum_{i=1}^{N} \sum_{j=1}^{N} \mathcal{L}_{ij} \psi_i \psi_j. \tag{2.13}$$

If N$\rightarrow \infty$ with $\psi_i \rightarrow 0$, after combining (2.12) and (2.13), then

$$H = -\frac{1}{4\pi} \int \int \mathbf{B}(\mathbf{x}) \cdot \frac{\mathbf{r}}{r^3} \times \mathbf{B}(\mathbf{y})\, \mathrm{d}^3x\, \mathrm{d}^3y. \tag{2.14}$$

Using Coulomb gauge vector potential

$$A(x) = -\frac{1}{4\pi} \int \frac{\mathbf{r}}{r^3} \times \mathbf{B}(\mathbf{y})\, \mathrm{d}^3y, \tag{2.15}$$

the helicity integral is reduced to

$$H = \int_V \mathbf{A} \cdot \mathbf{B} \, \mathrm{d}V. \tag{2.16}$$

Observe that magnetic helicity is a conserved quantity and is invariant under the gauge transformation $\mathbf{A}' = \mathbf{A} + \nabla\Lambda$, because

$$H' = \int_V \mathbf{A}' \cdot \mathbf{B}' \, \mathrm{d}V = H + \int_V \nabla\Lambda \cdot \mathbf{B} \, \mathrm{d}V = H + \oint_{\partial V} \Lambda \mathbf{B} \cdot \hat{\mathbf{n}} \, \mathrm{d}S, \tag{2.17}$$

where $\hat{\mathbf{n}}$ is the normal pointing out of the closed surface ∂V and the last term must vanish inside a magnetic surface when $\mathbf{B} \cdot \hat{\mathbf{n}} = 0$.

From Faraday's law, the evolution equation for $\mathbf{A} \cdot \mathbf{B}$ is

$$\begin{aligned} \frac{\partial}{\partial t}(\mathbf{A} \cdot \mathbf{B}) &= (-\mathbf{E} - \nabla\psi) \cdot \mathbf{B} + \mathbf{A} \cdot (-\nabla \times \mathbf{E}) \\ &= -2\mathbf{E} \cdot \mathbf{B} + \nabla \cdot (\psi\mathbf{B} + \mathbf{A} \times \mathbf{E}). \end{aligned} \tag{2.18}$$

Integrating the above equation over the volume V, we obtain

$$\frac{\mathrm{d}H}{\mathrm{d}t} = -2\int_V \mathbf{E} \cdot \mathbf{B} \, \mathrm{d}V + \oint_{\partial V} (\mathbf{A} \times \mathbf{B} + \psi\mathbf{B}) \cdot \hat{\mathbf{n}} \mathrm{d}S = -2\eta \, C, \tag{2.19}$$

where $C = \int_V \mathbf{J} \cdot \mathbf{B} \, \mathrm{d}V$ is the current helicity. Here, we have used the Ohm's law $\mathbf{E} = -\mathbf{U} \times \mathbf{B} + \eta\mathbf{J}$, in the volume integral and have assumed that the surface integral vanishes for closed domains [46].

Now, we define the relative helicity based on the paper of Berger and Field [34]. Consider the case where the space V is divided into two simply connected thin tubes of volume V_a and V_b separated by a boundary surface S. A divergence-free field $\mathbf{B}$ in volume V is denoted by the ordered pair $\mathbf{B} \equiv (\mathbf{B}_a, \mathbf{B}_b)$, the value of which at point x is

$$\mathbf{B}(x) = \begin{cases} \mathbf{B}_a(x) & \text{if } x \in V_a, \\ \mathbf{B}_b(x) & \text{if } x \in V_b. \end{cases} \tag{2.20}$$

To ensure $\nabla \cdot \mathbf{B} = 0$, it is required that $\mathbf{B}_a \cdot \hat{\mathbf{n}} = \mathbf{B}_b \cdot \hat{\mathbf{n}}$, where $\hat{\mathbf{n}} = \hat{\mathbf{n}}_a = -\hat{\mathbf{n}}_b$ is a unit normal pointing away from V_a.

The total helicity $H(\mathbf{B}_a, \mathbf{B}_b)$ inside V can be decomposed into contributions from two relative helicities, plus a term due to the potential fields

$$H(\mathbf{B}_a, \mathbf{B}_b) = H_R(V_a) + H_R(V_b) + H(\mathbf{P}_a, \mathbf{P}_b), \tag{2.21}$$

where $H_R(V_a)$ and $H_R(V_b)$ are the relative helicities of V_a and V_b respectively and $H(\mathbf{P}_a, \mathbf{P}_b)$ is the helicity due to the potential fields $\mathbf{P}_a$ and $\mathbf{P}_b$. The 'relative helicity of V_a', $H_R(V_a)$ is defined by

$$H_R(V_a) = H(\mathbf{B}_a, \mathbf{B}'_b) - H(\mathbf{P}_a, \mathbf{B}'_b), \tag{2.22}$$

where $\mathbf{P}_a$ is the potential field inside V_a and $\mathbf{B}'_b$ is an arbitrary field. Similarly, the 'relative helicity of V_b' is

$$H_R(V_b) = H(\mathbf{B}'_a, \mathbf{B}_b) - H(\mathbf{B}'_b, \mathbf{P}_b), \tag{2.23}$$

with $\mathbf{B}'_a$ an arbitrary field and $\mathbf{P}_b$ the potential field inside V_b.

This addition law can be generalized for relative helicities into the case where the space is divided into N simply connected volumes V_i, $i = 1, \ldots, n$. Let the magnetic field $\mathbf{B} = (\mathbf{B}_1, \ldots, \mathbf{B}_N)$ and $\mathbf{P}_i$ be the current free field determined by the normal field component at the boundary of V_i. The relative helicity is then given by

$$H_R(V_i) = H(\mathbf{P}_1, \ldots, \mathbf{P}_{i-1}, \mathbf{B}_i, \mathbf{B}_{i+1}, \ldots, \mathbf{B}_N) - H(\mathbf{P}_1, \ldots, \mathbf{P}_{i-1}, \mathbf{P}_i, \mathbf{B}_{i+1}, \ldots, \mathbf{B}_N). \tag{2.24}$$

2.8 Fast Dynamos: The Stretch-Twist-Fold Picture

We mentioned fast dynamos briefly in section 2.6. Here, we look at its physical interpretation. It is linked to the process of stretching, twisting and folding (STF) [234]. When STF is applied to a magnetic flux-tube in a perfectly conducting fluid, it will double the magnetic field strength. Thus the indefinite repetition of the STF sequence will lead to exponential growth of the magnetic field on a time-scale determined by that of the motion, and independently of the molecular diffusion process [54]. The STF sequence doubles the magnetic field-strength without increasing the cross-section of the flux-tube. This is similar to mapping the cross section on to itself. The stretching is usually associated with turbulent flow, twisting with convection in a rotating medium and folding with geometrical constraint on such convection. The degree that the field is twisted plays an important role in generating the dynamo. As mentioned at the start of the chapter, if the field were twisted too far, or not far enough, then the resulting field would not align itself with the original field. The angle of twist is governed by the geometry of the flow. Folding brings together a field that is largely aligned in the same direction, and the average field in a chaotic

region therefore grows exponentially with time. The STF sequence has some basis of reality in the turbulent convection within the convective zone of a rotating star [54].

To translate STF into a mathematical form, Moffatt and Proctor [155] represent the sequence as a three-dimensional time-dependent velocity field, where the STF process leading to fluctuations in the magnetic field is a periodic motion. They consider the centre line of the flux tube to be the circle $x^2 + y^2 = a_0^2$ in the plane $z = 0$ (figure 2.5(a)), and its cross section to be a circle of radius $c \ll a_0$ while also assuming that the diffusion is totally negligible, $\eta = 0$. In this section, we review the Moffatt and Proctor stretch-twist-fold sequence [155].

2.8.1 Stretch

Moffatt and Proctor achieve the process of stretching (figure 2.5(b)) by the uniform incompressible straining field

$$\mathbf{v}_1(x) = (\alpha x, \alpha y, -2\alpha z), \tag{2.25}$$

with $\alpha > 0$. As a result, the equation of the field in three dimensions becomes

$$\begin{aligned} \frac{\mathrm{d}x}{\mathrm{d}t} &= \alpha x \Rightarrow x(t) = x_0\, e^{\alpha t}, \\ \frac{\mathrm{d}y}{\mathrm{d}t} &= \alpha y \Rightarrow y(t) = y_0\, e^{\alpha t}, \\ \frac{\mathrm{d}z}{\mathrm{d}t} &= -2\alpha z \Rightarrow z(t) = z_0\, e^{-2\alpha t}, \end{aligned} \tag{2.26}$$

and the radius of the flux tube increases exponentially under the action of the field

$$a(t) = a_0 e^{\alpha t}. \tag{2.27}$$

As an example, consider the circular flux tube in the $y = 0$, $t = 0$, $x_0 = z_0 = c$ plane (figure 2.6(a)), then after stretching (figure 2.6(b)), at time t, the points P, Q, R and S have the following coordinates:

$$\begin{aligned} P &= ((a_0 + c)e^{\alpha t}, 0, 0), \text{ semiaxis in } x \text{ direction with length } ce^{\alpha t}, \\ Q &= (0, 0, ce^{-2\alpha t}), \quad \text{semiaxis in } z \text{ direction with length } ce^{-2\alpha t}, \\ R &= ((a_0 - c)e^{\alpha t}, 0, 0), \text{ semiaxis in } x \text{ direction with length } -ce^{\alpha t}, \\ S &= (0, 0, -ce^{-2\alpha t}), \end{aligned} \tag{2.28}$$

where the ratio $ce^{\alpha t}/ce^{-2\alpha t} = e^{3\alpha t}$.

It is important to note that at the time $t_1 = \alpha^{-1} \ln 2$, the radius is doubled and the cross section of the tube is flattened by the strain into an ellipse (figure 2.5(b))

$$\frac{1}{4}(x - 2\alpha_0)^2 + 16z^2 = c^2, \tag{2.29}$$

with semiaxes in the ratio of 8 to 1. The volume of the flux tube, however, remains constant at $V \approx 2\pi^2 c^2 a_0$.

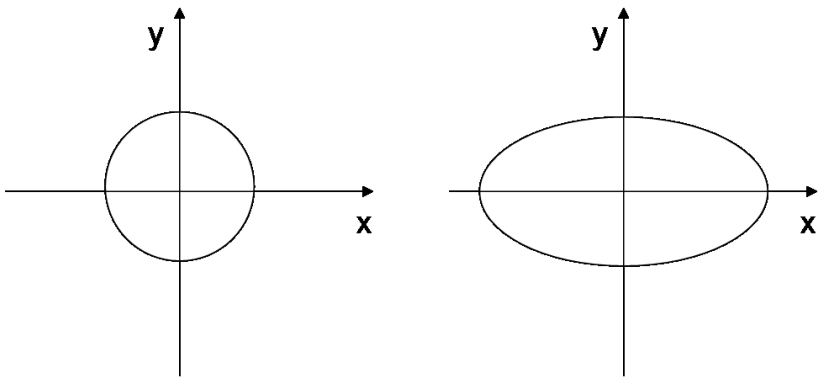

(a) (b)

Figure 2.5: Stretching of a circular flux tube in the xy plane.

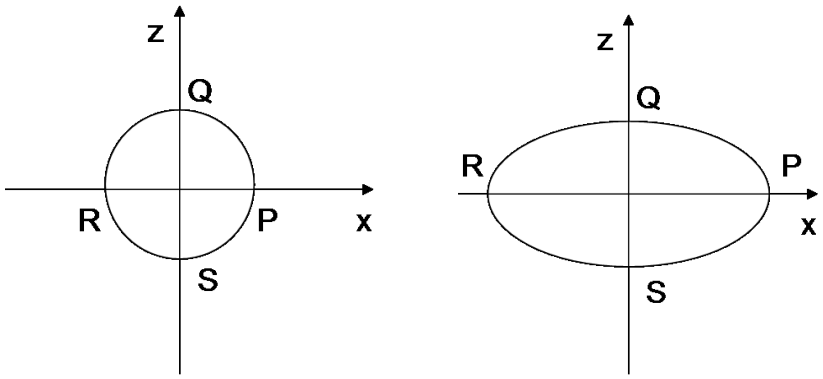

(a) (b)

Figure 2.6: Stretching of a circular flux tube in the xz plane.

2.8.2 Twist

Moffatt and Proctor present the twist about the x-axis (figure 2.7) by the velocity field

$$\mathbf{v}_2(x) = (0, -\omega(x)\, z, \omega(x)\, y), \tag{2.30}$$

where $\omega(x)$ is antisymmetric about $x = 0$. Solutions to equations

$$\begin{aligned} x(t) &= \int v_x(t)\, \mathrm{d}t, \\ y(t) &= \int v_y(t)\, \mathrm{d}t, \\ \text{and } z(t) &= \int v_z(t)\, \mathrm{d}t, \end{aligned} \tag{2.31}$$

are obtained by going to the second derivative in time. The simplest possibility of uniform twist is when $\omega(x) = -fx$ where f is constant. For a right-handed twist, $f > 0$, the twist as a function of f is

$$\mathbf{v}_2(x) = (0, fxz, -fxy). \tag{2.32}$$

If the object we are twisting is an elastic band or paper tape, then it may be difficult to achieve the twist at the midpoint of the elliptic cross section since these materials have a natural resistance to stretching. However such condition does not arise in magnetic flux tubes so long as the Lorentz force is negligible. Also a strong magnetic field subject to twist would respond in a nearly inextensible manner so that, in a dynamic regime in which Lorentz forces are important, the elastic-band analogy may then be more relevant.

To achieve the twist at the points A and B (figure 2.7), the twist field (2.32) is compressed along the y-axis by the strain field $\mathbf{v}_3(x)$. This leaves the scale of the loop along the x-axis undisturbed. The two dimensional strain field is

$$\mathbf{v}_3(x) = (0, -\beta y, \beta z), \tag{2.33}$$

with $\beta > 0$. If the fields $\mathbf{v}_2$ and $\mathbf{v}_3$ act simultaneously for a time $t_2 = \pi/4a_0 f$, then the distance between the points A and B will be reduced to $\delta = 2a_0 e^{-\beta t_2} = 2a_0 e^{-\pi\beta/4a_0 f}$. However, here a flux tube with an initially elliptic cross-section is twisted and not simply a closed curve. As the figure 2.7 demonstrates, a right-handed twist applied to a paper tape induces a left-handed twist of the tape about its own centreline. If the tape is broken and reconnected at the points A and B (simulating the diffusion process), then the two loops have created a form of Möbius strip, where each one will have a net left-handed twist of π.

Finally, as a result of the action of the velocity field $\mathbf{v}_2(x) + \mathbf{v}_3(x)$, the flux tube will develop what is described as 'intrinsic twist'. Once the reconnection takes place, this intrinsic twist manifests itself as the helicity of the magnetic field.

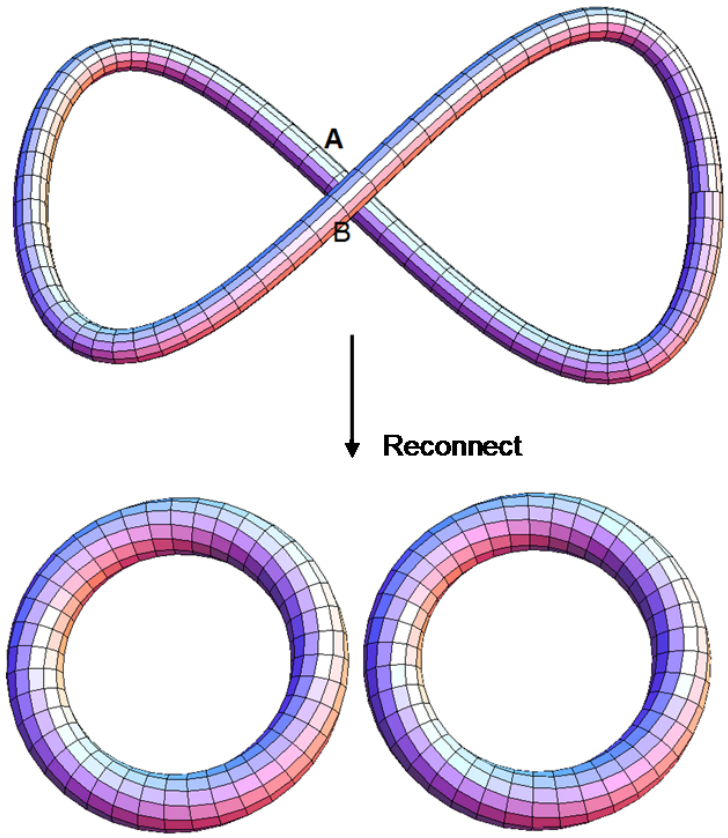

Figure 2.7: Twisting and reconnection of a flux tube of circular cross-section. The figure eight has a helicity of 1. By conservation of helicity [34] each circular tube has a twist of 0.5.

2.8.3 Fold

The action of folding two loops (figure 2.8) is described by the velocity field $\mathbf{v}_4(x)$

$$\mathbf{v}_4(x) = (-\gamma x, \gamma y + gx^2, 0), \tag{2.34}$$

with $\gamma > 0$, $g > 0$. The gx^2 term deforms the loops out of the (x, z)plane, and the remaining part of the equation (2.34) compresses both loops towards each other on the (y, z)-plane. A small value of g ($ga_0 \ll \gamma$) is sufficient to achieve the necessary effect, in a time interval of t_4 satisfying $\gamma t_4 \gtrsim 1$.

Now there is a double loop in the (y, z)-plane. In order to complete the process and return to the initial configuration, a translation of order a_0 and a rotation of $\pi/2$ about the y-axis is required. This is achieved with the velocity field

$$\mathbf{v}_5(x) = (0, \omega, 0) \wedge x - (0, U, 0), \tag{2.35}$$

with $U \approx 2a_0\,\omega/\pi$ in a time $t_5 = 2\omega/\pi$.

When applying the velocity fields $\mathbf{v}_1(x), \mathbf{v}_2(x), \ldots, \mathbf{v}_5(x)$ in succession and over suitable time intervals, we achieve an approximate doubling of the initial magnetic field. However, this happens at a cost of generating a net twist in both of the new flux tubes. If these velocity fields act simultaneously so that there is steady velocity field

$$\begin{aligned} \mathbf{v}(x) &= \mathbf{v}_1(x) + \mathbf{v}_2(x) + \ldots + \mathbf{v}_5(x) \\ &= (\alpha' x + \omega z, \beta' y + gx^2 + fxz - U, \gamma' z - \omega x - fxy), \end{aligned} \tag{2.36}$$

where

$$\alpha' = \alpha - \gamma, \;\; \beta' = \alpha + \gamma - \beta, \;\; \gamma' = -2\alpha + \beta, \tag{2.37}$$

then the initial loop should continuously deform in a similar way and the doubling process should be repeated again and again so long as the velocity field (2.36) is sustained. The trajectories associated with equation (2.36) are

$$\begin{aligned} \frac{\mathrm{d}x}{\mathrm{d}t} &= \alpha' x + \omega z, \\ \frac{\mathrm{d}y}{\mathrm{d}t} &= \beta' y + gx^2 + fxz - U, \\ \frac{\mathrm{d}z}{\mathrm{d}t} &= \gamma' z - \omega x - fxy, \end{aligned} \tag{2.38}$$

where $\alpha' + \beta' + \gamma' = 0$. The approaching of the two loops in the twist and fold process is achieved if $\alpha' < 0$ and $\beta' < 0$.

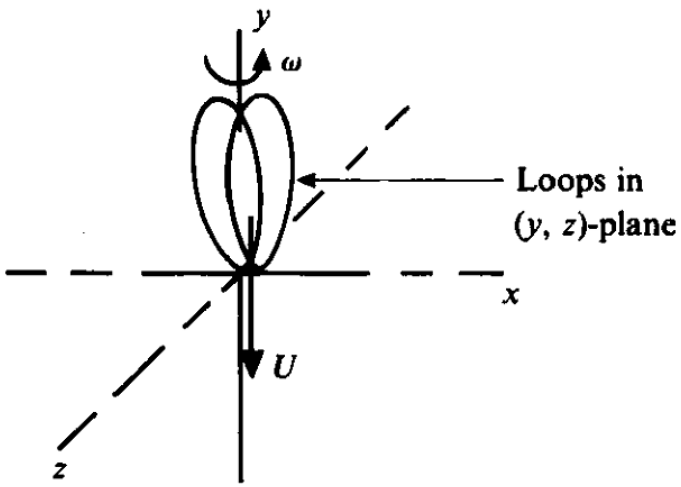

Figure 2.8: Folding of two loops with translation U and rotation ω. Figure from Moffatt and Proctor [155].

The vorticity associated with the velocity field in (2.36) is

$$\omega(x) = (-2fx, 2\omega + fy, 2gx + fz), \tag{2.39}$$

and the helicity, integrated over any sphere $|\mathbf{x}| < R$ is given by

$$H(R) = \int_{|x|<R} \mathbf{v} \cdot \omega \, \mathrm{d}V = -\frac{4}{5}\pi R^5 f\alpha'. \tag{2.40}$$

The motion therefore has a net right-handed or left-handed sense according to whether $f\alpha' < 0$ or > 0. The helicity (2.40) together with weak diffusion is responsible for generating helicity of opposite sign in the magnetic field.

The motion (2.36) is unbounded at infinity and there is no guarantee that the trajectories of fluid particles will remain within a sphere $r < R$, no matter how large R may be. Therefore the velocity field (2.36) is modified so that nearly all of the trajectories return to the neighbourhood of the origin. To achieve this, consider $\mathbf{A}(x)$ as the vector potential of $\mathbf{v}(\mathbf{x})$, which is a cubic function of the coordinates

$$\mathbf{A}(x) = [gx^2z - Uz + \frac{1}{2}fx(z^2 + y^2), \gamma zx - \frac{1}{2}\omega(x^2 + z^2), -\beta xy]. \tag{2.41}$$

The modified vector potential is defined as

$$\mathbf{A}^M(\mathbf{x}) = \mathbf{A}(\mathbf{x})e^{-r/R}, \tag{2.42}$$

and the modified (solenoidal) velocity field is given by

$$\mathbf{v}^M(\mathbf{x}) = \nabla \wedge \mathbf{A}^M(\mathbf{x}). \tag{2.43}$$

Note that $\mathbf{v}^M$ coincides with $\mathbf{v}$ for $r \ll R$, but since it is exponentially small for $r \gtrsim R$, nearly all of the stream lines are forced to return to the interior of the sphere $r = R$. Consequently, any magnetic field that is initially confined to the sphere $r \lesssim R$ will probably remain confined for all time under the frozen field assumption.

It is important to consider what happens when the STF cycle is repeated. The stretch is now applied to two adjacent flux tubes each of 8:1 elliptical cross section twisted in the form of a Möbius strip. The initial stretch in the (x, y)-plane again flattens the cross section, where the long axis of the ellipse is initially parallel to the plane. The ellipse is then further stretched until its axes are in the ratio 64:1. Where the long axis is initially perpendicular to the plane, the cross section returns to the original circular form (but with 1/4 of the original radius). The twist about the x-axis again induces additional intrinsic twist in the flux tube where there is the twisting and reconnection of a Möbius strip (twist π) and a strip with twist 2π. In the case of flux tubes, if symmetry is maintained between the two daughter tubes, then each will have a twist of $3\pi/2$. The repetition of folding stage leads to the superposition of these two tubes, which will be linked with the neighbouring tubes.

Even after only two stretch, twist and fold cycles, a field of considerable complexity is generated. For a toroidal flux that has increased fourfold, a poloidal field varying on a scale $1c/64$ has been generated and after n cycles the scale of variation would be $c/2^{3n}$. This is indeed an exponential decrease of scale $l_B \sim ce^{-t/t_0}$, where t_0 is the time-scale of the stretch-twist-fold cycle. The molecular diffusion, neglected so far, will result in eliminating these field variations as well achieving the reconnection of flux tubes. It is important to remember the field dealt with here is a fast diffusive dynamo rather than the non-diffusive type.

Suppose that the initial stretch (2.25) is maintained for a long time until the smaller dimension of the cross-section of the tube is reduced to $O(\eta/\alpha)^{\frac{1}{2}}$. At this cross section the magnitude of diffusion becomes important. The length scale does not reduce further. However, the larger dimension of the cross-section continues to increase like $e^{\alpha t}$ and since the total toroidal flux in the tube is constant during the stretch process, the field intensity must decrease like $e^{-\alpha t}$. Indeed the relevant local solution of equation (2.10) with the velocity field given by (2.25) is $\mathbf{B} = (0, B(z,t), 0)$ with

$$B(z,t) = B_0\, e^{-\alpha t}\, e^{-\alpha z^2/\eta}. \tag{2.44}$$

The behaviour in which the decrease of scale in one direction is limited by molecular diffusion has been discussed in the context of scalar-field diffusion by Batchelor [20] and its importance in dynamos has been emphasized by Zeldovich [254]. On a length scale as small as this in the stretch-twist-fold cycle, the toroidal field is not doubled - it is halved. The toroidal flux however is doubled, because there are now two adjacent flux tubes each with double the original cross-section. Repetition of the cycle results in continued increase of the net cross-section, and the structure of the field that finally emerges from many repetitions will be very different from the initial simple circular flux tube of small cross-section.

2.9 The α Effect

Central to the discussion of large-scale dynamos is the so-called alpha effect. It explains the generation of a mean field if the turbulence lacks mirror symmetry, e.g. if the flow has kinetic helicity. Turbulent flows recreate poloidal magnetic flux from the toroidal field [126, 154, 255]. The overall effect of turbulence is highly non-linear; however, to a first approximation the flows create an efficient electromotive force

$$\underline{\xi} = \alpha \mathbf{B} - \beta \nabla \times \mathbf{B}, \tag{2.45}$$

where $\mathbf{B}$ is the mean magnetic field [37]. In classical dynamo theory α is the result of kinetic helicity and β corresponds to turbulent diffusion. Considering the time derivative of helicity (2.19), the electric field becomes $\mathbf{E} = -\underline{\xi}$. Therefore α can modify the helicity of the mean field [201, 208]. The appearance of the electromotive force is known as the 'α effect'. It is at the heart of dynamo theory. The reason is that it provides the means for the dynamo cycle $\mathbf{B}_P \rightleftharpoons \mathbf{B}_T$ to be completed as the toroidal field $\mathbf{B}_T$ can be generated from poloidal field $\mathbf{B}_P$ by the process of differential rotation.

After series expansion of (2.45), one can write

$$\xi^{(0)} = \alpha \mathbf{B}_0, \tag{2.46}$$

and from Ohm's law $\mathbf{J} = \sigma(\mathbf{E} + \mathbf{v} \times \mathbf{B})$ with σ the electric conductivity, we have

$$\mathbf{J}^{(0)} = \sigma \xi^{(0)} = \sigma \alpha \mathbf{B}_0, \tag{2.47}$$

where $\mathbf{J}^{(0)}$ is the mean current density. In terms of mean fields, equation (2.47) demonstrates that the α effect generates toroidal current and, as a result, a poloidal field from the toroidal field [154].

2.10 Helicity in the Beltrami Dynamo

The property of fluid motion crucial to dynamo action is kinetic helicity. Helicity in simple terms is the imbalance between the right-handed and left-handed helical motion. A flow that has maximal kinetic helicity and, for this reason is of particular interest, is the Beltrami flow. A Beltrami flow satisfies $\nabla\wedge\mathbf{v} = k_0\mathbf{v}$, where k_0 is constant. This is similar to the force-free field structure ($\nabla \wedge \mathbf{B}_0 = k\mathbf{B}_0$). The helical wave

$$\mathbf{v}_1(x,t) = (0, U_1\sin(k_0x - \omega_1 t), U_1\cos(k_0x - \omega_1 t)), \tag{2.48}$$

satisfies the Beltrami condition, and its kinetic helicity is

$$H_1 = \langle \mathbf{v}_1 \cdot \nabla\wedge\mathbf{v}_1\rangle = k_0\, U_1^2. \tag{2.49}$$

Similarly, $\mathbf{v}_2$ and $\mathbf{v}_3$ are

$$\mathbf{v}_2(x,t) = (U_2\cos(k_0y - \omega_2 t), 0, U_2\sin(k_0y - \omega_2 t), \tag{2.50}$$

$$\mathbf{v}_3(x,t) = (U_3\sin(k_0z - \omega_3 t), U_3\cos(k_0z - \omega_3 t), 0), \tag{2.51}$$

and the velocity field

$$\mathbf{v}(x,t) = \mathbf{v}_1(x,t) + \mathbf{v}_2(x,t) + \mathbf{v}_3(x,t), \tag{2.52}$$

satisfies $\nabla\wedge\mathbf{v} = k_0\,\mathbf{v}$ and has helicity

$$H = \langle \mathbf{v}\cdot\nabla\wedge\mathbf{v}\rangle = k_0\,(U_1^2 + U_2^2 + U_3^2). \tag{2.53}$$

The flow (2.52) is an exact solution of the Euler equation in a rotating fluid. The Euler equation in a frame rotating with angular velocity Ω may be written as

$$\frac{\partial\mathbf{v}}{\partial t} + 2\Omega\wedge\mathbf{v} = -\nabla(\frac{p}{\rho} + \frac{1}{2}\mathbf{v}^2) + \mathbf{v}\wedge\omega, \tag{2.54}$$

and it is satisfied by (2.52) if

$$\Omega = -\frac{1}{2}(\omega_1,\omega_2,\omega_3), \tag{2.55}$$

and if p is chosen suitably. When $\omega_1 = \omega_2 = \omega_3 = 0$, the flow is steady.

Flows of this type are capable of dynamo action on length scales L large compared with k_0^{-1} [53, 190]. As discussed in section 2.9, there is an α associated with the motion (2.52) and that is given by the tensor [154]

$$(\alpha_{ij}) = \begin{pmatrix} \alpha^{(1)} & 0 & 0 \\ 0 & \alpha^{(2)} & 0 \\ 0 & 0 & \alpha^{(3)} \end{pmatrix},$$

where

$$\alpha^{(n)} = -\frac{\eta U_n^2 k_0^2}{\omega_n^2 + \eta^2 k_0^4} \ \ (n = 1, 2, 3). \tag{2.56}$$

When the frequencies ω_n are non-zero, $\alpha^{(n)} \to 0$ as η(magnetic diffusivity)$\to 0$. This is a property that persists at all higher orders of perturbation theory [71], and as a result the flow is not a fast dynamo.

For simplicity, consider the isotropic situation where

$$U_1 = U_2 = U_3 = U, \qquad \omega_1 = \omega_2 = \omega_3 = \omega, \tag{2.57}$$

then $\alpha_{ij} = \alpha\delta_{ij}$, where

$$\alpha = -\frac{\eta k_0 H}{3(\omega^2 + \eta^2 k_0^4)}. \tag{2.58}$$

The increase in the molecular diffusivity is similarly

$$\beta = \frac{2\eta k_0 E}{3(\omega^2 + \eta^2 k_0^4)}, \tag{2.59}$$

where $E = 3U^2/2$ is the mean kinetic-energy density of the motion ($H = 2k_0 E$) [155]. It is important to note that

$$\frac{|\alpha|}{\beta} = O\left(\frac{|H|}{E}\right) = O\left(k_0\right), \tag{2.60}$$

and this is expected to hold at higher orders of perturbation theory.

The evolution of the field $\mathbf{B}_0$ on a large-scale compared with k_0^{-1} is described by

$$\frac{\partial \mathbf{B}_0}{\partial t} \approx \alpha \nabla \wedge \mathbf{B}_0 + (\eta + \beta)\nabla^2 \mathbf{B}_0. \tag{2.61}$$

This has non-oscillatory dynamo solutions of force-free structure ($\nabla \wedge \mathbf{B}_0 = K\mathbf{B}_0$) whose growth rate p is given by

$$p = \alpha K - (\eta + \beta)K^2. \tag{2.62}$$

The maximum growth rate occurs for

$$K = K_m = \frac{|\alpha|}{2(\eta + \beta)}, \tag{2.63}$$

and, by adopting expressions from (2.58) and (2.59), then

$$\frac{K_m}{k_0} = \frac{U^2 k_0^2}{2[U^2 k_0^2 + (\omega^2 + \eta^2 k_0^4)]}, \tag{2.64}$$

so that $K_m \ll k_0$, as required for self-consistency of the approximation (2.61) provided that

$$\omega^2 + \eta^2 k_0^4 \gg U^2 k_0^2. \tag{2.65}$$

As U increases (for fixed ω and η), there is a decrease in the growth of the field $\mathbf{B}_0$ towards the scale k_0^{-1} of the velocity field, and the approximate methods of mean-field theory become less reliable [155].

An alternative approach [5, 91] would be to restrict attention to a field $\mathbf{B}(\mathbf{x}, t)$ with the same periodicity as the field $\mathbf{v}$ and with zero mean over a basic cube of side $2\pi/k_0$. In spectral terms, the spectrum of $\mathbf{B}$ may peak at wave numbers of order k_0, but the spectrum of $\nabla \wedge \mathbf{B}$ will have strong contributions at wave numbers of order $R_m^{\frac{1}{2}} k_0$, where R_m is the magnetic Reynolds number associated with the flow. This is consistent with the statement of Galloway and Frisch [91] that "spectra of the growing or decaying modes show that the value of the wave-number k at which energy peaks is surprisingly insensitive to R, though the length of the tail appears to increase roughly as the square root of R". The magnetic spectrum $M(k)$ has a power law dependence of the form

$$M(k) \approx k^{-q}, \quad 0 < q \leq 3, \tag{2.66}$$

in the range of wave-numbers $k_0 \ll k \ll R_m^{\frac{1}{2}} k_0$.

If the process of field distortion is similar to the stretch-twist-fold dynamo then the fluctuation of $\nabla \wedge \mathbf{B}$, generated at any scale k^{-1}, is related to the twist effective at that scale and, for the motion (2.52), this twist is independent of k. This results in $(k^2 M(k))\, k$ being independent of k, i.e. $q = 3$ in (2.66) and it leads to $k^2 M(k)$ becoming logarithmically divergent as $\eta \to 0$, corresponding to the non-analytical character of the magnetic field in this limit. The results available at present suggest that $M(k)$ in fact falls off more slowly than k^{-3} in the range of $k_0 \ll k \ll R_m^{\frac{1}{2}} k_0$ [155].

Chapter 3

Stretch-Twist-Fold Picture in a Thin Flux Tube

3.1 Introduction

This chapter looks at the influence of writhe in the stretch-twist-fold (STF) dynamo. We consider a thin flux tube distorted by simple stretch, twist, and fold motions and calculate the helicity and energy spectra. The results of this chapter have been published in the following journal [10].

A thin flux tube can be specified by the geometry of its central axis, the radius (and net magnetic flux) of the tube surrounding the axis, and a twist function: how much field lines twist about the axis as a function of position along the axis. We ignore the distribution of flux or twist in the radial direction. The axis geometry can be described locally in terms of two intrinsic quantities, the curvature and torsion. In addition, there are three important global quantities, the *twist number*, the *writhe* [34, 156, 35] (briefly, a measure of coiling), and the *helicity*, the measure of linking number of the field lines averaged over all pairs of field lines, and weighted by flux [153]. Longcope and Klapper [137] have developed a detailed theory of the evolution of a thin flux tube in terms of these geometric quantities. In particular, they allow the distribution of twist to vary along the axis of the tube.

For the purposes of this chapter, we make a strong simplification: we assume that the twist will at all times be uniformly distributed. Uniform distribution of twist is valid in an equilibrium situation [137, 172]. In a dynamic situation, the assumption will be justified if the time-scale for relaxation to a uniform distribution of twist is small compared to the time-scales for evolution of the shape of the tube axis. As

redistribution of twist operates at near Alfvén speeds this difference in time-scales should be valid for tube motions much slower than the Alfvén speed.

The growing complexity of the field in the STF process can be characterized by the evolution of the magnetic helicity [234]. This is discussed in [46] and [95] where repeated application of the STF cycle leads to a large-scale *writhe helicity* associated with the repeated crossings of the flux tube and oppositely signed *twist helicity* at a much smaller scale.

Suppose that the twist process proceeds as in figure 3.1 (rather than the mirror image process). Gilbert [95] notes that after folding, the twisted rope has a writhe of approximately $\mathcal{W} \approx -1$. This gives the writhe contribution to the helicity of $H_{\rm wr} \approx -1$. There is a compensating twist of field lines inside the tube, giving a twist of $+1$, and the twist contribution to the helicity is $H_{\rm tw} = +1$. These figures assume that the fold part of the cycle returns the field to a nearly flat state. If the field shape is more three-dimensional, then the writhe and twist must be calculated more carefully, as will be done in section 3.4. The total helicity after one STF step is $H = H_{\rm wr} + H_{\rm tw} = 0$. Gilbert suggests that the two forms of helicity are associated with different scale of the field. The positive twist helicity is associated with the tube's internal structure, presumably at small-scales, whereas the negative writhe helicity is related to the coiling of the tube at a larger scale.

Large-scale dynamos produce small-scale helical fields as a waste product that quench the large-scale dynamo and hence quench the alpha effect [41, 84]. If most of the helicity of the solar magnetic field were produced by the α effect, then one would expect much of the solar magnetic field to be bi-helical [39, 40, 135, 252], in that the field generated by the α effect has positive and negative magnetic helicity at different scales, but hardly any net magnetic helicity. To the extent that the helical structure lies in individual tubes (rather than linking between tubes) these different scales of helicity could manifest themselves in the twist and writhe structure. Evidence for bi-helical fields can be seen in the fact that bipolar regions are tilted according to Joy's law [75, 101], suggesting the presence of positive magnetic helicity in addition to the negative magnetic helicity usually found in northern active regions.

On the other hand, if most of the Sun's helicity is caused by differential rotation [37], the helicity in each hemisphere would have a strong dominant sign (negative in the north). Hence, the differential rotation causes segregation of magnetic helicity in

physical space, i.e. between north and south, while the α effect causes a segregation of helicity in wave-number space.

An emerging flux tube can carry helicity either as an internal twist within the tube, or as writhe [140]. To assist in interpreting both dynamo theory and observations of emerging helical structure, we investigate how the decomposition of helicity into twist and writhe (defined in section 3.2) relates to the helicity and energy spectra. Consider an STF dynamo with right-handed twisting motions (corresponding to the effects of Coriolis forces in the northern hemisphere of the Sun). According to Gilbert [95] and Brandenburg and Subramanian [46], the STF process generates negative helicity at the large-scales, and positive helicity at small-scales. The large-scale helicity is then interpreted as writhe, while the small-scale helicity corresponds to twist. We wish to test this interpretation with explicit calculations.

The outline of this chapter is as follows. In section 3.2, we review the magnetic helicity, twist, and writhe of flux tubes. This section also gives a review of the helicity and energy spectra. Then, in sections 3.3-3.4, we provide details of our thin flux tube model, present our calculations of magnetic energy and magnetic helicity and the subsequent numerical simulations of helicity in the STF picture. Conclusions are given in section 3.5.

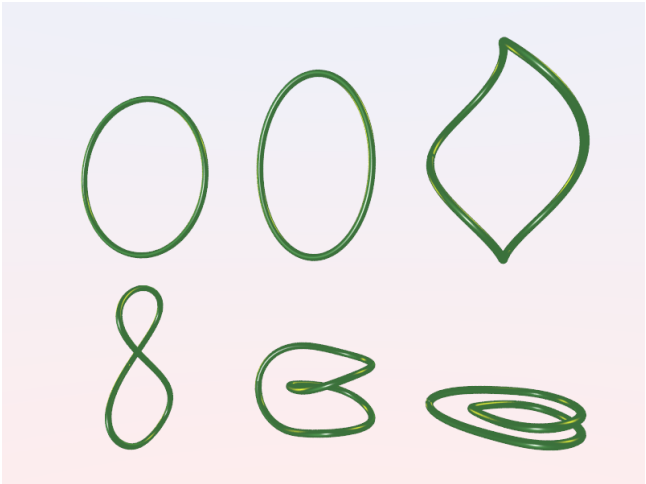

Figure 3.1: The stretch-twist-fold (STF) process. Top row: An initial circular flux tube ($\mathcal{W} = 0$) is stretched ($\mathcal{W} = 0$) and twisted ($\mathcal{W} = 0.295$). Bottom row: The tube is compressed into a figure 8 ($\mathcal{W} = 0.739$), folded ($\mathcal{W} = 1.12$), and compressed again ($\mathcal{W} = 1.15$). Writhe can be computed by counting the (signed) number of crossings seen in a plane projection, then averaging over all projection angles. Thus, for the figure 8, a positive crossing is seen from 74% of all projection angles. Note that the last two tubes have a writhe slightly >1; from some angles these tubes exhibit two crossings (e.g. if rotated from their present positions by 45° about the vertical).

3.2 Helicity, Twist, and Writhe

3.2.1 Definitions

We described in section 2.7, the Gauss linking number $\mathcal{L}$ as the measure of the linking of two curves [79]. Similarly, Magnetic helicity H was interpreted as the average linking of pairs of magnetic field lines. Here, we consider a closed tube of magnetic field lines with axial flux ψ. The helicity per unit flux H/ψ^2 of the magnetic tube can be divided into two components [34, 156] called the Writhe helicity $\mathcal{W}$ and the twist helicity $\mathcal{T}$.

Motions which do not break the curves conserve $\mathcal{L}$, just as ideal motions conserve magnetic helicity H. The relation $H/\psi^2 = \mathcal{T} + \mathcal{W}$ is analogous to the relation $\mathcal{L} = \mathcal{T} + \mathcal{W}$ known to hold for the edges of a ribbon [59, 180, 246]. The twist $\mathcal{T}$ measures how much a secondary curve (for example one edge of a ribbon) twists about the first (the central axis of the ribbon). Let s denote arc length along a curve, $\mathbf{T}(s)$ denote the tangent vector, and $\hat{\mathbf{V}}(s)$ denote a unit vector pointing to the secondary curve. Then

$$\mathcal{T} = \frac{1}{2\pi} \oint \mathbf{T} \cdot \hat{\mathbf{V}} \times \frac{\mathrm{d}\hat{\mathbf{V}}}{\mathrm{ds}} \, \mathrm{ds}. \tag{3.1}$$

For magnetic fields, this twist number measures field aligned current. In particular, if $J_\parallel$ is the current parallel to the magnetic field, and μ_0 is the vacuum permeability, then

$$\frac{\mathrm{d}\mathcal{T}}{\mathrm{d}s} = \frac{\mu_0 J_\parallel}{4\pi |\mathbf{B}|}. \tag{3.2}$$

The writhe number $\mathcal{W}$ is defined by the integral

$$\mathcal{W} = \frac{1}{4\pi} \oint \oint \frac{\mathbf{x}(s) - \mathbf{x}(s')}{|\mathbf{x}(s) - \mathbf{x}(s')|^3} \cdot \frac{\mathrm{d}\mathbf{x}(s)}{\mathrm{d}s} \times \frac{\mathrm{d}\mathbf{x}(s')}{\mathrm{d}s'} \, \mathrm{d}s \, \mathrm{d}s'. \tag{3.3}$$

Note that $\mathcal{T}$ is defined by a single integral and therefore has a well defined local density. In contrast, $\mathcal{W}$ is defined by a double integral and thus has no local density; it depends on the global geometry of the curve and can not be calculated by adding contributions from individual short sections of the curve. However, simpler and more efficient methods have been found for actually calculating $\mathcal{W}$ as described in [35].

Because of the conservation of helicity, a reduction in twist will result in an increase in $\mathcal{W}$. Therefore, a change in writhe will have the opposite sign as the change

in $\mathcal{T}$. Using the measurement of writhe, we determine the internal twist by

$$\mathcal{T} = \frac{H}{\psi^2} - \mathcal{W}. \tag{3.4}$$

The opportunity to change twist into writhe and decrease the energy may result in writhing instabilities where the axis forms helical structures [137, 228, 229, 230, 235].

3.2.2 Energy and Helicity Spectra

Following the definition of the Fourier transform of a random function in Appendix B, the Fourier transforms of the magnetic field and vector potential are (using $\mathbf{B} = \nabla \times \mathbf{A}$)

$$\widetilde{\mathbf{B}}_{\mathrm{k}} = \frac{1}{(2\pi)^3} \int \mathbf{B}(\mathbf{x}) \mathrm{e}^{-i\mathbf{k}\cdot\mathbf{r}} \mathrm{d}^3x = -\mathrm{i}\mathbf{k} \times \widetilde{\mathbf{A}}_{\mathrm{k}}. \tag{3.5}$$

With this convention, the magnetic energy spectrum is

$$M_{\mathrm{k}} = \frac{1}{2} \int_{\mathrm{k-shell}} \widetilde{\mathbf{B}}^*_{\mathrm{k}} \cdot \widetilde{\mathbf{B}}_{\mathrm{k}} \, \mathrm{k}^2 \mathrm{d}\Omega_{\mathrm{k}}, \tag{3.6}$$

and the helicity spectrum is

$$H_{\mathrm{k}} = \frac{1}{2} \int_{\mathrm{k-shell}} (\widetilde{\mathbf{A}}^*_{\mathrm{k}} \cdot \widetilde{\mathbf{B}}_{\mathrm{k}} + \widetilde{\mathbf{A}}_{\mathrm{k}} \cdot \widetilde{\mathbf{B}}^*_{\mathrm{k}}) \mathrm{k}^2 \mathrm{d}\Omega_{\mathrm{k}}, \tag{3.7}$$

where $\mathrm{d}\Omega_k$ is the solid angle element in Fourier space [154].

The helicity and energy spectra are normalized such that

$$\int_0^\infty H_{\mathrm{k}} \mathrm{dk} = \langle \mathbf{A} \cdot \mathbf{B} \rangle \, V \equiv H, \tag{3.8}$$

$$\int_0^\infty M_{\mathrm{k}} \mathrm{dk} = \left\langle \frac{1}{2} \mathbf{B}^2 \right\rangle V \equiv M, \tag{3.9}$$

where H and M are magnetic helicity and magnetic energy, respectively, V is the volume element and the angular brackets denote volume averages.

We can easily show that H_{k} is gauge invariant: if $\mathbf{A} \to \mathbf{A} + \nabla\phi$, then $\widetilde{\mathbf{A}}_{\mathrm{k}} \to \widetilde{\mathbf{A}}_{\mathrm{k}} + \mathrm{i}\tilde{\phi}_{\mathrm{k}}\mathbf{k}$. But as $\nabla \cdot \mathbf{B} = 0$, we have $\mathrm{i}\tilde{\phi}_{\mathrm{k}}\mathbf{k} \cdot \widetilde{\mathbf{B}}_{\mathrm{k}} = 0$. Thus equation (3.7) is unchanged by the gauge transformation.

We can decompose the Fourier transformed magnetic vector potential $\widetilde{\mathbf{A}}_{\mathrm{k}}$, into a longitudinal component, $\mathbf{h}^{\parallel}$, and eigenfunctions $\mathbf{h}^{\pm}$ of the curl operator

$$\widetilde{\mathbf{A}}_{\mathrm{k}} = a_{\mathrm{k}}^{+}\mathbf{h}_{\mathrm{k}}{}^{+} + a_{\mathrm{k}}^{-}\mathbf{h}_{\mathrm{k}}{}^{-} + a_{\mathrm{k}}^{\parallel}\mathbf{h}_{\mathrm{k}}{}^{\parallel}, \tag{3.10}$$

with

$$\mathrm{i}\mathbf{k} \times \mathbf{h}_{\mathrm{k}}{}^{\pm} = \pm \mathrm{k}\mathbf{h}_{\mathrm{k}}{}^{\pm}, \qquad \mathrm{k} = |\mathbf{k}|\,, \tag{3.11}$$

and

$$\left\langle \mathbf{h}_{\mathrm{k}}{}^{+^*} \cdot \mathbf{h}_{\mathrm{k}}{}^{+} \right\rangle = \left\langle \mathbf{h}_{\mathrm{k}}{}^{-^*} \cdot \mathbf{h}_{\mathrm{k}} \right\rangle = \left\langle \mathbf{h}_{\mathrm{k}}{}^{\parallel^*} \cdot \mathbf{h}_{\mathrm{k}}{}^{\parallel} \right\rangle = 1. \tag{3.12}$$

The longitudinal component $a_{\mathrm{k}}^{\parallel}\mathbf{h}_{\mathrm{k}}{}^{\parallel}$ is parallel to k and vanishes after taking the curl to calculate the magnetic field. It can also be set to zero by choosing a Coulomb gauge potential, $\nabla \cdot \mathbf{A} = 0$.

An example is to find $\mathbf{B}$ for $\mathbf{k} = (0, 0, 3l^{-1})$ and $\widetilde{\mathbf{A}}_{\mathrm{k}} = 2.7\mathbf{h}^{+}_{3l^{-1}}$, where l is some length scale. We have $\widetilde{\mathbf{B}}_{\mathrm{k}} = \mathrm{i}\mathbf{k}\times\widetilde{\mathbf{A}}_{\mathrm{k}} = \mathrm{i}\mathbf{k}\times(2.7\mathbf{h}^{+}_{3\mathrm{l}^{-1}})$ and from (3.11) we obtain $\widetilde{\mathbf{B}}_{\mathrm{k}} = (3l^{-1})\,2.7\mathbf{h}^{+}_{3l^{-1}} = 8.1l^{-1}\mathbf{h}^{+}_{3l^{-1}}$. The magnetic field $\mathbf{B}$ has magnitude $8.1l^{-1}$ and is in the x and y directions.

The complex coefficients $a_{\mathrm{k}}^{\pm}(t)$ depend on k and t, and the eigenfunctions $\mathbf{h}_{\mathrm{k}}^{\pm}$, which form an orthonormal set, depend on k [46]. They are given by

$$\mathbf{h}_{\mathrm{k}}^{\pm} = \frac{1}{\sqrt{2}} \frac{\mathbf{k} \times (\mathbf{k} \times \mathbf{e}) \mp \mathrm{ik}(\mathrm{k} \times \mathbf{e})}{\mathrm{k}^2\sqrt{1 - (\mathbf{k} \cdot \mathbf{e})^2/\mathrm{k}^2}}, \tag{3.13}$$

where $\mathbf{e}$ is an arbitrary unit vector that is not parallel to $\mathbf{k}$. Using the above relations, we can then write the magnetic helicity spectrum as

$$H_{\mathrm{k}} = \mathrm{k}(\left|a_{\mathrm{k}}^{+}\right|^2 - \left|a_{\mathrm{k}}^{-}\right|^2)V, \tag{3.14}$$

and the energy spectrum in the form

$$M_{\mathrm{k}} = \frac{1}{2}\mathrm{k}^2(\left|a_{\mathrm{k}}^{+}\right|^2 + \left|a_{\mathrm{k}}^{-}\right|^2)V, \tag{3.15}$$

where V is the volume of integration. From equations (3.14) and (3.15) we obtain the *realizability condition*

$$\frac{1}{2}\mathrm{k}\,|H_{\mathrm{k}}| \leq M_{\mathrm{k}}. \tag{3.16}$$

This condition becomes an equality for the eigenfields $\mathbf{h}_{\mathrm{k}}^{+}$ and $\mathbf{h}_{\mathrm{k}}^{-}$. The realizability condition is tested for a twisted tube in section 3.4.8.

The energy and helicity spectra are closely related to the Fourier transform of the two-point correlation function $R_{ij}(\mathbf{r})$ of the magnetic field [154]. Define

$$R_{ij}(\mathbf{r}) = \int B_i(\mathbf{x}) B_j(\mathbf{x}+\mathbf{r}) \mathrm{d}^3 x. \tag{3.17}$$

Then, in Fourier space, one finds that

$$\widetilde{R}_{ij}(\mathbf{k}) = \frac{1}{(2\pi)^3} \int R_{ij}(\mathbf{r}) \mathrm{e}^{-\mathrm{i}\mathbf{k}\cdot\mathbf{r}} \mathrm{d}^3 r \tag{3.18}$$

$$= \widetilde{\mathbf{B}}_{\mathrm{k}\,i} \widetilde{\mathbf{B}}^*_{\mathrm{k}\,j}. \tag{3.19}$$

We can then integrate over spherical shells in k space as in equations (3.6) and (3.7), with the help of (3.5) to find that:

$$M_{\mathrm{k}} = \frac{1}{2} \int_{\mathrm{k-shell}} \widetilde{R}_{ii}\, \mathrm{k}^2 \mathrm{d}\Omega_{\mathrm{k}}, \tag{3.20}$$

$$H_{\mathrm{k}} = \int_{\mathrm{k-shell}} \frac{-\mathrm{i}\epsilon_{\ell mn} k_\ell \widetilde{R}_{mn}}{k^2} \mathrm{k}^2 \mathrm{d}\Omega_{\mathrm{k}}. \tag{3.21}$$

Thus, the trace of $\widetilde{R}$ gives the energy spectrum, while the helicity spectrum comes from the anti-symmetric (and perpendicular to $\mathbf{k}$) component of $\widetilde{R}$. This relation between spectra and two point correlations is discussed further in section 3.2.4.

3.2.3 The Relation Between Helicity Spectrum and Spatial Structure

The helicity spectrum measures the distribution of twist, shear, and linking on different length scales. It fails, however, in detecting *spatial* fluctuations of helicity. For example, consider the field

$$\mathbf{B} = (\sin 2x \cos 2y, -\cos 2x \sin 2y, \sin x \sin y). \tag{3.22}$$

This field consists of twisted flux tubes aligned along the z direction (figure 3.2). The helicity spectrum for this field is identically zero, i.e. $H_{\mathrm{k}} = 0$ for all $\mathbf{k}$. While the field contains individual helicity-containing tubes of alternating sign, the tubes have the same size. Thus the positive helicity exactly cancels the negative helicity at the same places in the spectrum. A quantity related to helicity which detects spatial distribution in weakly inhomogeneous turbulence has been proposed by Subramanian and Brandenburg [219].

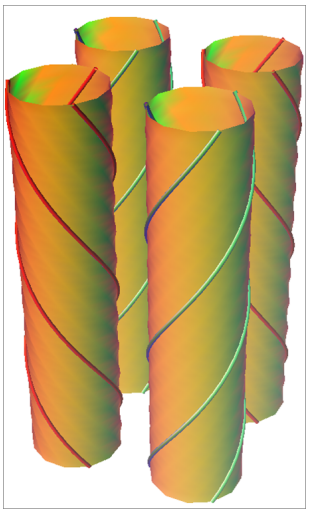

Figure 3.2: A field whose helicity spectrum $H_{\rm k} = 0$ for all $\mathbf{k}$.

Helicity-containing structures are inherently three dimensional. However, we can create a simple field which only varies in one dimension to investigate how a simple crossed field is represented in a Fourier spectrum:

$$\mathbf{B} = \frac{1}{\sqrt{2\pi}\sigma} \mathrm{e}^{-(z-w/2)^2/2\sigma^2}\,\hat{\mathbf{x}} + \mathrm{e}^{-(z+w/2)^2/2\sigma^2}\,\hat{\mathbf{y}}. \tag{3.23}$$

This field consists of two layers of flux separated by a distance w. Each layer has unit flux (per unit length in x and y directions) distributed with Gaussian profiles of width σ; their fields are perpendicular to each other.

Taking the Fourier transform in the z direction of the above magnetic field, we have

$$\widetilde{\mathbf{B}}_{\rm k} = \mathrm{e}^{\mathrm{i}kw/2}\,\mathrm{e}^{-k^2\sigma^2/2}\,\hat{\mathbf{x}} + \mathrm{e}^{-\mathrm{i}kw/2}\,\mathrm{e}^{-k^2\sigma^2/2}\,\hat{\mathbf{y}}, \tag{3.24}$$

which gives a helicity spectrum of the form

$$H_{\rm k} = \frac{2}{\pi k}\,\mathrm{e}^{-k^2\sigma^2}\,\sin(kw), \tag{3.25}$$

(as shown in figure 3.3). Here the envelope has width $\sigma/\sqrt{2}$ and the periodicity is $2\pi/w$. The helicity spectrum broadens as the width σ of the layers decreases; in the limit $\sigma \to 0$ it becomes

$$\mathbf{B} = \delta(z - w/2)\hat{\mathbf{x}} + \delta(z + w/2)\hat{\mathbf{y}}; \tag{3.26}$$

$$H_{\rm k} = \frac{2}{\pi k}\sin(kw). \tag{3.27}$$

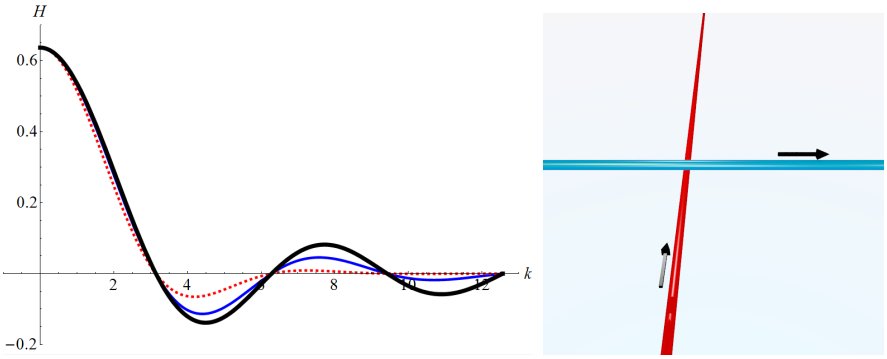

Figure 3.3: Left: the helicity spectrum for two perpendicular thin slabs of magnetic flux. The separation between the slabs has been set at $w = 1$. Curves are given for $\sigma = 0.2$ (dashed), $\sigma = 0.1$ (thin solid), and $\sigma \to 0$ (thick solid). Right: two crossed thin tubes of magnetic flux. The separation between the tubes is w. The helicity spectrum for this configuration is identical to that of the crossed slabs in limit of zero radius (thick solid curve).

3.2.4 Why Does the Helicity Spectrum Oscillate for Localized Flux?

What is the origin of the $\sin(kw)$ factor in the helicity spectrum? We can better understand this effect by recalling the close relation between the helicity spectrum and the Fourier representation of the two-point correlation function $R_{ij}(\mathbf{r})$.

For the two slab field above (3.26), as variations only occur in z, we can write

$$R_{12}(z) \;=\; \int B_1(z_0)B_2(z_0+z)\mathrm{d}z_0 = \delta(z+w). \tag{3.28}$$

Similarly $R_{21}(z) = \delta(z-w)$. Fourier transforms give

$$\widetilde{R}_{12} = \frac{1}{2\pi}\mathrm{e}^{-\mathrm{i}kw}; \qquad \widetilde{R}_{21} = \frac{1}{2\pi}\mathrm{e}^{\mathrm{i}kw}. \tag{3.29}$$

The one dimensional helicity spectrum analogous to (3.21) is

$$H_\mathrm{k} \;=\; \frac{-\mathrm{i}\epsilon_{3mn}k\widetilde{R}_{mn}(k)}{k^2} - \frac{-\mathrm{i}\epsilon_{3mn}k\widetilde{R}_{mn}(-k)}{k^2} \tag{3.30}$$

$$\;=\; \frac{1}{\mathrm{i}k}\Big((\widetilde{R}_{12}(k) - \widetilde{R}_{21}(k)) - (\widetilde{R}_{12}(-k) - \widetilde{R}_{21}(-k))\Big) \tag{3.31}$$

$$\;=\; \frac{2}{\pi k}\frac{1}{2\mathrm{i}}\left(\mathrm{e}^{\mathrm{i}kw} - \mathrm{e}^{-\mathrm{i}kw}\right) = \frac{2}{\pi k}\sin(kw), \tag{3.32}$$

in accordance with our previous calculation.

We can do a similar calculation for two crossed tubes (as shown on the right of figure 3.3). Consider two thin unit flux tubes aligned along the x axis at $z = w/2$, and along the y axis at $z = -w/2$. Then one finds $R_{12}(z) = \delta(z + w)$ and $R_{21}(z) = \delta(z - w)$ as above (multiplied by flux squared). This leads to the same spectrum for $H_{\rm k}$.

Note that the above fields have net fluxes in the x and y directions. Despite the infinite domain, the helicity is finite. A more physically reasonable field with zero net flux has two oppositely directed tubes in the x direction intertwined with two in the y direction:

$$\mathbf{B} = \delta(z - 3w/2)\hat{\mathbf{x}} + \delta(z - w/2)\hat{\mathbf{y}} - \delta(z + w/2)\hat{\mathbf{x}} - \delta(z + 3w/2)\hat{\mathbf{y}}. \tag{3.33}$$

This field still has an oscillatory spectrum, albeit with two modes of oscillation:

$$H_{\rm k} = \frac{6}{\pi k}\sin(kw) - \frac{2}{\pi k}\sin(3kw). \tag{3.34}$$

3.3 The Magnetic Field Inside a Twisted Torus

We consider a magnetic flux tube in a shape of a torus, with minor radius a and major radius R. The circular axis of the torus lies in a horizontal plane encircling the z-axis. In cylindrical coordinates a point is given by (ρ, ϕ, z). We will also need toroidal coordinates (r, θ, ϕ): here r denotes the distance of a point from the circular axis of the torus, and θ denotes angle the short way around (with $\theta = 0$ closest to the z-axis). Thus

$$\rho = R - r\cos\theta.$$

The field line equations are

$$\frac{\mathrm{d}r}{B_r} = \frac{r\,\mathrm{d}\theta}{B_\theta} = \frac{\rho\,\mathrm{d}\phi}{B_\phi}, \tag{3.35}$$

and so,

$$B_\theta = \frac{r\,\mathrm{d}\theta}{\rho\,\mathrm{d}\phi}\,B_\phi = \frac{r}{R - r\cos\theta}\frac{\mathrm{d}\theta}{\mathrm{d}\phi}B_\phi. \tag{3.36}$$

If we replace ϕ by arc length s along the toroidal axis, this becomes

$$B_\theta = \frac{rR}{R - r\cos\theta}\frac{\mathrm{d}\theta}{\mathrm{d}s}B_s, \tag{3.37}$$

where B_s is the axial magnetic field and constant and the field line derivative $\mathrm{d}\theta/\mathrm{d}s$ gives the rate of increase of twist $\mathcal{T}$ with arc length s, i.e.

$$\frac{\mathrm{d}\theta}{\mathrm{d}s} = 2\pi\frac{\mathrm{d}\mathcal{T}}{\mathrm{d}s} \qquad \text{(torus)}. \tag{3.38}$$

Substituting (3.38) in (3.37) and putting $s = 2\pi R$ leads to B_θ for a torus

$$B_\theta = \frac{r\mathcal{T}}{R}\left(\frac{R}{R - r\cos\theta}\right) B_s. \tag{3.39}$$

And for a thin torus with $R \gg r$, the above equation becomes

$$B_\theta = \frac{r\mathcal{T}}{R} B_s. \tag{3.40}$$

Next consider a thin flux tube of (almost) arbitrary shape. Locally, we can replace major radius R in the above analysis by the curvature radius $R(s)$ of the central axis of the tube. We also lose the angle ϕ, replacing it by the arc length s along the axis. The angle $\theta = 0$ now points in the direction of the curvature vector. But, in addition, there will be an extra source of twist due to the torsion τ of the axis [156]:

$$\frac{\mathrm{d}\theta}{\mathrm{d}s} = 2\pi\left(\frac{\mathrm{d}\mathcal{T}}{\mathrm{d}s} - \tau\right). \tag{3.41}$$

We assume twist (and thus parallel current) to be uniformly distributed along the total arc length L of the tube. In this case

$$\frac{\mathrm{d}\mathcal{T}}{\mathrm{d}s} = \frac{H - \mathcal{W}}{L}, \tag{3.42}$$

and so

$$B_\theta = \frac{2\pi r R(s)}{R(s) - r\cos\theta}\left(\frac{H - \mathcal{W}}{L} - \tau\right) B_s. \tag{3.43}$$

We keep B_s uniform inside the tube. In order to find the upper limit for a, in the equation (3.43), the denominator $R - r\cos\theta$ should be more than zero. Hence, $R > r\cos\theta$ and for $\theta = 0$, we should have $R > r$. Also, since we have $0 \leq r \leq a$, the radius of curvature $R(s)$ should always be larger than the minor radius a.

3.3.1 The Magnetic Energy of a Thin Torus

We define the magnetic energy E_T of the torus by

$$E_T = \frac{1}{2\mu_0}\int \mathbf{B}^2 \mathrm{d}^3x, \tag{3.44}$$

where μ_0 is the magnetic permeability. We have $B_\phi = B_s$, $B_r = 0$ and

$$B_\theta = \frac{2\pi r\mathcal{T}}{L} B_s. \tag{3.45}$$

Substituting for B_θ, B_ϕ and B_r in the energy integration (3.44) leads to

$$E_T = \frac{1}{2\mu_0}\int_0^{2\pi}\int_0^{2\pi}\int_0^{a} (B_\theta^2 + B_\phi^2 + B_r^2)\, r\,\mathrm{d}r\,\mathrm{d}\phi\,\rho\,\mathrm{d}\theta, \tag{3.46}$$

where $\rho = \sqrt{R^2 + r^2 + 2rR\cos\theta}$. Performing the angular integration and letting $q = r/R$, we obtain

$$E_T = \frac{2\pi B_s^2 R^3}{\mu_0} \int_0^{1/p} \left(1 + (\mathcal{T}q)^2\right) q \left[\sqrt{(1-q)^2}\mathrm{E}\left(\frac{-4q}{(1-q)^2}\right) + \sqrt{(1+q)^2}\mathrm{E}\left(\frac{4q}{(1+q)^2}\right)\right] \mathrm{d}q, \tag{3.47}$$

where E is the complete elliptic integral of the second kind and $p = R/a$ is the torus aspect ratio. We calculate this energy integral numerically in section 3.4 for given aspect ratio p, major radius R and an internal twist $\mathcal{T}$.

3.3.2 The Energy Calculation for a Thin Tube

When the tube is very thin, its topology becomes equivalent to the topology of a cylinder. Here the length of a cylinder is L and its volume is

$$V = L(\pi a^2),$$

where a is the radius. The total energy is comprised of two parts

$$E = E_{\text{axial}} + E_{\text{twist}}.$$

The axial energy component is

$$E_{\text{axial}} = \frac{1}{2\mu_0} \int B_{\text{axial}}^2 \, \mathrm{d}^3x = \frac{1}{2\mu_0} \int B_s^2 \, \mathrm{d}^3x. \tag{3.48}$$

Substituting for volume element leads to

$$E_{\text{axial}} = \frac{\pi a^2 \, L}{2\mu_0} \, B_s^2. \tag{3.49}$$

The twist energy component is

$$E_{\text{twist}} = \frac{1}{2\mu_0} \int B_\theta^2 \, \mathrm{d}^3x. \tag{3.50}$$

From (3.43) and when $R \gg r$, we have

$$B_\theta = 2\pi r \left(\frac{H - \mathcal{W}}{L} - \tau\right) B_s. \tag{3.51}$$

Considering $A = 2\pi\left(\frac{H-\mathcal{W}}{L} - \tau\right)$, we write

$$B_\theta = A \, B_s \, r, \tag{3.52}$$

where A is a constant. Substituting for B_θ in (3.50), we obtain

$$\begin{aligned} E_{\text{twist}} &= \frac{1}{2\mu_0} \int (A \, B_s \, r)^2 \mathrm{d}^3x \\ &= \frac{1}{2\mu_0} \int_0^a A^2 B_s^2 r^2 2\pi r L \mathrm{d}r \\ &= \frac{\pi A^2 a^4 L}{4\mu_0} \, B_s^2. \end{aligned} \tag{3.53}$$

Therefore, the total energy for the thin torus is

$$\begin{aligned} E &= E_{\text{axial}} + E_{\text{twist}} \\ &= \frac{\pi a^2 L}{2\mu_0} B_s^2 + \frac{\pi A^2 a^4 L}{4\mu_0} B_s^2 \\ &= \frac{\pi a^2 L}{2\mu_0}(1 + \frac{A^2 a^2}{2}) B_s^2. \end{aligned} \tag{3.54}$$

By substituting for B_s in terms of flux $B_s = \psi/(\pi a^2)$ in the above equation, we find

$$E = \frac{\psi^2 L}{2\mu_0 \pi a^2} \left(1 + \frac{A^2 a^2}{2}\right). \tag{3.55}$$

3.3.3 Magnetic Helicity for the Thin Flux Tube

We consider a thin toroidal flux tube with well defined nested flux surfaces. We define the flux function ψ with $\psi = 0$ on the magnetic axis, and let $\chi(\psi)$ be the toroidal flux contained within the flux surface ψ. In the infinitesimal flux layer $[\psi, \psi + \delta\psi]$, there is a surface where the field lines go the long way round about the major radius R and the short way round about the minor radius a before closing back on themselves. If we consider the layer to consist of a single tube of axial flux $\delta\chi/R$, then we can write the helicity of the thin tube as

$$\delta H = 2\psi \, \delta\psi \, \mathcal{T}. \tag{3.56}$$

Note that δH depends on $\mathcal{T}$. The equation (3.56) then integrates to give

$$H = \mathcal{T} \, \psi^2. \tag{3.57}$$

3.4 Numerical Simulations

In this section, we consider the behaviour of helicity in the STF picture. Our aim is to understand how helicity is distributed over different scales, and how that distribution relates to the twist-writhe decomposition. We start with a magnetic flux tube of circular cross section and unit flux. The radius a of this tube is held constant. At first, we consider a circular axis shape, then subject the shape to stretch, twist, and fold operations. The writhe is calculated employing the methods described in [35]. Using this measurement of writhe, we determine the internal twist from equation (3.4).

In order to calculate the helicity and energy spectra, the tube is placed inside a three-dimensional cubic grid (we employ 128^3). The central axis of the tube is represented by n points ($n = 300$ seems sufficient). At each point on the grid the code first determines whether it is within a distance a of the axis curve; if so then the magnetic field is determined. A fast Fourier transform then leads to a determination of the spectra.

We employ a uniform radius $a = 1.6$ in our study (the grid spacing is one). Larger radii make it more difficult to separate large and small-scales in the spectra. Smaller radii are more subject to edge effects (i.e. the boundary of the flux tube is not properly resolved, resulting in significant changes to the spectra).

Helicity is measured in units of ψ^2 (equivalently, we can set the flux to be $\psi = 1$ and let $B_s = 1/(\pi a^2)$). Energy is measured in units of ψ^2/a. In the graphs, wave-number k is measured in units of $k_0 = 2\pi/N$, where N is the size of the grid (we use $N = 128$). Thus a wavelength of λ corresponds to a wave-number of $k = k_0^{-1}(2\pi/\lambda) = N/\lambda$.

There is a valid concern that helicity is not always well-defined for periodic boxes [32]. However, this problem only presents itself when there is net flux in some direction, whereas the closed tubes here do not have a net flux in any direction.

3.4.1 Circular Tubes

Figure 3.4 shows the helicity and energy spectra for a circular magnetic flux tube with major radius 41.3 (aspect ratio 26). Note that edge effects produce no fluctuations whatsoever to the helicity spectrum, although they do appear in the energy spectrum, particularly for wave-numbers above 50.

The minor radius a provides a significant length scale for the tube, which should affect the spectra. For the tube with internal twist, the azimuthal field reverses over one diameter, i.e. half a wavelength corresponds to $2a$. Thus we infer a characteristic wavelength $\lambda_a = 4a$ and a corresponding wave-number $k_a = N/4a$. For our chosen parameters $k_a = 20$, which corresponds well to the peak of the helicity spectrum for the tube with internal twist (figure 3.4(c)). Also, the energy spectrum for the $\mathcal{T} = 0$ tube has a peak slightly below 20. This peak moves to the right for $\mathcal{T} = 1$.

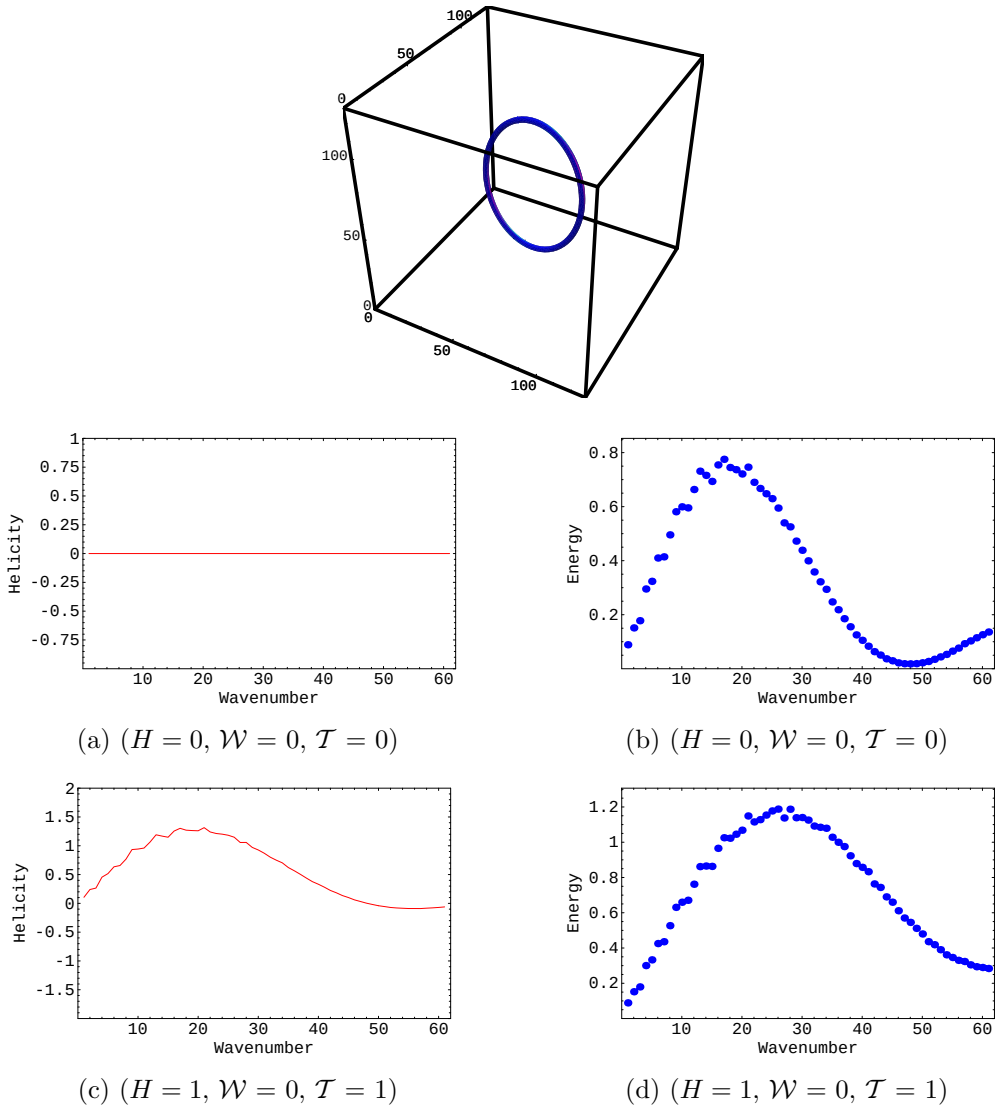

(a) ($H = 0, \mathcal{W} = 0, \mathcal{T} = 0$)

(b) ($H = 0, \mathcal{W} = 0, \mathcal{T} = 0$)

(c) ($H = 1, \mathcal{W} = 0, \mathcal{T} = 1$)

(d) ($H = 1, \mathcal{W} = 0, \mathcal{T} = 1$)

Figure 3.4: Spectra of a circular tube of radius $a = 1.6$ placed in a 128^3 grid. The tube has aspect ratio = 26. (a) and (b): $H = \mathcal{W} = \mathcal{T} = 0$. The magnetic helicity spectrum (a) shows that the helicity remains zero for large and small-scales (small and large wave-numbers) despite any edge effects. The energy spectrum (b) shows a maximum at the wave-number $k = 17$ and a minimum at the wave-number $k = 48$. Edge effects prevent the energy in small-scales from reaching a zero value. (c) After increasing the internal twist of the circular tube to one, we see an initial increase in the helicity spectrum and a corresponding increase in the energy spectrum (d) of the circular tube.

3.4.2 Stretched Tubes

First we stretch the flux tube, where the semi-major axis is twice the size of the semi-minor axis (figure 3.5), the helicity, writhe, and twist remain zero. Then we increase the helicity to $H = 1$. The writhe remains zero $\mathcal{W} = 0$. The helicity spectrum shows an increase for large-scales and remains zero at small-scales (figure 3.5(c)).

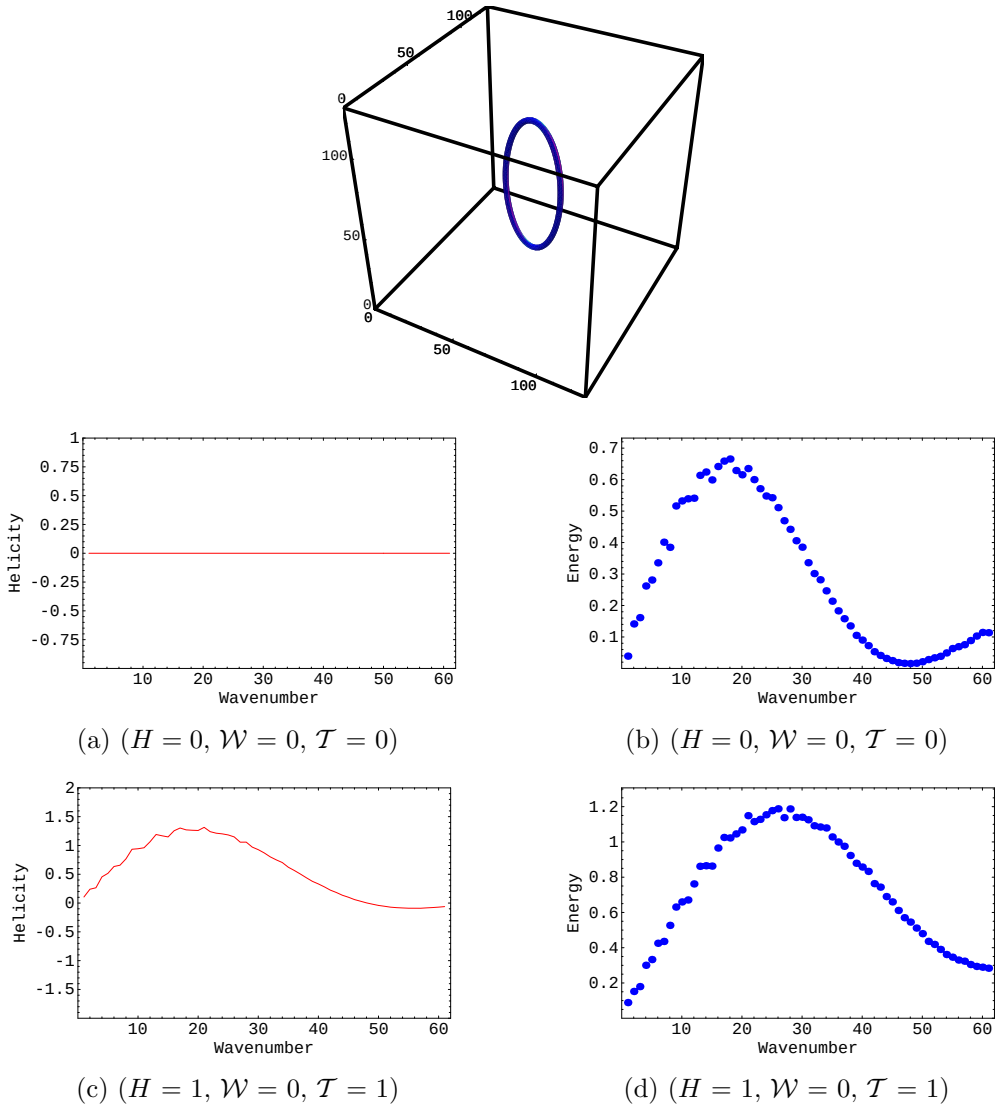

(a) ($H = 0$, $\mathcal{W} = 0$, $\mathcal{T} = 0$)

(b) ($H = 0$, $\mathcal{W} = 0$, $\mathcal{T} = 0$)

(c) ($H = 1$, $\mathcal{W} = 0$, $\mathcal{T} = 1$)

(d) ($H = 1$, $\mathcal{W} = 0$, $\mathcal{T} = 1$)

Figure 3.5: The flux tube is stretched. The total helicity is $H = 0$, $\mathcal{W} = 0$ and $\mathcal{T} = 0$. The helicity spectrum (a) and energy spectrum (b) are similar to the circular flux tube and they remain unchanged. We increase the helicity to $H = 1$, $\mathcal{W} = 0$ and $\mathcal{T} = 1$. The helicity spectrum (c) shows an increase for large-scales and drops to zero for small-scales. (d) There is an increase in the energy values compared to when $H = 0$.

3.4.3 Twisted Tubes

Next we twist the flux tube, keeping the helicity zero. To easily see the effects on the spectra, we have twisted the tube axis by a considerable amount: 3π (figure 3.6). The measurement of writhe shows $\mathcal{W} = 1.152$. With the stretched and twisted tube, some new large length-scales become apparent. For example, the spacing between two points on opposite sides of the tube gives a scale $\lambda_1 \approx 25.1$.

Here, the helicity spectrum shows strong oscillations. The oscillation period is 5.36, corresponding to a length-scale of $128/5.36 = 23.9$. This is very close to the typical separation between neighbouring sections of the tube ($\lambda_1 \approx 25$). Here we see an effect similar to that discussed in section 3.2.4: the two-point correlation function for the magnetic field of a thin tube will have sharp peaks at typical separation lengths. The helicity spectrum oscillates with a wavelength determined by these separation lengths.

We can separate the writhe and twist contributions to the helicity spectrum as follows: first, obtain the spectrum $H_{\rm k}(H = 0)$ for a tube with zero net helicity. This includes equal and opposite twist and writhe contributions. Next obtain $H_{\rm k}(\mathcal{T} = 0)$, the spectrum for a tube with the same shape but zero internal twist (thus zero internal electrical current). We will call this latter spectrum the *writhe helicity spectrum*. Finally, the *twist helicity spectrum* will be defined as the difference between the two, $H_{\rm k}(H = 0) - H_{\rm k}(\mathcal{T} = 0)$. The final two figures in figure 3.6 show these two spectra. Figure 3.6(c) shows that writhe helicity takes both positive and negative values at large-scales and at small-scales it reaches zero. Thus while it is concentrated at large-scales, as expected, it also displays large oscillations.

Table 3.1: Mean wave-numbers for the twisted tube of figure 3.6. The mean wave-numbers are calculated in four different ways, employing weightings for energy, helicity, twist, and writhe.

	$\bar{k}(M)$ ($\bar{\lambda}(M)$)	$\bar{k}(H)$ ($\bar{\lambda}(H)$)	$\bar{k}(H_+)$ ($\bar{\lambda}(H_+)$)	$\bar{k}(H_-)$ ($\bar{\lambda}(H_-)$)
$\mathcal{T} = -\mathcal{W}$ (H = 0)	21.7(5.90)	9.20(13.1)	6.37(20.0)	12.0(10.6)
H = $\mathcal{W}$ ($\mathcal{T} = 0$)	21.7(5.90)	8.50(15.0)	7.57(16.1)	9.77(13.1)
(H = 0) - ($\mathcal{T} = 0$) ($\mathcal{T}$ only)	21.7(5.89)	22.0(5.81)	56.4(2.27)	21.5(5.95)

Table 3.1 provides the mean wave-numbers for the twisted tube. Using these values, we find the wave length $\bar{\lambda}_k = 128/\bar{k}$, where $\bar{k}$ is the mean wave-number given some weighting. For instance if we weight by energy,

$$\bar{k}(M) = \frac{\sum k M_{\rm k}}{\sum M_{\rm k}}, \tag{3.58}$$

while if we weight by helicity (actually $|H_{\rm k}|$)

$$\bar{k}(H) = \frac{\sum k\,|H_{\rm k}|}{\sum |H_{\rm k}|}. \tag{3.59}$$

We then compare the values of $\bar{\lambda}_k$ with $\lambda_a = 4a = 4 \times 1.6 = 6.4$. We look at three cases: zero helicity, writhe helicity, and twist helicity. When using energy as the weighting factor for all three, $\bar{\lambda}_k(M)$ is very close to λ_a. In the second column, with helicity $|H_{\rm k}|$ as the weighting factor, there is a clear separation between the twist helicity (at a length scale near λ_a) and the writhe helicity (at two-and-half times larger scale). We can try to sharpen this separation by weighting with only the positive values of the helicity spectrum(H_+) or negative values (H_-). Here the positive writhe goes to slightly larger scales (slightly smaller $\bar{k}$). The negative writhe comes slightly closer to λ_a. The positive part of the twist helicity is at very large wave-numbers, suggesting perhaps some slight edge effects or numerical noise.

3.4.4 Folded Tubes

We now fold the tube (figure 3.7) with writhe $\mathcal{W} = 1.118$. Qualitatively the spectra are similar to the twisted tube spectra. Here the oscillations in the helicity spectrum have a smaller frequency of about 3.6, corresponding to a length-scale of 36. Taken as a whole, the folded tube has a size of about $36 \times 55 \times 33$.

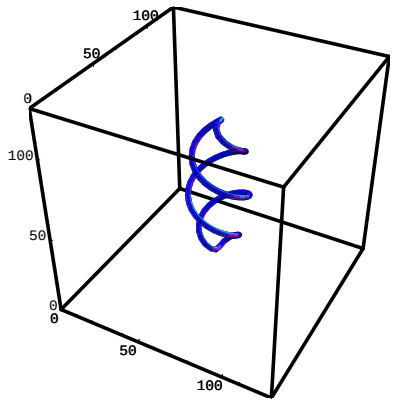

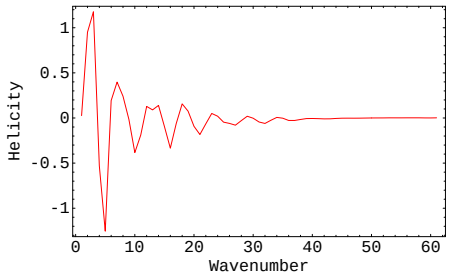

(a) ($H = 0$, $\mathcal{W} = 1.152$, $\mathcal{T} = -1.152$)

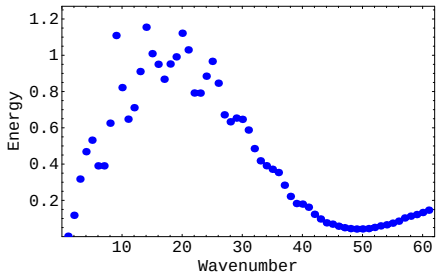

(b) ($H = 0$, $\mathcal{W} = 1.152$, $\mathcal{T} = -1.152$)

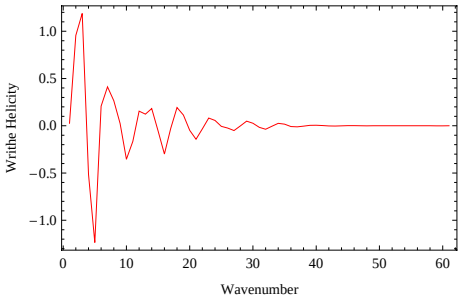

(c) Writhe helicity spectrum

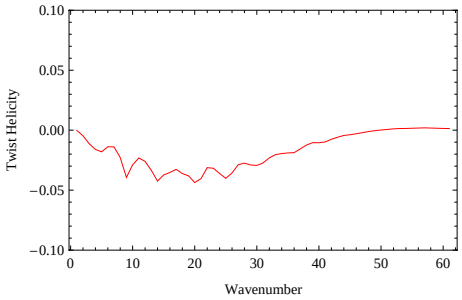

(d) Twist helicity spectrum

Figure 3.6: Spectra of a tube turned through an angle of 3π ($\mathcal{W} = 1.152$). (a) Gives the helicity spectrum for the tube with total helicity $H = 0$. Between the wavenumbers $k = 1$ to $k = 4$ (indicator of large-scale) the helicity is positive. Then there is a sharp decrease and change of sign in the values of helicity, and from then on the helicity oscillates between negative and positive values. From Fourier analysis the oscillation frequency is 5.36. (b) Shows the energy distribution of the twisted flux tube. (c) The writhe helicity spectrum. (d) The twist helicity spectrum. Note that the range on the y-axis of graph (d) is much smaller than that of graph (c).

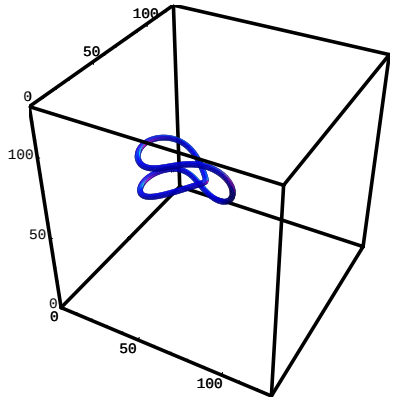

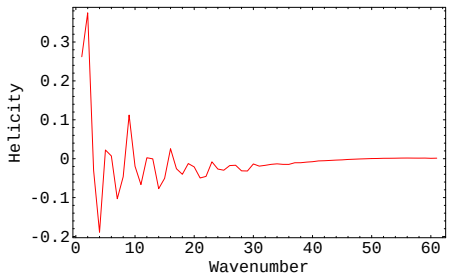

(a) ($H = 0$, $\mathcal{W} = 1.118$, $\mathcal{T}$ = -1.118)

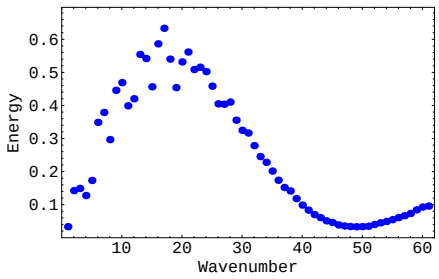

(b) ($H = 0$, $\mathcal{W} = 1.118$, $\mathcal{T}$ = -1.118)

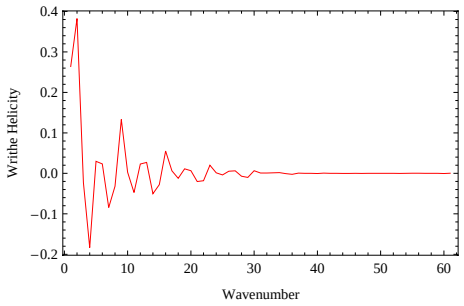

(c) Writhe helicity spectrum

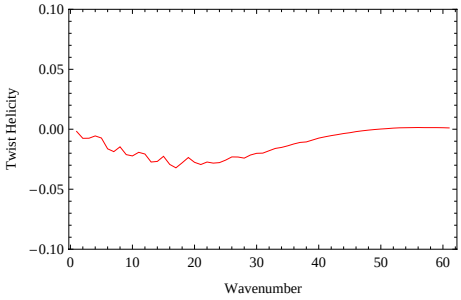

(d) Twist helicity spectrum

Figure 3.7: Spectra for a folded tube. (a) Gives the helicity spectrum. For wave numbers $k = 1$ to $k = 4$ the helicity is positive. Then there is a sharp decrease in the value of helicity and from then on helicity oscillates between negative and positive values, with a frequency of 3.58. (b) Shows the energy distribution of the folded flux tube. (c) The writhe helicity spectrum. (d) The twist helicity spectrum. Note that the range on the y-axis of graph (d) is much smaller than that of graph (c).

3.4.5 The Writhe Spectrum of Compact Curves

Maggioini and Ricca [148] present several families of analytic closed curves, and give a detailed analysis of the behaviour of both intrinsic quantities such as curvature and torsion, and global quantities such as writhe and elastic energy. There is a possible application in biology: many long biological molecules must be strongly coiled in order to fit inside cells. This can require multiple levels of supercoiling. We note that the technique of finding a Fourier spectrum for the writhe as presented here may complement this study. A Fourier analysis shows how the writhe distributes itself on different length scales. As a simple example, figure 3.8 shows two realizations of the hypocycloid curve described by

$$\mathbf{x}(t) = (\cos 2t + \beta \cos 3t, \sin 2t - \beta \sin 3t, \beta \sin t), \tag{3.60}$$

with free parameter β. The usual oscillations still occur with these shapes; it may be that for more irregular shapes the oscillations will smooth out.

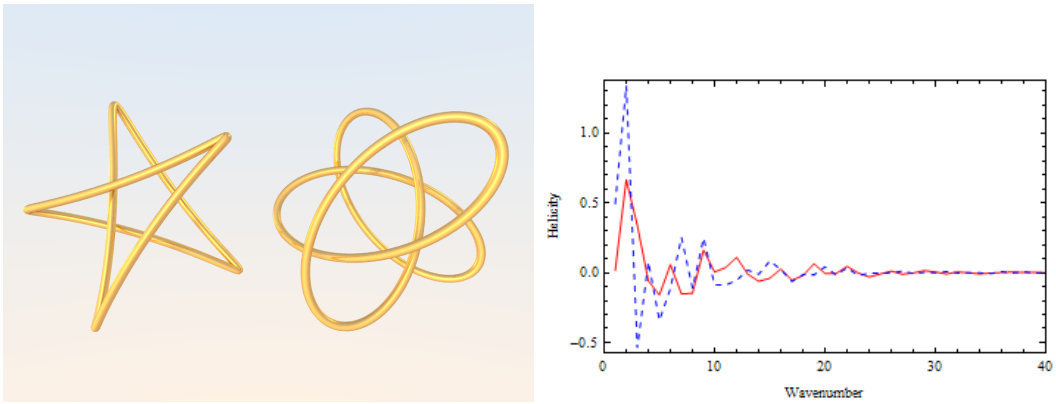

Figure 3.8: Two hypocycloids with their writhe spectra. On the left $\beta = 0.6$ with $\mathcal{W} = 1.1$ (red solid line), while on the right $\beta = 2$ with $\mathcal{W} = 2.0$ (blue dashed line).

3.4.6 Detecting the Twist Bump

Here we compare the twist helicity for a folded, twisted, stretched and circular tube.

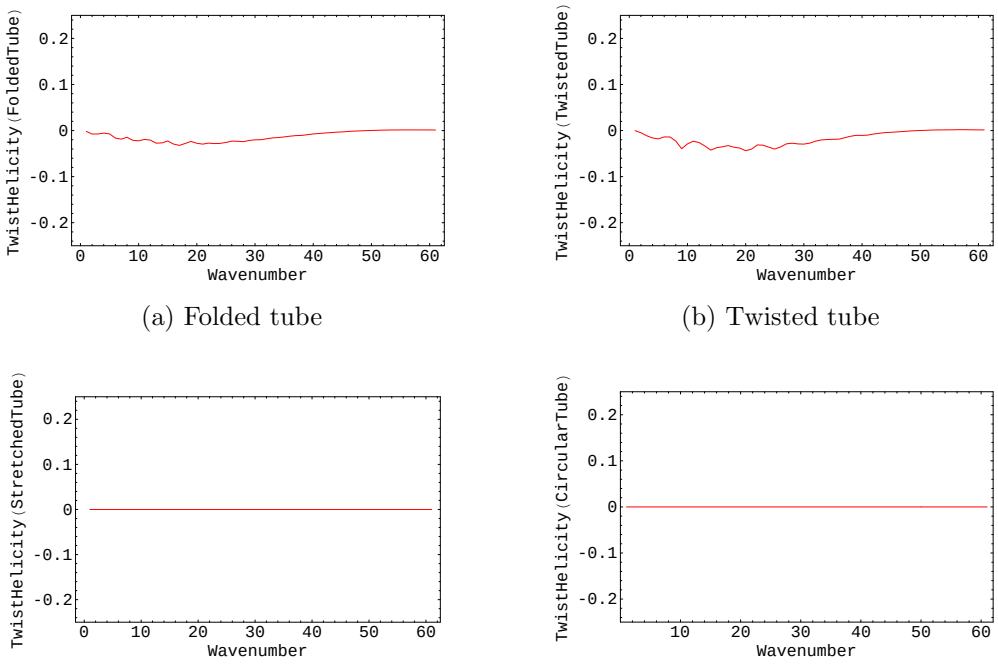

(a) Folded tube

(b) Twisted tube

(c) Stretched tube

(d) Circular tube

Figure 3.9: Twist helicity spectrum for a folded, twisted, stretched and circular tube. The twist helicity for circular and stretched flux tube is zero. The field lines with zero helicity are lying in parallel planes. They cannot wrap around each other, therefore the helicity is zero and as a result the twist helicity is also zero. However, there are oscillations in the helicity spectrum for a twisted and folded tube. The oscillations in the helicity spectrum of a twisted tube is more than that of folded tube.

3.4.7 The Twist Helicity for Grid Sizes of 34^3, 60^3 and 128^3

We compare the twist helicity spectrum of a thin twisted tube (figure 3.6) for grid sizes of 34^3, 60^3 and 128^3 (figure 3.10).

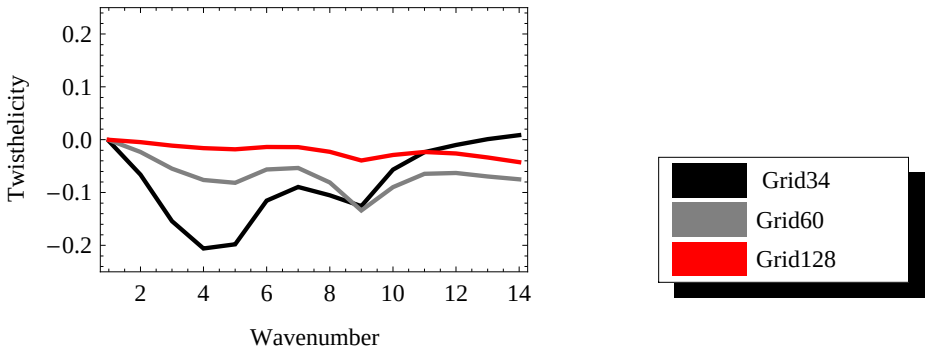

Figure 3.10: The twist helicity spectrum for different grid sizes. When comparing the twist helicity for different grid sizes, the grid size 128^3 provides the most accurate model of the twist helicity spectrum. Also, total helicity and energy for grid size 128^3 is the closest to our analytical results. The total energy from summing of the Fourier series is 85% of the thin flux tube energy estimate.

3.4.8 Testing the Realizability Condition

Following our discussion in section 3.2.2, we test the realizability condition for a twisted tube.

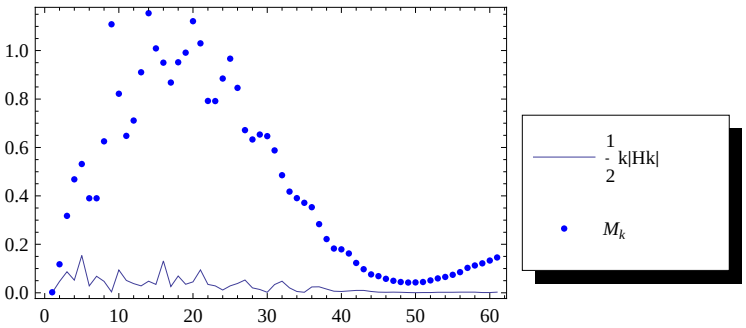

(a) (Testing realizability condition for $H = 0$)

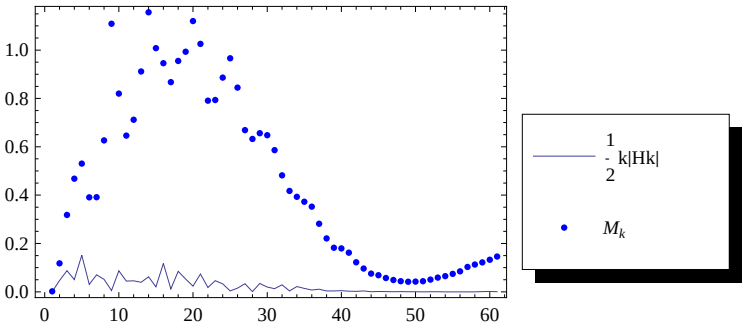

(b) (Testing realizability condition for $H = 1.152$)

Figure 3.11: From (a) and (b) it is clear that the realizability condition $\frac{1}{2}k\,|H_{\rm k}| \leq M_{\rm k}$ is satisfied for a twisted tube for the cases of $H = 0$ and $H = 1.152$. Note that at very low wave-numbers the fields are helical as $\frac{M_{\rm k}}{1/2k|H_{\rm k}|}$ is not far from 1. However, as the wave-number increases to 20 and more, $\frac{M_{\rm k}}{1/2k|H_{\rm k}|} \gg 1$, the helical contribution is small and therefore the realizability condition is easily satisfied.

3.5 Conclusions

This chapter has analysed the influence of twist and writhe numbers on helicity and energy spectra in the STF dynamo. Calculating the writhe number of a flux tube has two purposes. First, it assists us in finding out how much the internal twist changes as the tube is distorted. This greatly simplifies the modelling of a thin flux tube. Second, the writhe provides a valuable diagnostic for large-scale structure. We have compared this diagnostic with the more usual one: examining power spectra at low wave-numbers. We showed that there is a strong correlation between the helicity distribution over different scales and the twist-writhe decomposition. This correlation shows up in the mean wave-number calculations (table 3.1). As expected [46, 95], twist helicity appears at relatively large wave-numbers, while writhe helicity appears at smaller wave-numbers. The mean wave-number for twist helicity corresponds roughly to a wavelength of four times the radius of the tube. However, the helicity spectrum for writhe helicity is more complicated. While there is net power at low wave-numbers, the spectrum also oscillates within a wide envelope. Although there is a great deal of cancellation between positive and negative helicity, there is no clear boundary between negative helicity at large-scales and positive helicity at small-scales.

Of course, an ensemble of flux tubes of many sizes will all have their own oscillating spectra, somewhat out of phase with each other. Thus, in such an ensemble the oscillations might cancel, leaving only the envelope. Similarly, irregular curves may have oscillations with a broad range of frequencies, again resulting in a smoothing out of the writhe spectrum. However the large gap between mean wave-numbers for twist and writhe helicity should persist.

Chapter 4

Solar Corona

4.1 Introduction

The solar corona has a temperature of more than 10^6 K [67]. In order to maintain this temperature against radiative losses, energy is continuously supplied to the corona. The heating rate of the corona is thought to depend on parameters such as the strength of the coronal field and the length of the magnetic field lines [67]. The solar corona (figure 4.1) is more than 200 times hotter than the chromosphere, its lower boundary, although observational evidence suggests that the hot coronal plasma originates in the chromosphere. The part of the solar corona that is topologically connected to active regions makes up more than 80 percent of the heating energy requirement and most of the energy of the corona is stored in this part [7].

The solar corona is considered to be a very high Reynolds number turbulent plasma, producing intermittent bursts of radiation [12]. Observations of the solar corona show loops of hot plasma emanating from magnetic concentrations at the surface, which trace out the paths of the magnetic flux tubes [169]. The observations demonstrate well defined, discrete entities such as magnetic concentrations and flux tubes. As a result, one can treat the coronal magnetic field as made up of discrete interacting loops [110]. Determining the structure of the coronal magnetic field is of crucial importance in understanding the source of heating, the behaviour of waves propagating through the corona, and the nature of flares. The magnetic structure found in coronal loops has many sources [31].

In the solar corona, the increase of the magnetic energy is thought to be caused by the creation of stresses in the magnetic field lines [240]. Whether fields emerge through the photosphere in an already stressed state or that the stresses are the

result of photospheric foot-point motions of the coronal field is still under debate, as even perhaps both mechanisms are at work [240]. There are theoretical models describing plasma-heating mechanisms that are suitable for operating in the coronal environment [150].

Newly emerging loops can possess twist or other forms of structure and they start with a particular connectivity. The newly emerging flux tubes can be misaligned with the pre-existing ones [106, 210] and they twist or shear due to vorticity below the photosphere [28, 114, 218, 257]. These tubes random walk about each other [129] and this results in braiding of the magnetic field above [30, 173, 237]. If a flux tube obtains twist deep below the photosphere, the twist may propagate along the tube and then into the corona as a torsional Alfvén wave. One way a tube can obtain twist is through reconnection with other tubes; this subject is discussed in chapter 5.

Figure 4.1: Image of a small section of the solar corona made using the transition region and coronal explorer (Trace) satellite.

Solar coronal loops are rooted in a dense and turbulent plasma below the photosphere. Coronal loops are the fundamental building blocks of the corona since thermal conduction transports energy efficiently along the field lines, and not across them. The purpose of a coronal-heating model is to identify the mechanisms responsible for the energy input at coronal heights. Models of coronal heating can be divided into two main categories: stressing models and wave models [150]. These models are sometimes referred to as direct current (DC) and alternating current (AC) models respectively. They differ in the type of question they address such as how the free magnetic energy or wave energy is dissipated or what is the origin of

the magnetic energy [150].

In stressing models, the energy is extracted from coronal magnetic fields that are stressed by slow foot-point motions. Photospheric and subphotospheric motions displace magnetic foot-points in both random and systematic ways which include translational and rotational components [150]. The magnetic energy pumped into the field is then either released in real time or it is stored in the field to be released later. As a result, the plasma heating can be steady, quasi-steady, or highly episodic, depending on the model [150]. The quasi-steady heating refers to situations where the time interval between heating events is short compared to the cooling time by radiation and thermal conduction. Examples of stressing models are:
1. Stochastic build up [28, 218]: considers the random twisting of individual flux tubes that produces a stochastic build up of energy.
2. Critical angle : when the random walk step-size is not short compared to the correlation length, the field becomes entangled and braided, and the energy builds quadratically with time in a monotonic fashion. This model assumes that heating occurs when a critical angle θ is reached between adjacent misaligned flux tubes [30, 174].
3. Critical twist: the energy release occurs when a flux tube reaches a critical twist angle, ϕ, due to the onset of a kink instability [94].
4. Reconnection: the magnetic reconnection is assumed to occur at tangential discontinuities (current sheets) that are postulated to form even in simple magnetic configurations when foot-points are displaced by continuous motions [173]. In all these models reconnection releases the magnetic energy. Reconnection can occur at either currents layers or current sheets.
Current layers: currents can become concentrated in layers of small but finite thickness. Energy that is pumped into the field over large-scales gradually cascades to smaller and smaller scales until the scale is small enough for ohmic dissipation to be effective [237].
Current sheets: considers the formation and destruction of current sheets in magnetic configurations. These sheets dissipate by magnetic reconnection, in a sequence of energy release events [2].
Other models include turbulent processes to describe the effect of many reconnection events such as:
1. Taylor relaxation: makes use of Taylor's well-known conjecture [221] where magnetic fields relax via reconnection to the lowest energy state that conserves helicity, the linear force-free state [48, 105, 242].
2. Turbulence: it is a coronal heating model in which the small spatial scales neces-

sary for effective dissipation are produced by turbulence [72, 78].

In wave models, the energy is deposited by waves that are incident from below. In coronal loops, if the time-scale of the motions is shorter than the end-to-end Alfvén travel time, then we can regard these motions as waves [150]. The energy that powers the waves feeds into the coronal magnetic fields. However, in models mentioned here, the waves are generated at the base of the corona by photospheric turbulence and they propagate upward to heat the corona [150]. Examples of wave models are: resonance [108], resonance absorption [99, 166, 194], current layers [93] and turbulence [111].

There are two major problems associated with most of these models. First is that they are either based on non-observable parameters such as currents, non-potential magnetic energies or coronal magnetic fields, or they simply do not fit the observed data. Second is that, in many theoretical models, a coronal loop is approximated by a straight cylindric tube where the magnetic field and the density are homogeneous along the tube [7].

In summary, the stressing models involving the gradual stressing of the slow footpoint motions seem likely to be the correct explanation of coronal heating model as their predictions are in better agreement with observations compared to models that attribute coronal heating to the dissipation of MHD waves [150].

The plan of this chapter is as follows. Section 4.2 reviews loop energetics based on the Sturrock-Uchida model [218], used and analysed by Berger [31], where random twisting generates the magnetic energy. Section 4.3 examines models involving tangled field structures, before, finally in section 4.4, we present a review of energy crossing relations by Berger [30] based on the dissipation of randomly braided flux tubes.

4.2 Dissipation of Magnetic Structure in Coronal Loops

The release of magnetic energy and the dissipation of MHD waves on the surface of the Sun results in an increase of temperature in the coronal loops. The structure of coronal loops plays a major role in both of these processes [31]. If the loops are more tangled, the wave energy dissipates more efficiently and also a tangled field

contains a large amount of magnetic energy which is released in reconnection events. This magnetic energy can be estimated if the equilibrium energy before and after reconnection is known. If the loop is highly tangled, it is very difficult to find the solution to the equilibrium equations of the loop [31]. However, one can place lower bounds on the energy of the equilibrium field, using a measure of the tangling known as the crossing number [30]. This will be discussed in section 4.4.

There are a number of different methods for measuring the magnetic energy of the corona and they are reviewed in the next few sections.

4.2.1 Root Mean Square Twist

The magnetic flux at the photosphere is localized into discrete elements. This section considers the field lines from one photospheric element that form a single coherent coronal tube. In this case the field lines emerging from one foot-point re-enter the photosphere through only one other [31].

Rotational motions at or below the photosphere results in twisting of the coronal flux tubes. Sturrock and Uchida [218] pointed out that the magnetic energy stored in the twisted field could be a source of heating and the heating rate would be independent of the dissipation time-scale. This is in contrast to the heating mechanisms based on braided fields that will be discussed in sections 4.3 and 4.4. The Sturrock-Uchida model has been investigated in detail by Berger [28] and Karpen et. al. [117]. Suppose that the photospheric velocity field $\mathbf{v}$ is random and two dimensional and the radius of the photospheric tube is small compared to the coherence length of $\mathbf{v}$. The radius of a typical flux tube is 150-200 km compared to the granule size of 800 km. The twisting process for larger flux tubes is less efficient since the vorticity is not coherent across the area of the tube. For small flux tubes the twist rate depends on

$$\nabla \mathbf{v} = \begin{pmatrix} \partial_x v_x & \partial_x v_y \\ \partial_y v_x & \partial_y v_y \end{pmatrix} = \frac{1}{2}\left[\omega \begin{pmatrix} 0 & 1 \\ -1 & 0 \end{pmatrix} + (\nabla \cdot \mathbf{v}) \begin{pmatrix} 1 & 0 \\ 0 & 1 \end{pmatrix} + \mathbf{s}\right]$$

where

$$\omega = \partial_x v_y - \partial_y v_x,$$

is the vorticity and $\mathbf{s}$ is the symmetric shear tensor. The term $\nabla \cdot \mathbf{v}$ does not contribute to rotation while $\mathbf{s}$ contributes up to almost half of the vorticity term for a turbulent velocity field.

Based on statistical analysis, one can define the mean square vorticity as $\overline{\omega^2} = 4\overline{v^2}/\lambda^2$, where λ measures the correlation length and $\overline{v^2}$ is the mean square velocity. Assuming $\mathcal{T}$ is the number of turns through 2π taken by a field line about the axis of the coronal tube and and the fact that both senses of rotation are equally likely, the mean twist $\overline{\mathcal{T}}$ is zero. The mean square twist $\overline{\mathcal{T}^2}(t)$, is due to rotations at both ends of a coronal loop and grows linearly with time [218]. Starting at $\overline{\mathcal{T}^2}(t) = 0$ at $t = 0$ and assuming infinite conductivity, one finds that [27]

$$\overline{\mathcal{T}^2}(t) \approx \frac{3\tau_c\,\overline{\omega^2}}{8\pi^2}\,t = \frac{3\tau_c\overline{v^2}}{2\pi^2\lambda^2}\,t, \tag{4.1}$$

where τ_c is the Lagrangian correlation time for the photospheric flow. The mean energy also grows linearly with time, an example of the above equation will be given in section 4.3.1.

To find the energy flux, consider the thin flux tube model of section 3.3 connected to a single photospheric flux element of ψ as in Sturrock and Uchida [218]. It is axisymmetric and uniformly twisted with length L, coronal radius a_c, and field strength B_s and the flux is $\psi = \pi a_c^2 B_s$. In polar coordinates , the magnetic field vector is

$$\mathbf{B} = B_s(\mathbf{z} + 2\pi r\mathcal{T}L^{-1}\theta), \tag{4.2}$$

with rotations at both ends providing a mean energy density

$$w = \frac{1}{\pi a_c^2 L}\frac{1}{8\pi}\int\left(\frac{2\pi r\mathcal{T}B_s}{L}\right)^2 \mathrm{d}^3x = \frac{B_s\,\psi\,\mathcal{T}^2}{4L^2}, \tag{4.3}$$

where the mean energy per unit area is

$$P = \frac{L}{2}\frac{\mathrm{d}w}{\mathrm{d}t} = \frac{3B_s\,\psi\,\overline{v^2}\,\tau_c}{16\pi^2 L\lambda^2}. \tag{4.4}$$

At at the photosphere the magnetic field is squeezed into a small intense flux element with radius a and magnetic field strength B [31].

The analysis stated here is based on passive motion in a simple two dimensional random velocity field. In the next section we look at braided field lines.

4.3 Braided Magnetic Fields

A coronal loop can be modelled using a set of N flux tubes that are braided about each other. The random motions of photospheric foot-points generate this braiding. For one or two braided tubes, the magnetic energy grows linearly with time. As the

number of tubes increases to three or more, the magnetic energy grows quadratically with time [25]. Here, we give a brief review of braided flux ropes by Berger [25] where he introduces a method that characterizes the flux rope structure using braids.

We know the main source of coronal heating is the dissipation of the magnetic energy associated with the random component of the magnetic field lines [173, 218]. In order to measure the magnetic energy, one needs to know how fast the magnetic energy builds up due to random boundary motions.

A loop satisfies a non-linear equilibrium equation such as $\mathbf{J}\times\mathbf{B} = 0$ or $\mathbf{J}\times\mathbf{B} = \nabla p$. For a field with given topology, there is some minimum energy satisfying one of the above equations. Because the three dimensional solutions to these equations possess current sheets or very thin layers [152, 171, 238], the highly structured loops are difficult to model numerically or analytically. However, in order to estimate magnetic energy it is not necessary to have an exact equilibrium solution. A magnetic field that satisfies the same boundary conditions and topological constraints as an equilibrium field will have a higher energy than the equilibrium field. For a field with such characteristics, upper limits can then be placed on the equilibrium magnetic energy. This section describes the structure of these fields using an arbitrary braiding pattern.

Berger models a coronal loop using a straight cylinder of length L and radius R. Inside the cylinder is filled with N flux tubes that are braiding about each other. Near the ends of the cylinder, the magnetic flux is contained in N foot-points with a negligible radius, in order to prohibit the transition of flux tubes. This model is able to approximate the actual solar conditions, where the flux at the photosphere is highly localized [85, 253]. The N tubes are straight and parallel and the foot-points random walk about each other. Due to this motion, the flux tubes become braided in the absence of reconnection. The number of foot-points per unit area is measured by

$$\frac{1}{d^2} = \frac{N}{\pi R^2}, \tag{4.5}$$

where d is the distance between the foot-points. If a foot-point approaches the boundary at radius R, it bounces off elastically, hence keeping the foot-points in the vicinity of radius R. This keeps the distance d constant as well.

By increasing N and R for a given d, the effects of the boundary conditions at R can be reduced. Also, for large values of N and a fixed d, the magnetic energy per unit area is independent of N. If this approximation method is based on a very

good algorithm, then it is unnecessary to do the simulation for large values of N. Below we examine this model for cases where $N \leq 3$.

4.3.1 One Tube Model

Consider the case of $N = 1$, where a single flux tube fills the entire cylinder. The transition regions where the tube narrows to a point at the photosphere is ignored. The field lines twisting about the central axis produce the magnetic free energy. For example, if $\lambda = 800$ km, $\overline{v^2} = 1\text{km}s^{-1}$, and $\tau_c = \lambda/v = 800s$, then using (4.1), we obtain $\overline{\mathcal{T}^2}(t) = t/1.5$. This implies an rms twist of about four turns after 24 hours.

4.3.2 Two Tubes Model

The situation for two tubes ($N = 2$) is similar to $N = 1$. The tubes have internal twist of $\mathcal{T}_1$ and $\mathcal{T}_2$, and they wind about each other through an angle θ_{12}. The angle θ_{12} is known as the *winding number* and has attracted considerable interest in random walk theory [36, 214]. The mean winding number is zero but the mean-square winding number increases linearly with time. Note that coronal loops consisting of two intertwined flux tubes have been discussed by Glencross [96].

Let us assume that magnetic energy dissipates over a time-scale τ_d. For $N = 1$ and $N = 2$, the energy input per unit time (power input) is independent of t, and therefore independent of τ_d. In fact, the power input neither depends on the amount of structure already built up within the cylinder, nor on how much structure has been lost to dissipation. When calculating the heating rate, for simplicity, the extremely difficult details of reconnection in the line-tied corona is ignored. Also, because of the rapid reconnection events taking place in the corona, τ_d may be much shorter than the resistive time.

For flux tube numbers as low as $N = 3$, there are interesting effects due to non-trivial braiding. However higher N must be considered in order to accurately simulate tangled coronal loops.

4.3.3 Three or More Tubes Model

For $N > 2$, the system becomes more complex. In this case the tubes can be tangled about one another. To see this clearly, consider a braid that is chopped into pieces of $X, Y, Z, \ldots$, and look at how these parts interact (figure 4.2). Note that a braid XY consisting of pattern X between $z = 0$ and $z = L/2$, and pattern Y between

$z = L/2$ and $z = L$, is not topologically equivalent to the braid YX with pattern X above pattern Y. Also, every braid X has an inverse X^{-1} ($XX^{-1} = I$ = trivial braid), where if X^{-1} is positioned above X, the whole thing unravels leaving a set of parallel tubes.

Consider the example of two tubes for now. A braid between the two tubes (call the tubes A and B) is described by the internal twists $\mathcal{T}_A$, $\mathcal{T}_B$, and the mutual winding θ_{AB}. For simplification, assume that the twists and the winding are represented by discrete pieces; in units of one turn (we know that $\mathcal{T}_A$, $\mathcal{T}_B$ and θ_{AB} evolve continuously as foot-point motions proceed). Define a right handed twist γ_A of one turn on tube A, with the inverse of γ_A^{-1} (left handed twist) with twists on tube B as γ_B or γ_B^{-1} respectively, and the mutual winding between the tubes A and B as γ_{AB} or γ_{AB}^{-1}. The twists and the windings commute with each other.

A sequence of random motions of the foot-points of the tubes produce a braid that is described by a sequence of γ and γ^{-1} symbols. For instance, the motions might result in something like

$$\gamma_A \gamma_B^{-1} \gamma_A^{-1} \gamma_{AB} \gamma_B^{-1} = \gamma_{AB} \gamma_B^{-2}. \tag{4.6}$$

The internal twist $\mathcal{T}_A$ equals the number of γ_A elements minus the number of γ_A^{-1} elements. Therefore, this braid has $\mathcal{T}_A = 0$, $\mathcal{T}_B = -2$, and $\theta_{AB} = 2\pi$. The numbers $\mathcal{T}_A$, $\mathcal{T}_B$, and θ_{AB} grow like a one-dimensional random walk on the integers where their mean is zero and their mean-square is proportional to the number of steps.

Now consider a braid with three or more tubes. Since some of the braid patterns do not commute with each other, the braid pattern XYX^{-1} cannot be reduced because Y is positioned between X and X^{-1} and there won't be any cancellations, but in general the length of a sequence will grow linearly with the number of patterns.

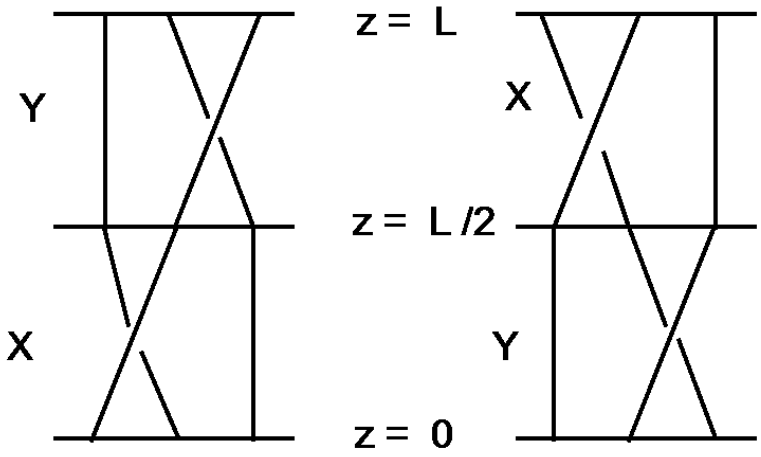

Figure 4.2: The braid XY on the left is not equivalent to YX on the right. Thus X and Y do not commute.

4.4 Energy-Crossing Relations for Braided Field Lines

Following the information provided previously, this section represents a review by Berger [30] of the energy calculation of the braided magnetic fields. Berger uses the crossing number techniques pioneered by Freedman and He [87] to derive lower bounds on the energy of braided field lines. In the early nineties Freedman and He employed knot theory to find lower bounds on the energy of topologically complex magnetic fields. These lower bounds are often used to constrain the equilibrium states accessible to magnetized fluid with a given topology.

Numerical modelling of braided magnetic fields extending between two parallel plates shows current densities increasing exponentially with topological complexity [151]. This is where Freedman and He's techniques become important since they do not involve solving non-linear partial differential equations. The quantity they define is known as the "asymptotic crossing number" and it provides a precise measure of field-line entanglement. The asymptotic crossing number is not topologically invariant. However, like the magnetic energy it has a positive minimum value for a given magnetic topology. The minimum asymptotic crossing number, multiplied by a constant coefficient, provides a lower bound for the equilibrium energy.

Braided magnetic fields are strongly aligned in one direction but possess significant transverse structure. This two dimensionality makes the derivation for braided fields

simpler than fully three dimensional knotted structures and thus minimum crossing numbers become easier to calculate [29, 250].

We begin by considering two field lines stretching between parallel planes at $z = 0$ and $z = L$. Let ϕ be the polar angle in the $x - y$ plane and observe the curves from the viewing angle $\phi = \pi/2$. At this angle, the curves exhibit a certain number of crossovers $c(\pi/2)$. Different viewing angles ϕ result in different crossing numbers $c(\phi)$ (figure 4.3) and therefore an average crossing number can be defined as

$$\bar{c} = \frac{1}{\pi} \int_0^\pi c(\phi) \mathrm{d}\phi, \tag{4.7}$$

which is independent of viewing angle.

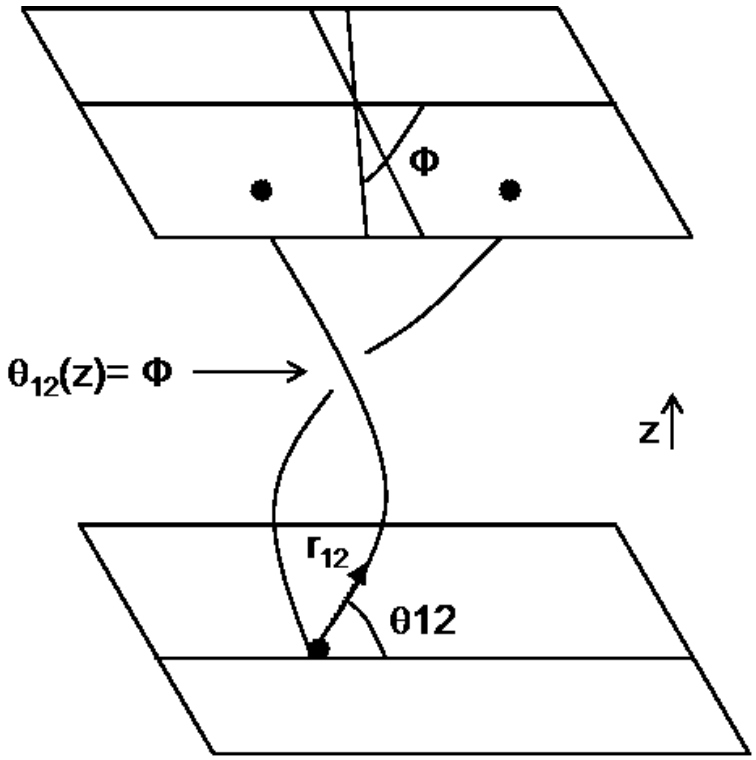

Figure 4.3: From the viewing (projection) angle ϕ, two curves will be seen to cross wherever the displacement vector $r_{12} = \phi$ or $\phi + \pi$.

One can compute the crossing number from the form of the curves. Consider that the two field lines follow the curves $\mathbf{x}_1(z)$ and $\mathbf{x}_2(z)$ where $\mathbf{x}_1(z) = (x_1, y_1)$ and $\mathbf{x}_2(z) = (x_2, y_2)$. The displacement vector $\mathbf{r}_{12} = \mathbf{x}_2(z) - \mathbf{x}_1(z)$ makes an angle $\theta_{12}(z)$ with respect to the x-axis and an observer viewing the curves from the angle ϕ will see crossovers wherever $\theta_{12} = \phi$ or $\phi + \pi$. If $\mathbf{r}_{12}(z)$ sweeps out a net angle $\Delta\theta_{12} =$

$\int |\mathrm{d}\theta_{12}/\mathrm{d}z|\,\mathrm{d}z$, then a proportion $\Delta\theta_{12}/\pi$ of observers see a crossover. Therefore,

$$\bar{c} = \frac{1}{\pi}\int_0^L \left|\frac{\mathrm{d}\theta_{12}}{\mathrm{d}z}\right| \mathrm{d}z. \tag{4.8}$$

Now, consider a set of magnetic field lines confined inside the cylinder $x^2+y^2 \le R^2$. To obtain the crossing number for the magnetic field, one must sum $\bar{c}$ over all pairs of lines to obtain

$$C \equiv \frac{1}{2\pi}\int_0^L \int\int B_{z1}B_{z2}\left|\frac{\mathrm{d}\theta_{12}}{\mathrm{d}z}\right| \mathrm{d}^2x_1\,\mathrm{d}^2x_2\,\mathrm{d}z. \tag{4.9}$$

If one lets

$$\mathbf{b}_1 \equiv \frac{\mathrm{d}\mathbf{x}_1(z)}{\mathrm{d}z} = \frac{B_\perp(\mathbf{x}_1)}{B_z(\mathbf{x}_1)}, \tag{4.10}$$

then

$$\frac{\mathrm{d}\theta_{12}}{\mathrm{d}z} = \frac{1}{r_{12}^2}(\mathbf{b}_2-\mathbf{b}_1)\cdot\theta_{12}, \tag{4.11}$$

where $\theta_{12} = \mathbf{z}\times\mathbf{r}_{12}$. Substituting (4.11) in (4.9) results in

$$\frac{\mathrm{d}C}{\mathrm{d}z} = \int\int \frac{B_{z1}B_{z2}}{2\pi r_{12}}\left|(\mathbf{b}_2-\mathbf{b}_1)\,.\,\theta_{12}\right| \mathrm{d}^2x_1\,\mathrm{d}^2x_2. \tag{4.12}$$

For fields with a strong axial component such as B_z, the topology manifests itself in the structure of the transverse field rather than in the relatively small variations in B_z [236]. If one considers $B_z = \text{const}$, then

$$\mathbf{B} = B_z(b_x, b_y, 1) = B_z(\mathbf{b}+\mathbf{z}). \tag{4.13}$$

In order to find the lower bounds on the free energy

$$E_f \equiv \frac{B_z^2}{8\pi}\int b^2\,\mathrm{d}^3x \qquad \text{with} \qquad b = |\mathbf{b}|\,, \tag{4.14}$$

we apply the triangle inequality to the integral in (4.12) to get

$$\frac{\mathrm{d}C}{\mathrm{d}z} \le \frac{B_z^2}{2\pi}\int\int r_{12}^{-1}(|\mathbf{b}_1\cdot\theta_{12}| + |\mathbf{b}_2\cdot\theta_{12}|)\,\mathrm{d}^2x_1\,\mathrm{d}^2x_2. \tag{4.15}$$

After rewriting the second term in the above equation as $\mathbf{b}_1 = b_1\mathbf{b}_1$ with $|\mathbf{b}_1| = 1$, the inequality becomes

$$\frac{\mathrm{d}C}{\mathrm{d}z} \le \frac{B_z^2}{\pi}\int b_1\int \frac{|\mathbf{b}_1\cdot\theta_{12}|}{r_{12}}\,\mathrm{d}^2x_2\,\mathrm{d}^2x_1. \tag{4.16}$$

In order to estimate the above integral, we use the vector field $\mathbf{n} = \mathbf{z}\times\mathbf{x}_1$ which maximizes $I(\mathbf{x}_1) = \int(|\mathbf{n}\cdot\theta_{12}|/r_{12})\,\mathrm{d}^2x_2$. The maximum value of $I(\mathbf{x}_1)$ is $I_{max}(\mathbf{x}_1) = Rf(a)$, where $a = |\mathbf{x}_1|/R$ and

$$f(a) = 2\left(1+\ln(1+a^2) + \frac{1-a^2}{2a}\tan^{-1}\frac{2a}{1-a^2}\right). \tag{4.17}$$

Therefore, we obtain

$$\frac{\mathrm{d}C}{\mathrm{d}z} \leq \frac{R\,B_z^2}{\pi} \int b_1 f \mathrm{d}^2 x_1. \tag{4.18}$$

Define

$$\overline{f^2} = (\pi R^2)^{-1} \int f^2 \mathrm{d}^2 x_1 \approx 13.1. \tag{4.19}$$

Using Schwarz inequality, leads to

$$\left(\frac{\mathrm{d}C}{\mathrm{d}z}\right)^2 \leq \pi^{-1} R^4\, B_z^4\, \overline{f^2} \left(\int b_1^2 \mathrm{d}^2 x_1\right). \tag{4.20}$$

Now, considering

$$C^2 \leq L \int_0^L (\mathrm{d}C/\mathrm{d}z)^2 \mathrm{d}z, \tag{4.21}$$

one finds that

$$C^2 \leq \pi^{-1} L\, R^4\, B_z^4\, \overline{f^2} \int b^2\, \mathrm{d}^3 x, \tag{4.22}$$

and this results in a lower bound for the free energy of equation (4.14) of the form

$$E_f \;\geq\; \left(8\overline{f^2} L R^4 B_z^2\right)^{-1} C^2 \tag{4.23}$$

$$\;=\; 9.54 \times 10^{-3} \left(L R^4 B_z^2\right)^{-1} C^2. \tag{4.24}$$

In order to find how far off the lower bound of (4.23) is, consider a particular configuration where $\mathbf{b}(\mathbf{x}, \mathbf{z})$ is a random vector field with correlation length much smaller than R and the distribution of field is Gaussian. If $\mathrm{d}C/\mathrm{d}z$ in equation (4.12) is averaged over many realizations, then $\langle|(\mathbf{b}_2 - \mathbf{b}_1) \cdot \theta_{12}|\rangle$ should only depend on the distance r_{12} and in the limit of zero correlation length, it will be constant. Therefore

$$\left\langle \frac{\mathrm{d}C}{\mathrm{d}z} \right\rangle = \frac{B_z^2}{2\pi} \langle|(\mathbf{b}_2 - \mathbf{b}_1) \cdot \theta_{12}|\rangle \int\int \frac{1}{r_{12}}\, \mathrm{d}^2 x_1 \mathrm{d}^2 x_2. \tag{4.25}$$

For a Gaussian distribution the bracketed term is equal to $\sqrt{2/\pi} b_{rms}$ where $b_{rms}^2 = \langle b^2 \rangle^{1/2}$ and the double integral of r_{12}^{-1} equals $16\pi R^3/3$. Hence

$$\left\langle \frac{\mathrm{d}C}{\mathrm{d}z} \right\rangle = \frac{8}{3} \sqrt{\frac{2}{\pi}}\, B_z^2\, R^3 b_{rms}, \tag{4.26}$$

and it leads to

$$E_f \;=\; 9\pi \times 2^{-10} \langle C \rangle^2 B_z^{-2} L^{-1} R^{-4} \tag{4.27}$$

$$\;=\; 2.76 \times 10^{-2} \langle C \rangle^2 B_z^{-2} L^{-1} R^{-4}, \tag{4.28}$$

which is 3.01 times the lower limit.

Energy-crossing number relation is a useful method if there is a way of calculating the crossing number C. Now consider the case of N mutually entangled flux tubes from section 4.3. We can approximate C by counting the cross overs of the N axis curves of the flux tubes. The N curves form a braid between $z = 0$ and $z = L$. Regard C_N to be the dimensionless crossing number for the N axis curves with minimum C_{min}. For simplicity, we let the N tubes have equal flux $\psi = \pi R^2 B_z/N$. Since C counts the crossings between two field lines within the same tube and C_N counts crossings between different tubes, C counts more crossings than C_N. Therefore $C \geq \psi^2 C_N \geq \psi^2 C_{min}$ and one can write the lower bound of the equation (4.23) as

$$E_f \geq \left(\frac{\pi^2}{8\overline{f^2}} \frac{C_{min}^2 \psi^2}{N^2 L} \right) \tag{4.29}$$

$$= \frac{9.04 \times 10^{-2} C_{min}^2 \psi^2}{N^2 L}. \tag{4.30}$$

This equation has a quadratic dependence on C_{min}. The important point here is that braided fields with constant B_z have similar characteristics to a system with two spatial dimensions plus time (let $z \longrightarrow t$). In the case of a three dimensional field, Freedman and He [87] found that the minimum energy grows linearly with crossing number.

In the remainder of this section, we consider magnetic fields generated by random motions. In order to investigate how photospheric motions generate structure in the coronal field, Berger uses a model with discrete filaments [30]. Since magnetic flux is extremely localized at the photosphere, the flux from one photospheric flux element may bifurcate and connect to several photospheric elements of opposite polarity. In order to accommodate this possibility, one can increase N and allow for variable flux. This process includes N points in a plane corresponding to the N foot-points of the filaments inside a coronal loop. The N points move about each other randomly according to the laws of random walk, diffusion or motion in a stochastic velocity field. This results in the braiding of the filaments. In order to find $C_{min}(t)$, the minimum value for C_{min} at time t for the braid structure, one can use the magnetic energy $E_f(t)$.

In a numerical simulation by Berger [26], he considers three photospheric flux elements that are allowed to random walk about each other as they are restricted to a disk of radius 1000 km. Once they reach the edge of the disk, they bounce back inside the disk. They move with an average velocity of $v = 1$ km/s. For step sizes

of $\lambda = 1000$ km, Berger obtains

$$C(t) \approx \frac{1}{4}\frac{vt}{\lambda}. \tag{4.31}$$

In order to find out how crossing number C_{min} varies with N after the braid is generated by random motions, one needs to fix the flux ψ and the typical diameter D of the flux tube. The flux can then be written as $\psi = \pi D^2 B_z/4$ and $R = N^{1/2}D/2$. The intensive quantity b_{rms} known as field strength can be written as

$$b_{rms} \geq 0.27 C_{min}\, D\, L^{-1}\, N^{-3/2}, \tag{4.32}$$

where b_{rms} depends on the amount of tangling per unit area. The equation (4.32) thus demonstrates that C_{min} increases with $N^{3/2}$. To see this clearly, consider N foot-points in a square array, with $N^{1/2}$ points in each row and a distance D between points. Once a point moves by distance D, then in projection up to $N^{1/2}$ extra crossings will be made. Therefore if all N points move, the increase in C_{min} would be $N^{3/2}$.

In order to find the power per unit area, consider N foot-points that are in random motion about each other. If the distance between photospheric points is d, then

$$C_{min}(t) = \beta \frac{vt}{d}\, N^{3/2}, \tag{4.33}$$

where β is a dimensionless parameter. Because of the clumping of flux at super-granule boundaries, the photospheric distance d may be less than the diameter of coronal tubes D. Using the lower bound of equation (4.29), the power input per unit area is given by

$$\begin{aligned} P &= \left(N\pi D^2/4\right)^{-1}\, \mathrm{d}E_f/\mathrm{d}t \\ &= \left(\pi^3/16\overline{f^2}\right)\, \beta\, C_{min}\, N^{-3/2}\, \left(B_z^2\, D^2\, v/Ld\right). \end{aligned} \tag{4.34}$$

When the mean value of b reaches some critical value μ, the energy input saturates. This is the result of reconnection releasing energy at the same rate as the energy is pumped in at the photosphere. In this case, the energy is

$$E_f = LN\pi\, (D^2/4)\, B_z^2\, \mu^2. \tag{4.35}$$

From (4.29) and (4.35), the minimum crossing number is

$$C_{min} = \frac{2^{5/2}\, \overline{f^2}^{1/2}\, N^{3/2}\, L\, \mu}{\pi^{3/2}\, D}. \tag{4.36}$$

And the power at saturation is

$$P = \left(\pi^{3/2}/2^{3/2}\, \overline{f^2}^{1/2}\right)\, \beta\, \mu\, \left(v\, B_z^2\, D/d\right). \tag{4.37}$$

Since $\pi^{3/2}/2^{3/2}\,\overline{f^2}^{1/2} = 0.543$, if $B_z = 100G$, $\beta = 0.06$ (as indicated by Parker [174]), $v = 1$ km/s and $\mu = 0.25$, then $P = 8{\times}10^6 D/d$ ergs cm^{-2} s^{-1}. This power is sufficient for an active region, provided $D/d \gtrsim 2$. Berger concludes that since d measures typical distances between foot-points at the photosphere, gathering of foot-points at the boundaries reduce d relative to the coronal flux tube diameter D.

4.4.1 The Fragmentation of Flux Tubes

The coronal flux tubes have a finite lifetime. This is because the reconnection of coronal loops releases magnetic energy and heats the corona and, as a result, the foot-points regularly fragment and reform. Hence, the fields inside one newly formed foot-point may have belonged to several old foot-points and the new foot-points may connect to the old coronal tubes. However, the energy calculation in previous section may not be strongly affected by this fragmentation. To calculate power P in terms of the lifetime of coronal flux tubes, Berger [31] supposes that photospheric foot-points have a lifetime of τ_f. For simplification, he assumes a separation of time-scales: $\tau_c \ll \tau_f \ll \tau_d$, where τ_c is the velocity correlation time and τ_d is the dissipation time. Consider a loop of length L with many individual tubes of flux ψ^*. If between time $t = 0$ and $t = \tau_f$ each tube is independently twisted, the rms twist at $t = \tau_f$ on one tube from equation (4.1) is

$$\mathcal{T}(\tau_f) = \frac{v}{\pi\lambda}\left(\frac{3\tau_c\tau_f}{2}\right)^{1/2}. \tag{4.38}$$

If, at time τ_f, the foot-points of this tube fragment and the fragments are gathered into new foot-points, then the twist described by equation (4.38) will survive in the corona. Also, subsequent foot-point rotations push a more twisted structure into the corona and the result is a highly braided system. The twist at time t is then

$$\mathcal{T}(t) \approx \frac{\mathcal{T}(\tau_f)\,t}{\tau_f} = \frac{v}{\pi\lambda}\left(\frac{3\tau_c}{2\tau_f}\right)^{1/2} t. \tag{4.39}$$

As in (4.4), using the energy density w and the length of the braid, one can find the power

$$P = \frac{L}{2}\frac{\mathrm{d}w}{\mathrm{d}t} = \frac{B_z\psi^*}{4L}\,\mathcal{T}\,\frac{\mathrm{d}\mathcal{T}}{\mathrm{d}t} = \frac{B_z\psi^*}{4L}\,\mathcal{T}\,\frac{v}{\pi\lambda}\left(\frac{3\tau_c}{2\tau_f}\right)^{1/2}, \tag{4.40}$$

which has a direct correlation with the value of $\mathcal{T}$, where $\mathcal{T}$ is an indicator of how excited the field is. At a certain level of stress, power input balances losses to reconnection, and this level of stress is described by the parameter μ

$$\mu = \frac{\overline{B_\perp}}{B_z} = \frac{8\pi w^{1/2}}{B_z} = \frac{2^{1/2}\pi R_c\mathcal{T}}{L}. \tag{4.41}$$

Using the above relation and (4.40), one can write the power as

$$P = \frac{\mu\, R_c\, B_z^2\, v}{8\,\pi\,\lambda} \left(\frac{3\tau_c}{\tau_f}\right)^{1/2}, \tag{4.42}$$

where R_c is the radius of the coronal flux tube and is approximately equal to the distance between photospheric foot-points.

Chapter 5

Solar Flares

5.1 Introduction

One of the fundamental problems of solar physics is explaining the trigger and energy release process of flares. The magnetic energy stored in the coronal magnetic field is the energy source of flares. Magnetic reconnection is the key to this energy process: when misaligned magnetic field lines are brought together, they can reconnect and, as a result release the stored magnetic energy in the form of a flare [132, 241]. Flares (figure 5.1) are composed of many smaller events [175, 217], and therefore the corona is heated by many small non-thermal events [174, 216]. The random foot-point motions of magnetic fields anchored in the photosphere will lead to many current sheets in the corona with associated tangential discontinuities in the magnetic field [141]. As stated in chapter 2, observations [86] suggest that the magnetic field of the Sun occurs in flux-tube bundles in the solar atmosphere, thereby flare models invoke flux tube collision as the trigger for flares. One major proposal is that the flares could be the result of an interaction between two or more flux tubes [80, 102, 119]. In fact, the collision and reconnection of flux tubes could be involved in two ribbon flares [120, 146, 217], X-ray bright points [185], and compact flares [113]. In all of these models, the magnetic field lines are brought into contact by the collision of flux tubes, and their subsequent reconnection releases energy stored in the flux-tube configuration, resulting in a flare. This interaction may take place when a new flux tube appears into the solar atmosphere below the existing one and the two tubes collide as the new flux tube rises into the corona [83, 107]. Other collisions could be the result of the foot-point motions of two existing coronal flux tubes where differential rotations or convective motions move the tubes and they hit the photosphere, bringing them into contact higher up in the corona [102]. In either case, there is a complex active region with several flux tubes present and the flux

tubes are close enough to collide. This is in agreement with observations of those such as Machado [145] who found that many flares are the result of an interaction between two or more bipoles. A study by Raoult et al. [188] on a large sample of flares concluded that impulsive flares are due to rapid interactions between two or more magnetic structures. Also, the soft X-ray flare observations from Yohkoh demonstrate that the flares occur because of interactions in complex loop magnetic structures [83].

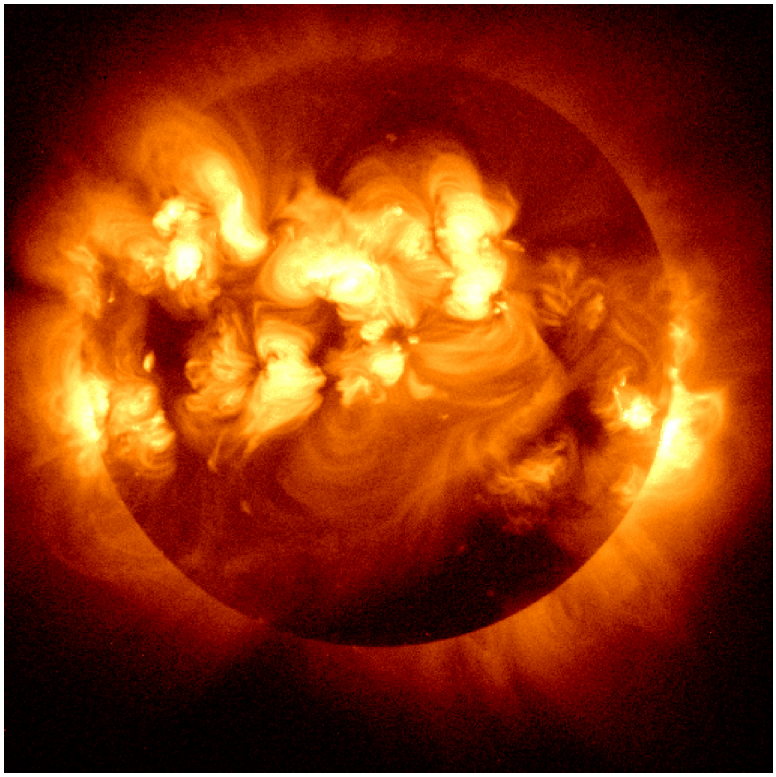

Figure 5.1: Image of solar flares from Yohkoh.

A complete theory of solar flares or of any astronomical objects is expected to address the question of the physics underlying individual events as well as the overall distribution of the observed events, since these two issues are intimately related. An example is the physics of stellar structure and evolution, and the distribution of stars on the H-R diagram. Solar flare observations indicate that the flares have a large dynamic range in both energy and duration. Their total energy release ranges from less than 10^{27} ergs in the smallest observable flares to of the order of 10^{33} ergs, while their durations range from order of less than one second to several thousand seconds [143]. Also, the distribution of solar flare peak luminosities is observed to be a power law over a range of more than four orders of magnitude, extending down to the limits of observation [68, 131]. The morphology of flaring regions demonstrate

that there is structure on all length scales from more than 10^9 cm down to below 10^8 cm [220]. Therefore, any complete theory of solar flares must consider not only the observed emissions and morphology of flares, but also the reasons behind these broad distributions [143]. According to Parker [172, 173, 175], the statistical properties of large-scale dynamics of complex magnetized plasmas can arise from energy release processes.

As stated earlier, the occurrence of solar flares is the result of rapid release of magnetic energy in active regions. This energy is built up by the convective motion of gas in the photosphere and below [143]. The magnetic field below the photosphere is convected by the highly conducting fluid. This is the result of the fact that the ratio of gas to magnetic pressure is more than one, i.e. $\beta = nkT/(\mathbf{B}^2/8\pi) \gg 1$ (n is the number density of gas, k is Boltzman's constant and T is the absolute temperature of gas). Therefore, the magnetic field which extends up into the low-density corona where $\beta \ll 1$ is continually shuffled by the random fluid motions. These convective velocities are much slower than the Alfvén velocities and thereby the behaviour of the large-scale coronal magnetic field is described by a quasi-static evolution of the equilibrium magnetic field. This equilibrium configuration is a response to the changing boundary conditions at the photosphere. It is important to note that instabilities can occur in these structures, resulting in rapid changes in the magnetic field on time-scales of the order of the Alfvén crossing time. The magnetic energy released in such an instability in the form of flare is converted into thermal energy, energetic particles, and radiation [143]. The solar particles accelerated by the flares, interact with the Earth's magnetic field and ionosphere. This results in disruption to radio communications and damage to satellites [132].

The plan of this chapter is as follows. The following section examines the collision and reconnection of magnetic flux tubes resulting in solar flares. We analyse a model by Linton, Dahlburg and Antiochos [132], where the reconnection process is studied by a simulation of the collision of pairs of twisted flux tubes. Section 5.3 provides a review of solar flare distribution based on self-organized criticality models.

5.2 Reconnection of Twisted Flux Tubes

As we discussed in chapter 3, a right-handed twisted tube has positive helicity, where as a left-handed twisted tube has negative helicity. Flux tubes pairs are then either co-helical, with helicities of the same sign, or counter helical, with opposite helicities. It is therefore important to distinct between the two, since when counterhelicity flux

tubes interact, they annihilate each other's helicity and, as a result, release magnetic energy. On the other hand, the helicity of co-helicity flux tubes will add together, and the energy release possibilities are reduced [132].

Linton et al. [132] simulated flux tube interactions in a box of size 2π where the tubes come into contact in the centre of the box ($x = y = z = 0$). As soon as the tubes are initialized, one is in front with an angle ($x = \pi/4$) and the other has angle ($x = -\pi/4$) and their axes form an angle ϕ (figure 5.2) where each tube holds a uniform twist. In a two dimensional reconnection, the symmetry and the restriction to a single spatial plane result in the reconnected field lines being pulled away from the interaction region by magnetic tension [182]. In three dimensional reconnection, the fields of equal strength reconnect with each other if any component of the two fields is oppositely directed [212]. This section looks at the case when two field lines from the same radial shell of the flux tubes interact. It is important to note that with twisted flux tube interactions reconnected, there is no guarantee that the field lines can be pulled away from the reconnection region. There is a possibility that reconnected field lines wrap around unreconnected field lines, and this wrapping may result in enhancing the reconnection rate by pulling the flux tubes together more quickly or else curb it by congesting the reconnection region. For example in the simulations of flux tube reconnection performed by Ono et al. [167], for parallel or anti-parallel flux tube collisions, the reconnection rate increases with increasing radially averaged field line angles. Their results demonstrate that a flux tube pair with an averaged field line angle of π has three times the reconnection rate of a flux tube pair with an averaged field line angle of $\pi/2$. And when the angle is between $\pi/2$ and π, the field lines reconnect in such a way as to clear the interaction region and then pull the flux tubes together [202]. Furthermore, the field lines that reconnect with angles of less than $\pi/2$, remain between the two tubes and may even remain in the interaction region, preventing the tubes from coming closer together.

Thus, magnetic reconnection depends on the angle between the magnetic field lines when they come into contact. One can find the exact field-line angles if one assumes that the tubes are not deformed before hitting each other. For instance if the tube axes sit in $y - z$ plane at $x = \pm\pi/4$, the tubes first come into contact along the x-axis, and since the tubes have the same size and same radial profiles, the field line pairs that interact will be in the same radial shell as in their respective tubes. In order to find the interaction angle of these field lines, one needs to look at $\mathbf{B}_1(r) \cdot \mathbf{B}_2(r)$ on the x-axis, where $\mathbf{B}_1(r)$ is the field of the reference tube, tube 1, and $\mathbf{B}_2(r)$ is the field of the rotated tube, tube 2.

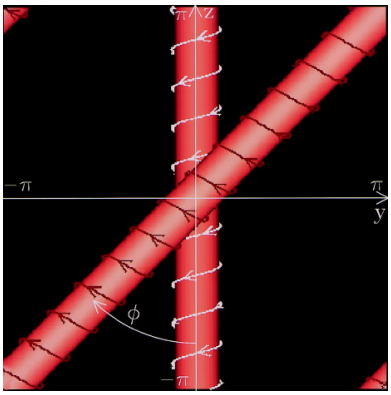

Figure 5.2: A pair of right-hand flux tubes with a contact angle of $\phi = \pi/4$. Figure from Linton et al. [132].

To perform the field-line angle calculation, one needs the field of each tube along the segment of x-axis running from the centre of the tube to the edge of the tube near to the interaction region. Tube 1 is centred at $x = -\pi/4$ and it is parallel to the z-axis, so the magnetic field is

$$\mathbf{B}_1(r_1) = -\mathbf{z}\,\mathbf{B}_z(r_1) - \mathbf{y}\,\mathcal{T}\,r_1\,\mathbf{B}_z(r_1), \tag{5.1}$$

with

$$\mathbf{B}_{\text{axial}}(r) = \frac{\mathbf{B}_0}{1+\mathcal{T}^2 r^2}, \tag{5.2}$$

and

$$\mathbf{B}_{\text{azimuthal}}(r) = \mathcal{T}\,r\,\mathbf{B}_{\text{axial}}(r). \tag{5.3}$$

where $r_1 = \pi/4 + x$ is in the range of $-\pi/4 < x < -\pi/4 + R$, $0 \le r \le R$, $\mathcal{T}$ is the twist parameter and $\mathbf{B}_0$ is the magnetic field strength. The tubes profile is given in cylindrical coordinates with $0 \le r \le R$ where R is the major radius of the cylinder. Tube 2 is centred at $x = \pi/4$, and it is oriented at an angle ϕ to the z-axis. Its magnetic field is then

$$\mathbf{B}_2(r_2) = -\mathbf{B}_z(r_2)\,(\mathbf{z}\cos\phi + \mathbf{y}\sin\phi) \pm \mathcal{T}\,r_2\,\mathbf{B}_z(r_2) \times (-\mathbf{z}\sin\phi + \mathbf{y}\cos\phi), \tag{5.4}$$

where $r_2 = \pi/4 - x$ and it is in the range $\pi/4 - R < x < \pi/4$. The plus/minus sign is for a right- or left-hand tube respectively. The angle θ where the two field lines meet at radius $r_1 = r_2 \equiv r$ is

$$\cos\theta = \frac{\mathbf{B}_1(r)\,\cdot\,\mathbf{B}_2(r)}{|\mathbf{B}_1(r)|\,|\mathbf{B}_2(r)|}. \tag{5.5}$$

Substituting the appropriate expressions into equation (5.5), one finds that

$$\cos\theta = \frac{(1 \pm \mathcal{T}^2\,r^2)\cos\phi + (1 \pm 1)\sin\phi}{1+\mathcal{T}^2 r^2}. \tag{5.6}$$

Therefore, the field line angle θ for right-left (RL) pair at a collision angle ϕ is

$$\theta = \phi. \tag{5.7}$$

For anti-parallel field lines ($\theta = \pi$), the lines reconnect most easily. As a result, for counter helicity (RL) tube interactions, tubes with contact angles near $\phi = \pi$ reconnect most efficiently. However if, on the other hand, the contact angle of an RL tube collision is decreased to $\phi = \pi/2$, the reconnection loses its efficiency [167]. And, as θ and ϕ decrease below $\pi/2$, the reconnection becomes inhibited by field lines blocking the interaction region, and this results in the reconnection being stopped as soon as it starts. The relation between θ and ϕ demonstrates that there should be a symmetry in the interactions for counter helicity collisions. For instance any tube at $\phi = \theta + \pi$ will interact in the same way as a tube at $\phi = \pi - \theta$.

Linton, Dahlburg and Antiochos [132] conclude that there are four types of interactions that can take place between the tubes. They are: bounce, merge, slingshot and tunnel. We discuss each of these four types in following subsections.

5.2.1 Bounce Interaction

If two field lines are brought together in such a way that their magnetic fields point in the same direction, they do not reconnect. Therefore, if in the collision of the flux tubes, the pair are nearly parallel, the reconnection would be limited. This happens for the case RL0, where the axes of the two tubes are parallel and the angle between the field lines is exactly zero. In this case, there is no reconnection since the tubes bounce off each other (figures 5.3(a) and 5.3(b)) [202]. The same process occurs in the collision of anti-parallel right-hand tubes (figures 5.3(c) and 5.3(d)).

Apart from the weak reconnection and the resulting bounce off of the flux tubes, figure 5.3 shows how the current-driven kink instability is excited when the tubes hit each other. Such kinks are excited because of the contact at the middle of the tubes (figures 5.3(a) and 5.3(c)) and it results in the tubes arching away from this point. The kink dispersion relation for a flux tube indicates that a right hand kink will develop for a right-hand twisted tube ($\mathcal{T} > 0$) and vice-versa for a left-hand tube [133].

The magnetic energy released from the reconnection in the bouncing interaction is negligible, since more than seventy percent of the magnetic energy is lost due to the direct conversion of magnetic energy into heat as a result of magnetic diffusion.

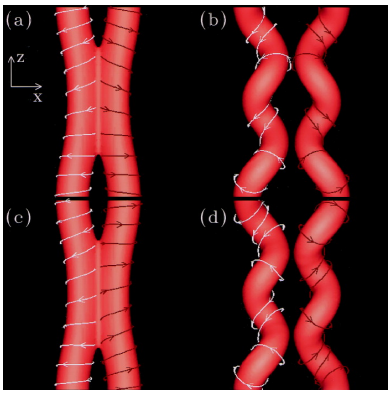

Figure 5.3: Bounce interaction. Figure from Linton et al. [132].

5.2.2 Merge Interaction

In merge interaction, reconnection starts and continues efficiently as the flux tubes come into contact and then gradually shuts off as the tube axes approach each other (figure 5.4). The field line in figure 5.4(a) has reconnected twice and goes from the left-hand tube completely around the right-hand tube and returns to the left-hand tube. As it can be seen, it has moved out of the reconnection region between the two tubes, allowing field lines at the inner radial shells also to reconnect. Also, as the tubes wrap around each other, the magnetic tension pulls the tubes together intensifying the reconnection rate. As figure 5.4(c) indicates the two parallel right-hand tubes merge into a single right-hand tube. It is important to note that the merge reconnection brings the tubes into a configuration with weaker magnetic field gradients than that of the unreconnected tubes. Therefore, diffusion is less effective at dissipating the field of merged tubes than at dissipating that of the bounced tubes, so despite the fact that energy is released from the reconnection, here the merged tubes will have the same magnetic energy as that of the bounced tubes. On the surface of the Sun however, this is not the case since diffusion occurs on a much longer time-scale.

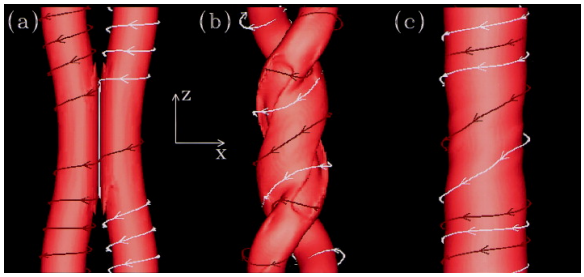

Figure 5.4: Merge interaction. Figure from Linton et al. [132].

5.2.3 Slingshot Interaction

Slingshot interaction takes place when a right and left-hand tube with antiparallel axial fields collide. The axial and azimuthal fields are antiparallel when the flux tubes collide and they remain so as the reconnection continues (figure 5.5). The slingshot occurs when flux tubes of opposing helicity collide in the range of $\pi/2 \leq \phi \leq 3\pi/2$, releasing enough energy to cause a flare. Here, reconnection takes place quickly and it results in annihilation of the magnetic flux. Because the tubes are pushed together at the centre of the simulation box, the field lines reconnect first (figure 5.5(a)) before being annihilated (figure 5.5(b)). In fact, the tubes reconnect into new tubes that form elbows at the interaction region and then they slingshot away from the interaction region. This is the result of the tension among the field lines. It is the most energetic of the interaction types because the flux is annihilated and the twist is cancelled.

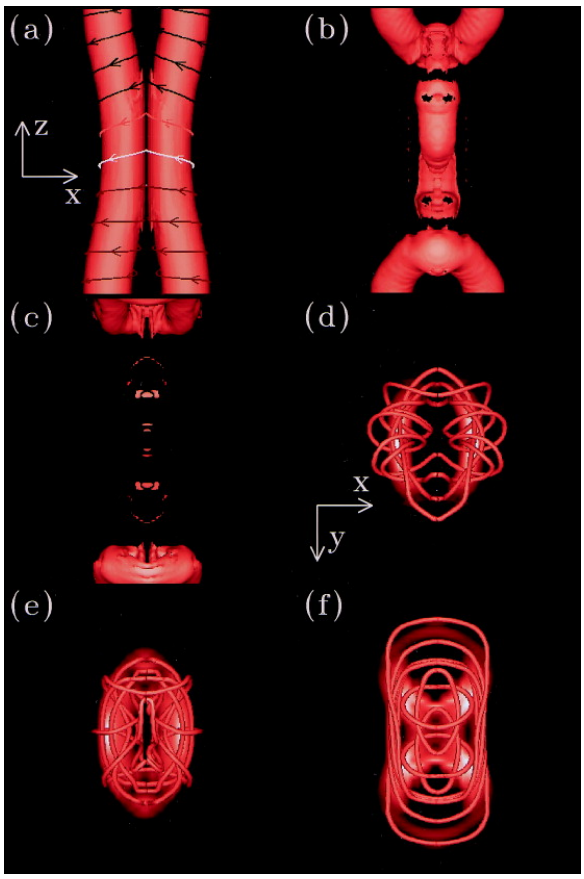

Figure 5.5: Slingshot interaction. Figure from Linton et al. [132].

In chapter 6 we consider the case of micro-flares, where after the braiding is built up along the flux tubes, once the angle between the strings reaches $\pi/6$ or over, the reconnection occurs.

5.2.4 Tunnelling Interaction

The final basic interaction is the tunnelling case (figure 5.6) where two right-hand flux tubes collide at $\phi = 3\pi/2$. The field lines in these tubes undergo two reconnections each [3, 60] and this allows the tubes to pass through each other (figure 5.6(b)). There is similarity between the tunnelling interaction and both the slingshot and merging case since there is significant reconnection occurring and the topology of the flux tubes are changed. However the major difference is that here the two flux tubes keep their identity rather than integrating into a new combination. The topological change is the result of how the tubes move around each other. The energy release associated with this type of reconnection is small however because hardly any flux is annihilated and less twist cancelled.

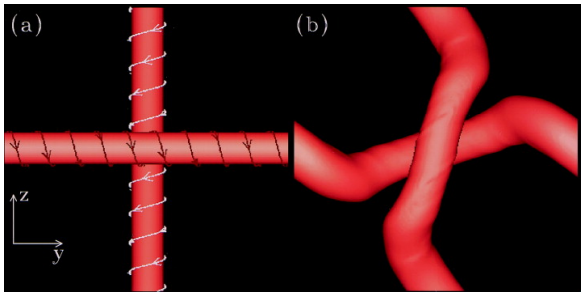

Figure 5.6: Tunnelling interaction. Figure from Linton et al. [132].

5.3 Distribution of Solar Flares

Observations show that the distribution of solar flare hard X-ray bursts is a power law in peak photon flux with logarithmic slope 1.8 [62, 68, 131]. The power law index of this distribution is independent of the solar cycle. This indicates that the underlying mechanism giving rise to the power law distribution is insensitive to the level of coronal activity. Lu and Hamilton [142] suggest that there is a connection between the distribution of solar flares and a phenomenon known as *self-organized criticality* (SOC).

In order to explain the prevalence of power law, or scale-invariant correlations extending over many decades in complex dynamical systems, Bak, Tang and Wiesenfeld [14, 15] proposed the concept of self-organized criticality. Their models suggest that extended systems with many metastable states can naturally evolve into a critical state with no intrinsic length or time-scale. Experiments [11], as well as numerical simulations [51, 115], have proved the existence of such critical states.

This section looks at two SOC models. The first model is the avalanche model by Lu and Hamilton [142] and the second is the forest fire model by Bak, Chen, Tang [13] and Drossel and Schwabl [74].

5.3.1 Avalanche Model

A simple example of a critical state is an avalanche model. As sand is added to the sand pile, the average slope of the sandpile increases. It then reaches a state where it remains approximately constant. As this self-organized critical state is reached, the addition of more sand results in avalanches which readjust the local shape. Note that the critical state is insensitive to the initial condition. It does not require any fine tuning of parameters and it is an attractor of the dynamics of the system. As soon as the perturbations cause disturbances that are able to propagate the length of the system, the system becomes stationary. When the system is in a critical state, it has a distribution of minimally stable regions of all sizes. Therefore small perturbations give rise to avalanches of all sizes from the smallest possible avalanche such as a single sand grain up to the size of the entire system. A featureless power law spectrum of avalanche sizes results since there is no characteristic length scale in the system. In numerical sand pile models, the sand grains are added at random to the system. The grains then shift downward whenever the local shape transcends some critical value. As the slope is readjusted by shifting grains to neighbouring sites, this results in forcing the slope at a neighbouring site to transcend the critical value, this causes the avalanche to grow. The avalanche continues for as long as the slope is greater than the critical value. The spectral index of the resulting power law avalanche size distribution is persistent and insensitive to the value of critical slope [15, 115]. It is important to note that different physical systems have different spectral indices, which depends on the number of spatial dimensions and the symmetry of the system [15, 115, 165]. The existence of a self-organized critical state requires a local instability. This instability takes place whenever some local parameter transcends a critical value, resulting in a transport process which changes the value of this quantity at nearby sites with the possibility of causing the value of the parameter at neighbouring sites to also exceed the critical value.

If the magnetic energy release process has a local instability, it triggers the release of magnetic energy at nearby sites and therefore results in the coronal magnetic field system being driven to a self-organized critical state. Lu and Hamilton [142] suggest that the coronal magnetic field corresponds to a sand pile. In their model the random twisting of the magnetic field by photospheric convective motions plays

the same role as the addition of sand grains. Parker [174] suggests that when the magnetic discontinuity angle θ between the magnetic field vectors on opposite sides of a particular current sheet is less than some critical angle θ_c, magnetic reconnection continues slowly due to the high conductivity of the coronal plasma. This results in energy being stored in the twisted magnetic field. When $\theta > \theta_c$, reconnection continues, this reduces θ rapidly, and hence dissipates the energy in the transverse magnetic field. The change in the magnetic field strength and topology is the result of reconnections, and it corresponds to the sliding grains of sand to neighbouring sites. If the discontinuity angle at some neighbouring current sheets is increased above θ_c, it will cause additional reconnection events. Therefore, one can conclude that the coronal magnetic field is driven to a state with regions of all sizes on the verge of instability. Lu and Hamilton identify the reconnection avalanches with solar flares. The energy process in these solar flares is thus understood to be avalanches of many small reconnection events [143]. Flares of all sizes are the result of the same physical process whereby the size of a given flare is determined by the number of elementary reconnection events.

To illustrate the properties of the self-organized field configuration, Lu and Hamilton construct a lattice model of reconnection. Consider a three dimensional grid of points with a three component vector $\mathbf{B}_i$ representing the average magnetic field in a cell, where i represents the spatial location on the grid. The local magnetic field gradient $\mathrm{d}\mathbf{B}_i$ is the difference between the local magnetic field and the average of its six nearest neighbours $\mathbf{B}_{nn}$,

$$\mathrm{d}\,\mathbf{B}_i = \mathbf{B}_i - \frac{1}{6}\,\Sigma_{nn}\,\mathbf{B}_{nn}. \tag{5.8}$$

When the magnitude of the gradient is greater than a critical value $|\mathrm{d}\mathbf{B}_i| > B_c$, the configuration is unstable to reconnection. When a reconnection instability takes place, the magnetic field is vertically cancelled by transporting one-seventh of the gradient vector onto each of its six nearest neighbours

$$\mathbf{B}_i \to \mathbf{B}_i - \frac{6}{7}\,\mathrm{d}\mathbf{B}_i, \qquad \mathbf{B}_{nn} \to \mathbf{B}_{nn} + \frac{1}{7}\,\mathrm{d}\mathbf{B}_i, \tag{5.9}$$

therefore the local field becomes equal to the average of its neighbours, and $\mathrm{d}\mathbf{B}_i \to 0$. If the field at nearby positions then satisfies the instability condition, it results in additional reconnection events. The amount of energy released by each reconnection event is

$$\Delta \sum_j B_j^2 = \left(\frac{6}{7}\right) |\mathrm{d}\mathbf{B}_i|^2 . \tag{5.10}$$

Lu and Hamilton start their computation with a uniform magnetic field where they drive the system by adding a random vector $\delta\mathbf{B}$ to a random position on the grid. If the magnetic gradient exceeds the critical value $\mathbf{B}_c$, the field is readjusted according to equation (5.9). After the magnetic gradient is recalculated, each new unstable point undergoes a reconnection according to equation (5.9). The field is permitted to relax until the magnetic gradient is again everywhere less than the critical value B_c. Another random vector is then added, and this process is repeated.

As Lu and Hamilton anticipated, the field is driven to a self-organized critical state with a power law distribution of event sizes. The occurrence distributions of events versus total energy, peak flux, and duration follow a power law distribution. The energy release distribution is

$$N(E) \propto E^{-\tau}, \tag{5.11}$$

and it is a power law in total energy released E with logarithmic slope $\tau = 1.4$. The peak flux distribution is

$$N(P) \propto P^{-\alpha}, \tag{5.12}$$

which is also a power law in peak flux P with logarithmic slope $\alpha = 1.8$. The duration distribution is predicted to be a power law. However, it has a cutoff due to the finite size of the grid [115]. Finally, the distribution of solar flare avalanche or energy release time T is also a power law

$$N(T) \propto T^{-\eta}. \tag{5.13}$$

The determination of the energy release time distribution from X-ray observations is a difficult task since the duration of flare emissions can be substantially longer than T. This is due to a number of effects including thermal emission from plasma heated during the impulsive phase of the burst [144]. Also, measuring the lifetime of small flares is hard because of the obscuring effect of the background that comes from nonsolar sources. All three distributions demonstrate deviations from power law behaviour at large sizes due to the finite-sized grid and at small sizes due to the finite resolution of the lattice.

Note that if the random values of the components of δB are symmetric about zero, the magnetic field is decreased as often as it is increased. Therefore the field configuration is not driven to a self-organized critical state. This is similar to the situation whereby sand grains are subtracted from a sandpile as often as they are added, so the sandpile never reaches the critical value. The self-organized critical

system has randomly occurring events. These events release energy E in time T giving rise to an energy release rate $L(x,t)$ which is a function of position and time. The integration of energy release rate $L(t)$ over position results in a time-varying signal whose spectral power $S(\omega)$ is a power law [15] in frequency ω

$$S(\omega) = \left| \int_{-\infty}^{\infty} L(t) \exp(i\omega t) \mathrm{d}t \right|^2 \propto \omega^{-\beta}, \tag{5.14}$$

where $\beta = (\tau - 3)(1 - \eta)(\tau - 1)$. This provides a direct relation between the power law indices which can be tested by observations. Lu and Hamilton's model results in a power law $S(\omega)$ with $\beta \approx 2$.

Although admittedly, Lu and Hamilton over simplify the picture of flares, their model contains some essential physics underlying the distribution of flares. The natural consequences of a self-organized critical state are that first the flare size spectrum is a featureless power law, and second that the spectral index of the flare distribution is constant over the solar cycle, even though the total flare occurrence rate changes. One can explain the variation in flare occurrence rate with the solar cycle by either the average energy released in an elementary reconnection event, or by the rate of energy input into the magnetic field with the solar cycle.

Lu and Hamilton conclude that since the classification of flares into nanoflares, microflares, and giant flares is arbitrary, there is no preferred scale and therefore the fundamental energy release structure is the same for all flares of all sizes. However, observations suggest that flares of different sizes have different characteristics. For example, the larger flares tend to have harder X-ray spectra, and the X-ray spectral index is hardest during the peak of the flare. This may be explained that because electrons are initially accelerated in a particular reconnection region, they can be further accelerated as they propagate through other reconnection regions. Also, larger flares will have more reconnection events, and the number of active reconnection sites will be greatest at flare maximum. It is important to note that the duration of an elementary reconnection must be less than the rise time of a solar flare which consists of many elementary events since the time it takes for the reconnection avalanche to spread to neighbouring sites is roughly the duration of a single event. Therefore the energy release time of an elementary reconnection event is expected to be much less than one second [69].

5.3.2 Forest Fire Model

The forest-fire model is a model that consists of dynamical systems displaying self-organized criticality. However it does not behave critically on very large physical scales. The forest fire model was introduced by Bak, Chen and Tang [13], where they studied the distribution of fire and its dependence on the driving force. In this model there is a d-dimensional hypercubic lattice with L^d sites. Each site is occupied by either a tree, a burning tree or is empty. The state of the system is defined by the following rules:
(i) trees grow with small probability p from empty sites at each time step.
(ii) trees on fire will burn at the next time step.
(iii) the fire on a site will spread to trees at its nearest neighbour sites at the next time step.
The important parameter in this model is the growth rate of the trees. The forest is characterized by the correlation function $\xi(p) \propto p^{-\nu}$. The system is critical in the limit $p \to 0$ where the fire correlation length diverges. This results in the system being in a critical state as long as trees grow slowly. If the correlation length is larger than the size of the system, the fire will die out within a time of the order of the linear size of the system. However, when the correlation length is smaller than the size of the system, the forest fire is sustained [13]. If the system size is larger than the correlation length of the fire, the model assumes a steady state with finite fire density [74].

Bak, Chen and Tang [13] start their simulation of the forest fire on lattices of sizes up to 256^2 in 2d and 64^3 in 3d. Also, periodic boundary conditions are chosen. Starting with a homogeneous distribution of trees and fires, the forest fire evolves to a stationary state for $p > p_c$, where $p_c \propto L^{-1/\nu}$. Measuring the number distribution $D(r)$ of fires at a distance r from a chosen site on fire ($D(r) \propto r^{D-1}$), one obtains the fractal dimension: $D = 1.0 \pm 0.2$ in 2d and $D = 2.5 \pm 0.2$ in 3d. This value of D agrees with experimental observations for turbulence [149]. Using the fractal dimension, one obtains the power law dependence of ξ on p where the total number of trees burned down is equal to the total number of trees grown and that is $L^d p$. It is also equal to the total number of uncorrelated domains $(L/\xi)^d$ multiplied by the number of trees burned down in a given domain ξ^D. Therefore, we have $\xi(p) \propto p^{-\nu}$ with $\nu = 1/(d - D)$, with $\nu \approx 1.0$ in 2d and $\nu \approx 2.0$ in 3d [13].

Grassberger and Kantz [98], as well as Mossner, Drossel and Schwabl [160], performed computer simulations of the forest-fire model with values of p smaller than

those used by Bak, Chen, and Tang. These simulations demonstrate that the forest-fire model is not critical but it becomes more and more deterministic with decreasing p and develops regular fire fronts. The size of these spirals, as well as the distance between them is of the order $1/p$. The temporal fire-fire correlation function oscillates regularly with a period proportional to $1/p$. In comparison, a critical system should contain fire fronts of all sizes up to the correlation length, and their temporal correlation function should show a power law spectrum of frequencies. Drossel and Schwabl [74] argue that the reason there are no fire fronts smaller than $1/p$ is that the trees that are next neighbours belong to the same forest cluster. A tree only catches fire when one of its neighbours burns. Therefore a small forest cluster can not be ignited and as a result it grows until it becomes part of a burning cluster. Since the fire burns constantly in the steady state, a burning forest cluster must be so large that trees grow at one end while the fire burns the other end, i.e. the diameter of a burning forest cluster is proportional to $1/p$, and thereby the size of a fire front is also proportional to $1/p$.

The forest-fire model becomes critical once a mechanism allows the burning of small forest clusters. Drossel and Schwabl therefore introduce a lightning parameter f and a rule that a tree ignites with probability f even if no neighbour site is burning and an empty space fills with a tree with probability p. Therefore, the controlling parameter of the model is f/p and $(f/p)^{-1}$ gives the average number of trees planted between two lightning strikes. In order to understand how criticality grows in the forest fire model, they assume a forest cluster where a cluster is assumed to be a coherent set of cells, all of which have the same state and are being burned down instantaneously as a result of one of the trees being struck by lightning. This is the case where the dynamics are invariant except for a change in the time-scale when f and p are multiplied by the same factor. If $\bar{\rho}$ is the mean overall forest density in the system in the steady state, the average number of lightening strikes in the system during t time steps is $tf\bar{\rho}L^d$. Also, the average number of trees grown in the system during t time steps is $tp(1-\bar{\rho})\,L^d$. Accordingly, the average number of trees extinguished by a lighting strike is

$$\bar{s} = (f/p)^{-1}\,(1-\bar{\rho})/\bar{\rho}. \tag{5.15}$$

To prevent finite-size effects, one should choose the number of sites L^d to be much larger than the largest forest cluster. For finite values of f/p, the value of $\bar{s}$ is independent of L. If, for small values of f/p, the $\lim_{f/p\to 0}\bar{\rho} < 1$, then equation (5.15) corresponds to a power law of the following form

$$\bar{s} \propto (f/p)^{-1}. \tag{5.16}$$

Also, if for small values of f/p, the mean forest density $\bar{\rho}$ was near 1, the largest forest cluster would include a finite percentage of all trees in the system, and the average number of trees burned by a lightening strike would diverge in the limit $L \to \infty$. This happens in contradiction to equation (5.15). Therefore a critical point in the limit $f/p \to 0$ is expected.

The critical behaviour of the forest fire model can be compared to the sandpile model whereby a separation of time-scales is needed. Sand should be added slowly compared to the lifetime of an avalanche. This corresponds to the condition that a forest cluster burns promptly. In the forest-fire model, the power law distribution of fire clusters is a result of a second separation of time-scales $p^{-1} \ll f^{-1}$. This guarantees that a large amount of energy is deposited in the system between two lightning occurrences and thereby a large number of trees is destroyed by a lightning strike [13, 74].

Chapter 6

Self-Organized Braiding of Coronal Loops

6.1 Introduction

Observations of coronal loops by Trace and Stereo reveal a beautiful and highly regular structure. In many regions the loops seem to be of similar diameters and almost parallel. This coherence in and between loops is surprising, considering the fragmented nature of magnetic field generation and release in the solar atmosphere. How can the random processes thought to exist in the corona lead to such well-organized structures?

This puzzle may relate to two others: how are the coronal loops heated? And why is the distribution of flare energies a power law? The structure of a loop must be strongly affected by magnetic reconnection within the loop, as well as larger scale reconnection with other loops. In the Parker theory of coronal heating, a large number of small flares (*nanoflares*) exist as reconnection of small flux elements within loops [174, 216]. The net effect of these tiny unresolvable events provides an in-situ heating of the coronal plasma. On larger scales, *microflares*, of energies of about 10^{26} ergs or more, may involve reconnection between loops. These nanoflares and microflares reorganize the magnetic field within the loops. This chapter examines how a highly braided field responds to this reorganization using mathematical models. As such we hope to supplement numerical simulations of weakly braided line–tied fields (e.g. [189]).

The classic picture of solar activity set out by Parker [170, 172], Sturrock & Uchida [218], and others, describes a highly conducting plasma evolving quasi-statically due

to the random motions of the photospheric foot-points. Random rotations of the foot-points twist the field lines above, while a random walk of the foot-points braid the overlying loops about each other. The corona field finds an equilibrium state (i.e. state of minimum energy) given its topology, but must gradually adjust this equilibrium as the topology changes. In Parker's theory, smooth equilibria do not exist for sufficiently complex topologies, so electric current sheets form. There is some controversy as to whether (in ideal MHD) true current sheets of zero thickness form, rather than thin current layers [162]. The physical consequences for a finite conductivity plasma will be the same, however: resistive effects will change the field topology and release magnetic energy. Numerical [93] and theoretical evidence [65] strongly suggest that current layers of exponentially decreasing thickness will soon be produced when the magnetic field topology reaches even a small level of complexity. These current layers may either burn slowly as, say, a tearing mode, or burn quickly in a rapid reconnection event. Numerical simulations [61] suggest that rapid reconnection does not occur until sufficient stresses have built up in the magnetic field.

Delaying rapid reconnection allows the buildup of substantial energy reserves in the magnetic field. As the magnetic field becomes more and more braided and twisted, its energy will generally increase quadratically in time [28, 173]. If reconnection occurs too early, there will not be enough energy stored to power flares or coronal heating.

This classic picture has recently run into some difficulties. First, as will be discussed in the next section, present observations of loops do not clearly display a braided structure. Even if most of the braiding is at smaller scales, some braid structure might be expected to be visible at the sub-arcsecond resolutions of Trace and Stereo. Furthermore, random braiding of field lines within loops may expand the diameters of the loops beyond what we observe [92].

Secondly, the distribution of energy deposition along a loop is not easy to determine and remains controversial [8, 49, 176]. Some observations suggest that the deposition is largely at the base of the loops [7] while others suggest a uniform deposition along the loop [183]. If most of the deposition is at the base of the loop, then the predominant heating mechanism occurs at low heights, for example reconnection with field lines in the magnetic network or carpet [9, 184]. Note that coronal loops will only be observed if they contain a sufficient density of plasma, as emission scales with the square of the density. This plasma can be supplied in upflows from

the chromosphere. In chromospheric heating models the upflows are caused by heat deposition in the chromosphere or transition region. In nanoflare heating models energy is first released in the corona; this energy quickly spreads along the field lines down to the chromosphere, which then heats up and sends plasma upwards.

Several subsequent authors have presented self organized critical (SOC) models resembling forest fire models or avalanches [52, 147, 245, 257]. Most of these models involve a grid (2D or 3D) with magnetic field vectors at the nodes. At each time step, small perturbations are added to the field, in analogy with input of structure to the coronal field at the photosphere. The nodes become unstable if some criterion is satisfied, for example high field strength or high field gradients. In this case a small 'nanoflare' occurs, and the node shares some of its excess magnetic energy with neighbouring nodes. This spread of energy may make neighbouring nodes unstable, leading to more nanoflares. Thus a single small event can avalanche to a much larger set of events. In SOC models a grid set up in an arbitrary initial state will evolve due to both the input perturbations and the output events until a statistical steady state is reached. This 'critical' state has no intrinsic length scale (apart from the grid spacing on the smallest scale) and generally exhibits power law behaviour; in particular, the total energy released in a set of events obeys a power law distribution.

One great challenge of solar SOC theory is making a close correspondence with the specific geometry of the coronal magnetic field. The grid models do not explicitly possess a photospheric boundary. Also, one might wish to see coronal loops, or at least distinct flux regions bounded by separatrices [134].

Zirker and Cleveland [256] created an SOC model where the two dimensional grid represents a cross-section through a set of coronal flux tubes. They tuned the energy inputs and outputs according to what would be expected for a set of flux tubes undergoing twisting and braiding [28]. Longcope and Noonan [139] built a model based on the topological structure of the field. In particular, they relate the build up of stresses in a 2D grid to current flows along separatrices. Here we look at braided magnetic field evolving to an SOC state through reconnection.

The outline of this chapter is as follows. In section 6.2 we estimate the extent of braiding inside a coronal loop, assuming that most of the free energy stored in the loop results from braiding of flux elements. Section 6.3 briefly discusses whether braiding can be detected with present instruments. Section 6.4 reviews several mechanisms for generating braid structure within or between loops. Section 6.5 presents

an analytic model for the evolution of a loop where braiding is added by endpoint motions and removed by reconnection. Because the reconnection selectively occurs at critical points along the braid, the loop evolves to a self-organized state with a power law distribution of coherence lengths. The energy release distribution is also power law. Section 6.6 presents a numerical model involving a braiding pattern. An elastic force model shows that the stresses on the braided field are highest at certain places along the loop where the tangling is most complex. A numerical algebra routine is used to evolve the braid pattern according to additions to the braid at the endpoints and reconnection at the stress points. Finally, conclusions are presented in section 6.7. The result of this chapter is being submitted to astronomy and astrophysics journal.

6.2 The Amount of Braiding Inside Loops

As stated in chapter 4, when we look at a braid in projection, we see a certain number of crossings between the individual strings (for example the braid in figure 6.1(a) has 6 crossings) . Suppose a braid has N strings of diameter D and exhibits C crossings. If N is small, say $N = 3$ or $N = 4$, then each crossing will require two neighbouring strings to rotate around each other. If the strings are magnetic flux tubes, this means that the flux tubes must have a transverse magnetic field $B_\perp$, hence extra magnetic energy. Thus the magnetic energy increases with the number of crossings. We derived the inequalities relating magnetic energy to crossing number C in section 4.4 based on the work of Berger [30].

Here, we make a simple estimate of how the transverse field grows with C. Suppose the braided tubes stretch vertically between planes $z = 0$ and $z = L$. We ignore the contribution to the transverse field from the twisting of individual flux elements, i.e. we assume that the transverse field arises predominantly from braiding.

Each crossing involves two strings out of the N strings. Thus, on average, each string takes part in $2C/N$ crossings. This implies a single crossing takes place in a vertical distance of about

$$\delta z = \frac{NL}{2C}. \tag{6.1}$$

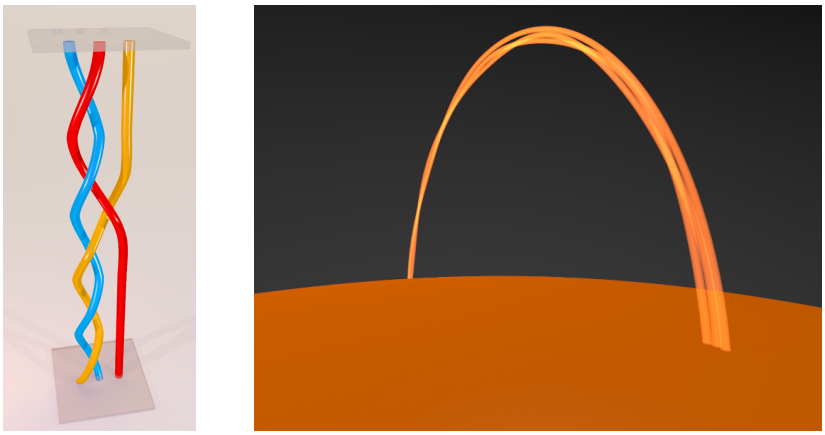

(a) (b)

Figure 6.1: (a) A braid with six crossings. (b) A cartoon of three coronal loops with the same braid structure.

Consider the centre lines of two tubes that rotate about each other between heights z and $z + \delta z$. Assuming the tubes have a circular horizontal cross-section, the transverse distance each tube travels is $\delta\ell = \pi D/2$. Then the typical ratio of transverse field strength to axial field strength will be

$$\frac{B_\perp}{B_\parallel} = \frac{\pi D}{2\delta z} \tag{6.2}$$

$$= \frac{\pi C D}{NL}. \tag{6.3}$$

Now $\tan^{-1} B_\perp/B_\parallel$ gives the typical angle of the flux tubes with respect to the vertical. Two crossing flux tubes will be misaligned by as much as twice this angle. When the crossing number becomes large enough, neighbouring tubes will be sufficiently misaligned to trigger reconnection [132]. If a misalignment of about $\pi/6$ triggers reconnection, then $B_\perp/B_\parallel \approx \tan \pi/12 \approx 0.27$, and the crossing number will be

$$C_{critical} = \frac{NL}{\pi D} \tan \pi/12 \approx 0.085 \frac{NL}{D}. \tag{6.4}$$

For flux elements with aspect ratio $L/D = 100$ and $N = 3$, we find $C_{\mathrm{critical}} \approx 25$.

We also note that the free energy is proportional to the square of the crossing number. Let

$$E_{free} = \frac{1}{2\mu} \int B_\perp^2 \, \mathrm{d}^3 x. \tag{6.5}$$

The volume of the N tubes is approximately $N\pi D^2 L$. Then by equation (6.3)

$$E_{free} \approx \left(\frac{N\pi D^2 L}{2\mu} \right) \left(\frac{\pi C D B_\parallel}{NL} \right)^2 = \left(\frac{\pi^3 D^4 B_\parallel^2}{2\mu NL} \right) C^2. \tag{6.6}$$

6.3 Observation of Braided Coronal Loops

Observations of coronal loops, like the famous Hinode image (figure 6.2), display a well-combed set of almost parallel loops. The observed structure seems far away from mathematical diagrams of braids, such as 6.1(a). The mathematical diagrams, however, are designed to most clearly display the geometrical structure. If we elongate, compress, and arch the strings in the braid diagram, then the braid structure becomes much more difficult to see. Figure 6.1(b) demonstrates this. One can see that a braid with, say, 6 crossings might be difficult to distinguish from a collection of slightly irregular but parallel loops. Detailed forward modelling would be likely to further obscure the braid structure. For example, figure 6.1(b) shows tubes with circular cross sections. Three circular tubes bundled together, as in the diagram, have an empty space in between while physical magnetic flux tubes will expand into the space between (consider a cross-section of three neighbouring loops. If the loops are modelled with circular cross sections, then we obtain three close-packed circles in a plane; they can only touch each other at three points. But in cross section three more realistic flux elements might resemble one big circle divided into three pie slices).

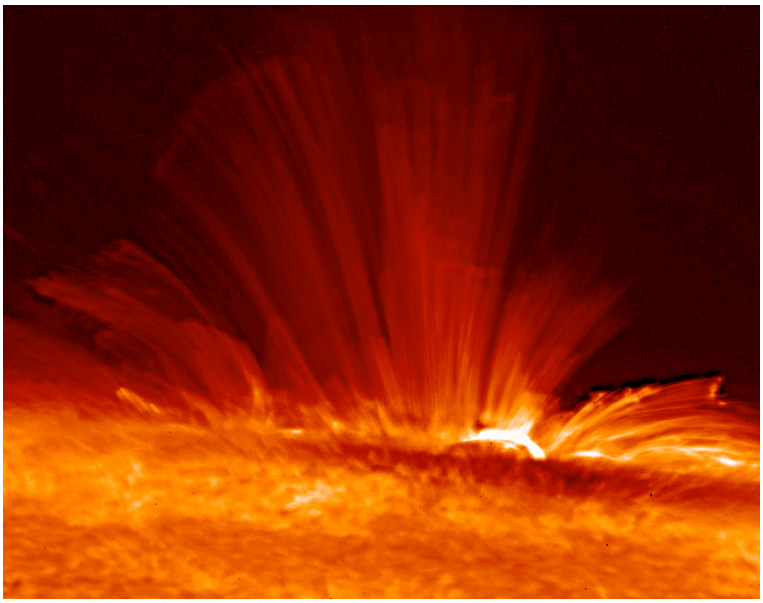

Figure 6.2: Magnetic loops observed by Hinode. JAXA/NASA.

The possibility of directly observing braiding also depends on details of the braid structure. As described in details in chapter 4, a braid in mathematics is a set of curves stretched between two planes. The simplest non-trivial braid consists of two curves twisted about each other. Suppose the number of twists between curves 1 and 2 is $\mathcal{T}_{12}$ (we adopt the convention that one turn through an angle 2π corresponds to

$\mathcal{T}_{12} = 1$). Two magnetic flux tubes braided in this fashion will also possess internal twists $\mathcal{T}_1$ and $\mathcal{T}_2$ (we will assume uniform internal twists here). Of course, if we are looking at two neighbouring coronal loops or two threads in an erupting prominence then the large-scale structure represented by $\mathcal{T}_{12}$ will be easier to see than the smaller scale twists. Suppose, however, that the two tubes are tightly wound about each other. In this case, they might appear as a single tube. In the particular case where $\mathcal{T}_1 = \mathcal{T}_2 = \mathcal{T}_{12} = \mathcal{T}$, the two flux tubes will be topologically identical to a single tube with uniform twist $\mathcal{T}$. If the internal and external twists differ from each other, then current sheets will develop between the two tubes. This will lead to reconnection. If that reconnection is not too fast, then the two tubes may persist as topologically distinct entities. However, both tubes will light up due to emission caused by the reconnection, so in practical terms they may still be indistinguishable from one single tube.

Suppose that the braid is generated by random rotational motions at the photosphere. As it was shown in section 4.4.1, if the average rotation is zero, then the mean twist vanishes, but there will be a root-mean-square twist growing in time as $t^{1/2}$ [28, 218].

With three or more curves, there are many more possible braid patterns. Rather than merely recording the twist between each pair of curves, we must record the actual sequence of windings. We can measure the complexity of the braid by counting the number of crossings C exhibited when the curves are projected onto the $x - y$ plane. In this case random motions do not generally cancel each other out. In particular, if the braid is generated by random photospheric motions, then C will grow linearly with time, and the resulting magnetic energy will grow quadratically in time [30, 173]. Eventually the corona reaches a critical state where it cannot take any more braiding, and reconnection removes crossings at the same rate as they are generated at the photosphere.

However, not all braided fields will look the same, even if the number of curves N and the number of crossings C are the same. Figure 6.3 shows two braid structures which both have four strings and 13 crossings. Some descriptive terminology will be useful here. The sections of the braid where the two strings on the left twist about each other will be called *coherent sequences*. The single crossings which swap the middle string with the string on the right will be called *interchanges*. The second structure (figure 6.3(b)), however, is much more coherent. Apart from the crossing in the middle, the braid consists of two distinct pairs of twisting tubes. Such a braid

pattern would look well combed in comparison to the randomly tangled pattern of figure 6.3(a).

In this chapter we suggest that self-organization will add coherence to the braid pattern. This additional coherence has some practical consequences for any attempt to observe coronal braiding. First, the interchanges may be a signature of braiding. If the two tubes twisting about each other appear like one larger tube, then at the interchange this larger tube will appear to branch and/or merge with a neighbouring tube. Secondly, a coherent braid pattern may not spread out as much in radius as a random pattern. Galloway, Helander, and MacKinnon [92] suggest that limits can be placed on braiding of threads within an X-ray loop because randomly braided field lines will random walk perpendicular to the axis of the loop. As a consequence the loop spreads out laterally as it rises from the photosphere. However, a more well-combed braid pattern within a loop will not spread out as much.

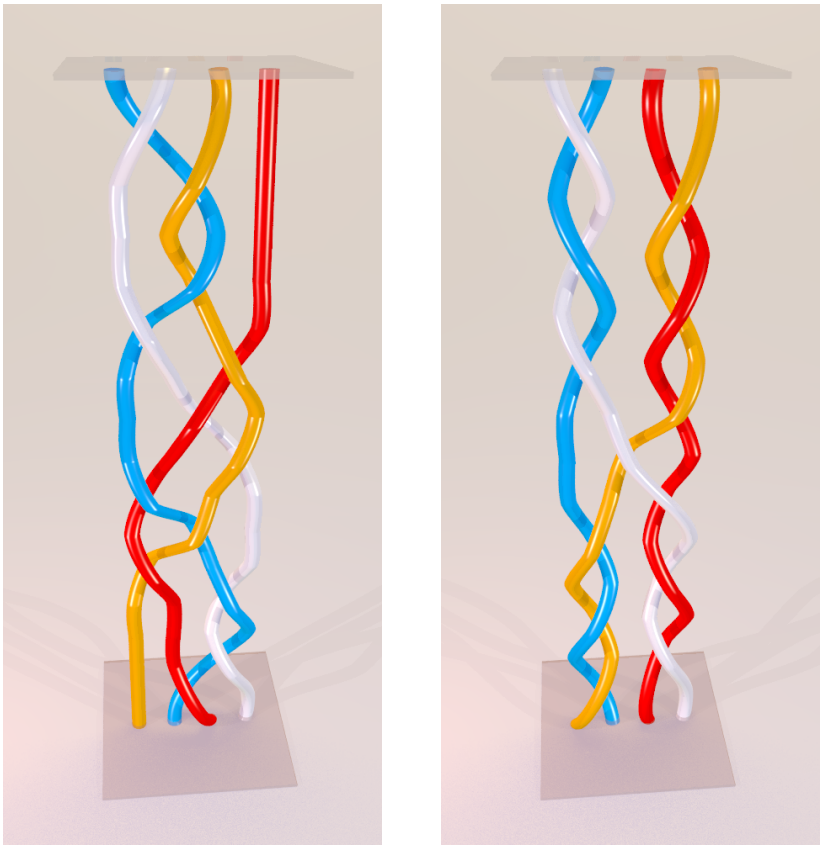

(a) (b)

Figure 6.3: (a) A random 4-braid with 13 crossings. (b) A highly coherent four braid with 13 crossings. Here there are two *coherent sequences* where only pairs of curves twist about each other, separated by an *interchange* in the middle.

6.4 Generation of Braid Structure

There are several mechanisms which will braid coronal magnetic flux. First, random motions of photospheric magnetic foot-points will braid the flux elements above. Secondly, a coronal flux tube may be fragmented at its foot-points. Imagine that part of a foot-point rotates, twisting the flux above. Then the fragments at the foot-point rearrange themselves, and subsequently another part rotates. Even if the second rotation is opposite in sense to the first, the twists generated in the magnetic field do not cancel. The non-cancellation makes random photospheric rotations much more efficient in heating the coronal plasma [31].

Third, the fragmentation of the foot-points of large coronal loops can be interpreted in terms of the coronal flux connecting to small-scale chromospheric loops. These loops can reconnect with each other, leading to an effective motion of the end-points of the coronal field lines [184]. Evidence for fragmentation and reconnection near foot-points of coronal loops can be seen in the work of Shibata et al. [209].

Fourth, Reconnection may occur on several scales. Suppose two large bundles of flux reconnect. This has two effects on the smaller flux elements inside. First, their small-scale braid patterns are cut in half and reshuffled. Symbolically, if large tube 1 has an internal braid pattern A below the reconnection point and braid pattern B above, and tube 2 has patterns C below and D above, then after reconnection the new tubes will have patterns AD and BC. In addition, when two flux tubes reconnect, each acquires a half unit of twist [24, 211, 249]. Thus the smaller flux elements inside will now twist about each other, adding to the braid patterns additional structure. (Symbolically, if a half twist is represented by the Greek letter Δ, then the final patterns are in fact ΔAD and ΔBC.)

Fifth, reconnection is not always clean and simple. For example, if two tubes with five units and seven units of flux reconnect, then there will be two units of flux left over in a topologically distinct third tube. Moreover, if there are multiple reconnection sites, then the end product may be several topologically distinct tubes.

Finally, internal braiding may already be present in newly emerging flux.

6.5 Analytic Braid Model Exhibiting Self-Organization

6.5.1 Description of the Model

Here we present a simple model which gives a power law distribution of energy releases. We consider a braid on three strings, with lower boundary fixed (figure 6.4). At the upper boundary, braid structure is generated in the strings below by a succession of motions. We suppose at the boundaries the endpoints line up on the x axis.

In this model, two motions alternate with each other. The first motion rotates the leftmost and middle endpoints through some net twist angle ϕ, where ϕ is a multiple of π. This generates a twist $\mathcal{T}$ corresponding to $C = 2\mathcal{T}$ crossings in the strings below, i.e. $C = \phi/\pi$. The sign of C tells us whether the crossing is right-handed or left-handed. The second motion gives a single half twist between the middle and right hand end point.

In figure 6.4(a), there are two coherent sequences with twists 3/2 and -3/2, i.e. $C = +3$ and $C = -3$. Note, however, that the twists cannot cancel because of the interchange. This constraint can only be removed by reconnection. Figure 6.4(b) shows the result immediately after reconnection of the curves at the interchange. Now the positive and negative twists connect to each other. They can now cancel out through purely ideal motions.

The braid on the left can be generated as follows: start with three straight curves of figure 6.4(c). First, let the leftmost endpoints rotate through three anti-clockwise half turns ($C = +3$), giving the strings below three positive (right-handed) half twists. Next, the second motion exchanges the third string with the middle string. Finally, a twist of three clockwise turns gives the two strings on the left (no longer the same two strings) three negative half-twists ($C = -3$).

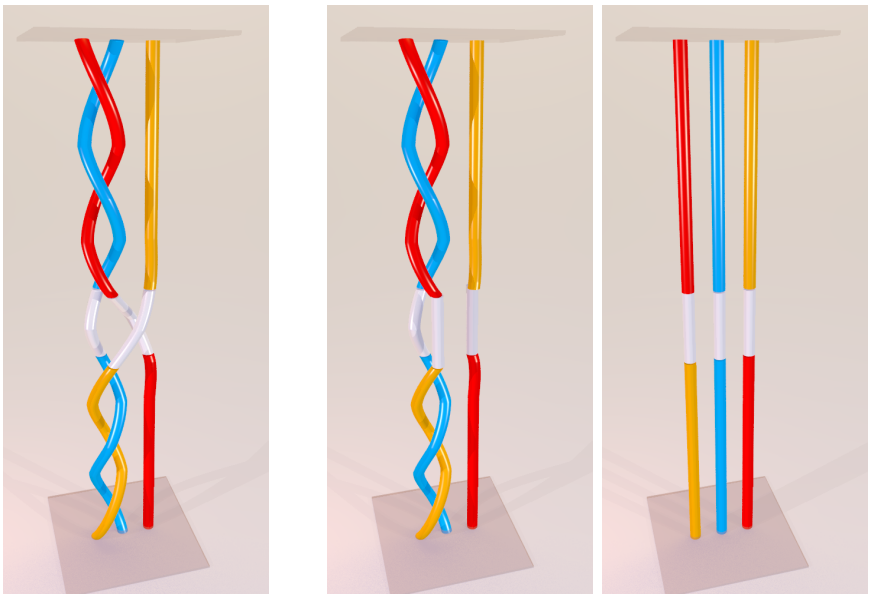

(a) (b) (c)

Figure 6.4: (a) A 3-braid with two coherent sequences separated by an interchange. (b) Reconnection removes the interchange. (c) The curves can now relax, cancelling out their crossings.

6.5.2 The Distribution of Twists

Suppose the braid as a whole has M sequences separated by $M-1$ interchanges. The number of sequences with crossing number C is $n(C)$. Thus

$$M = \sum_{C=-\infty}^{\infty} n(C). \tag{6.7}$$

Also, the total number of crossings (ignoring the sign and the interchange) is

$$C_{\text{tot}} = \sum_{C=-\infty}^{\infty} |C| n(C). \tag{6.8}$$

We will simplify the calculation by assuming C is a continuous rather than discrete variable. In this case, the number of crossings between C and $C+\delta C$ is (considered as an ensemble average) $n(C)\delta C$. We will normalize by letting $f(C)\delta C = n(C)/M$. Thus

$$\int_{-\infty}^{\infty} f(C)\mathrm{d}C = 1. \tag{6.9}$$

At each time step, one new sequence and one new interchange is added, while reconnection removes one of the interior interchanges. The crossing number of the next sequence is distributed with probability function $f(C)$. At each time-step the function $f(C)$ changes by $\delta f(C)$: first, there is a probability of $p(C)$ that the

new sequence will add to $f(C)$. Next, the sequence to the left of the reconnecting obstruction may have twist C. This sequence disappears, so there is a probability $f(C)$ that the number $Mf(C)$ of sequences with crossing number C will decrease by one. Similarly, the sequence to the right of the obstruction has probability of $f(C)$ of removing a C-sequence. Finally, if the left sequence has crossing number w and the right sequence has crossing number $C - w$, a new C-sequence will be created. Thus

$$\begin{aligned} M\delta f(C) &= p(C) - 2f(C) \\ &+ \int_{-\infty}^{\infty} f(w)\mathrm{d}w \int_{-\infty}^{\infty} f(u)\mathrm{d}(u)\delta(C-(u+w)) \qquad (6.10) \\ &= p(C) - 2f(C) + \int_{-\infty}^{\infty} f(w)f(C-w)\mathrm{d}w. \qquad (6.11) \end{aligned}$$

In a steady state, the left–hand side vanishes. Thus

$$p(C) - 2f(C) + \sqrt{2\pi}(f * f)(C) = 0, \qquad (6.12)$$

where $f * g$ is the Fourier convolution. To solve this, we take the Fourier transform,

$$\tilde{f}^2(k) - 2\ \tilde{f}(k) + \tilde{p}(k) = 0. \qquad (6.13)$$

This has solution

$$\tilde{f}(k) = \left(1 \pm \sqrt{1 - \tilde{p}(k)}\right). \qquad (6.14)$$

Note that we must choose the negative square root in order to insure that $\tilde{f}(k) \to 0$ as $k \to \infty$.

Say the input is a Poisson process, so that for some λ,

$$p(C) = \frac{\lambda}{2} e^{-\lambda|C|}. \qquad (6.15)$$

Then

$$\begin{aligned} \tilde{p}(k) &= \frac{\lambda^2}{\lambda^2 + k^2}, \qquad (6.16) \\ \tilde{f}(k) &= \left(1 - \frac{|k|}{\sqrt{\lambda^2 + k^2}}\right). \qquad (6.17) \end{aligned}$$

We can solve the inverse transform using standard integrals:

$$f(C) = \frac{\lambda}{2}\left(I_1(\lambda C) - L_{-1}(\lambda C)\right). \qquad (6.18)$$

where I_0 is a Bessel–I function and L_0 is a Struve–L function (see figure 6.5). The function $f(C)$ falls asymptotically as C^{-2}.

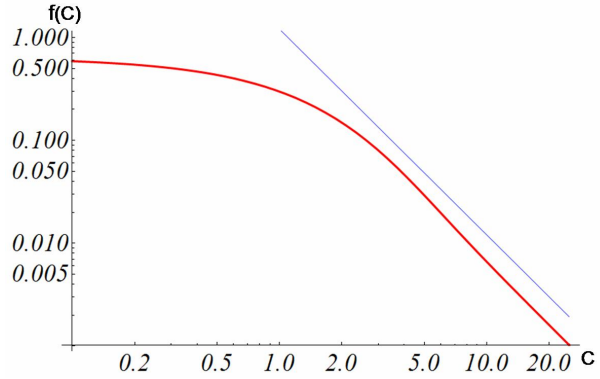

Figure 6.5: The distribution $f(C)$ of braid sequence lengths given by equation (6.18), shown with a log-log plot. The asymptotic slope is -2.

6.5.3 The Energy Distribution

From section 6.2, the free energy of a set of braided magnetic flux tubes is $E_{free} = a\,C^2$ where the constant a depends on the length and diameter of the tubes. Suppose that a reconnection reduces the number of crossings from $C_{initial}$ to C_{final}. We ignore the constant a and define the 'flare energy' to be

$$W = \delta E/a = C_{initial}^2 - C_{final}^2. \tag{6.19}$$

Given the distribution $f(C)$ of coherent braid sequences, what is the corresponding distribution of flare energies $f(W)$?

We first consider a braid consisting of just two sequences separated by an interchange, as in figure 6.4(a). Suppose the sequences have size (number of crossings) C_1 and C_2. After the sequences merge, they form one sequence of size $C_1 + C_2$. If C_1 and C_2 have opposite signs, once they merge they release energy.

For large crossing numbers C_1 and C_2, we can ignore the energy release due to the loss of the interchange. The change in energy is $W = 4\,|C_1 C_2|$.

To obtain the distribution of flare energy, we integrate over all combinations of C_1 and C_2 (with their corresponding probabilities $f(C_1)$ and $f(C_2)$, but insert a delta function to pick out the combinations which yield the correct energy change W:

$$f(W) = \int\int f(C_1)\, f(C_2)\, \delta(W - 4C_1C_2)\, \mathrm{d}C_1\, \mathrm{d}C_2. \tag{6.20}$$

Thus

$$f(W) = \int \frac{1}{4C_1}\, f(C_1)\, f\left(\frac{W}{4C_1}\right) \mathrm{d}C_1. \tag{6.21}$$

For a power law distribution of crossings, i.e. $f(C_1) = b\,C_1^{-\alpha}$, using the energy

distribution relation (6.21), we have

$$\begin{aligned} f(W) &= \frac{1}{4}\int_{C_{min}}^{C_{max}} \frac{1}{C_1}\, b\, C_1^{-\alpha}\, b \left(\frac{W}{4C_1}\right)^{-\alpha} \mathrm{d}C_1 \\ &= \frac{b^2}{4}\int_{C_{min}}^{C_{max}} (4)^{\alpha} W^{-\alpha}\, \frac{\mathrm{d}C_1}{C_1} \\ &= b^2 (2)^{2\alpha-2} W^{-\alpha} \int_{C_{min}}^{C_{max}} \frac{\mathrm{d}C_1}{C_1} \\ &= b^2 (2)^{2\alpha-2} W^{-\alpha} \ln \frac{C_{max}}{C_{min}}. \end{aligned} \tag{6.22}$$

Thus $f(W) \propto W^{-\alpha}$ for large W. The distribution could be modified for smaller W where the energy of the interchange cannot be neglected. The unit of crossing corresponding to the interchange gives an effective length scale to the problem, which modifies the power law behaviour at low W.

Next we calculate the energy distribution assuming that reconnection occurs when the total crossing number reaches some critical value C_{crit}. Here two coherent sequences of length C_1 and C_2 merge. Suppose that $|C_2| > |C_1|$ and that they are of opposite sign. They merge to form a single sequence of length $|C_2| - |C_1|$. As we had two sequences of total length $|C_2| + |C_1|$ beforehand, the loss of crossings is $2|C_1|$. The change in crossing number squared is

$$W = C_{\mathrm{crit}}^2 - (C_{\mathrm{crit}} - 2|C_1|)^2 = 4C_{\mathrm{crit}}|C_1| - 4C_1^2. \tag{6.23}$$

To find the slope of the distribution of W for high W, we assume $C_1 \ll C_{\mathrm{crit}}$ and we choose C_1 to be positive, and multiply $f(W)$ by 2. There is a constraint here: the second sequence has a larger crossing number, i.e. $|C_2| > |C_1|$. Thus the probability of obtaining W is

$$f(W) = 2\int_0^{\infty}\int_{-\infty}^{-C_1} f(C_1)\, f(C_2)\, \delta(W - 4C_1 C_{\mathrm{crit}})\, \mathrm{d}C_2\, \mathrm{d}C_1. \tag{6.24}$$

For a power law distribution of crossings, we let $f(C) = b|C|^{-\alpha}$ for $C \geq 1$. Then

$$f(W) = 2b^2 \int_1^{\infty} C_1^{-\alpha} \frac{C_1^{1-\alpha}}{1-\alpha}\, \delta(W - 4C_1 C_{\mathrm{crit}})\, \mathrm{d}C_1 \tag{6.25}$$

$$= \left(\frac{2b^2}{1-\alpha}\left(\frac{1}{4C_{crit}}\right)^{2-2\alpha}\right) W^{1-2\alpha}. \tag{6.26}$$

Thus $f(W) \propto W^{1-2\alpha}$. For example, if $\alpha = 2$ as in the model of the previous section, then the distribution of flares with energy W decreases as the third power of W, i.e. $f(W) \propto W^{-3}$.

6.6 Numerical Models

6.6.1 The Braid Group

The theory of braids was first developed by Artin [6]. Figure 6.6 shows the elementary braid patterns for a braid consisting of three strings. Each pattern is labelled according to which strings are involved in a crossing. Thus σ_1 refers to a crossing of string 1 under string 2 (as numbered from left to right at the top), σ_2 refers to string 2 crossing under string 3, etc. The inverse crossing σ_1^{-1} refers to string 1 crossing over string 2. An algebraic n-braid is a word over the generators of the braid group B_n, that is the set $\sigma_i^{\pm 1}$ for $1 \leq i < n$. Two words in B_n represent the same braid if, and only if, one can be transformed into the other using the following relations:

$$\sigma_i \sigma_i^{-1} = e, \tag{6.27}$$

$$\sigma_i \sigma_j = \sigma_j \sigma_i, \tag{6.28}$$

$$\sigma_i \sigma_{i+1} \sigma_i = \sigma_{i+1} \sigma_i \sigma_{i+1}, \tag{6.29}$$

where $|i - j| > 1$ and e is the identity in B_n (topologically e is the braid with no crossings; it consists of n vertical strings). The word length for Artin braids equals the number of crossings in the braid.

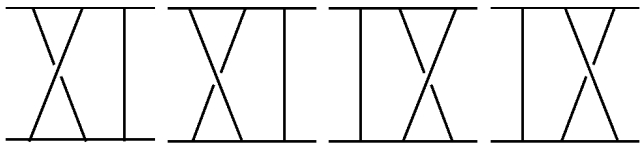

(a) σ_1 (b) σ_1^{-1} (c) σ_2 (d) σ_2^{-1}

Figure 6.6: The braid group for three strings.

The diagram in figure 6.7 shows a projection of the braid into a plane. The strings may be regarded as beginning and ending each crossing by aligning themselves parallel to the x-axis, and deviating in the y direction only to move around each other. Other projections are also possible, for example onto a cylinder [26].

Let us consider three-braids in particular. The special braid pattern

$$\Delta = \sigma_1 \sigma_2 \sigma_1 = \sigma_2 \sigma_1 \sigma_2 \tag{6.30}$$

twists the entire braid through half a turn. The square of this, Δ^2 gives a full turn, and commutes with all other braid words in the group (in group theory terminology,

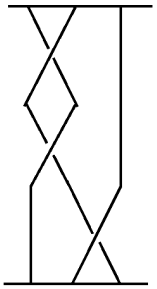

Figure 6.7: The braid word representing this braid is $\sigma_2\sigma_1\sigma_1$.

powers of Δ^2 constitute the *centre* of the braid group). Half turns *almost* commute with other group elements, in the sense that

$$\Delta\sigma_1 = \sigma_2\Delta; \Delta\sigma_2 = \sigma_1\Delta. \tag{6.31}$$

Because the full turns commute with other braid patterns, they can be placed anywhere along the braid. All three braids can be converted to the normal form

$$B = \Delta^n \sigma_1^a \sigma_2^{-b} \sigma_1^c \sigma_2^{-d}. \tag{6.32}$$

6.6.2 Selective Reconnection

A crucial element of our self-organization model is the hypothesis that reconnection will occur preferentially at certain places along the braid. In other words, a magnetic braid will have weak points where the stresses are largest, and reconnection is most likely to be triggered.

Figure 6.8 shows a fairly coherent braid pattern. In this braid, two coherent segments are stacked on top of each other. This braid could be generated by a rotational motion at one boundary of one pair of tubes, and at the other boundary by a rotational motion entangling a different pair of tubes. Alternatively, if the motions are at just the lower boundary, the motions could be an anti-clockwise motion of two of the endpoints followed by a clockwise motion with a different pair. The Artin representation for the braid is

$$\mathbf{B} = \sigma_2^{-4}\,\sigma_1^4. \tag{6.33}$$

Starting with a set of braided strings with this topology, we employed an elastic relaxation code [16] to relax the braid to its lowest energy state (shown in figure 6.8(a)). The code balances curvature forces and pressure forces between the strings. We hypothesize that the most likely place where the reconnection occurs is where the balanced forces are the strongest. In figure 6.8 the position of the reconnection

point is indicated by an arrow. Note that this is precisely where the braid pattern changes. We assume that the stresses will cause the two outside strings (red and yellow) to reconnect. The result of relaxing the resulting braid further is shown in figure 6.8(c)).

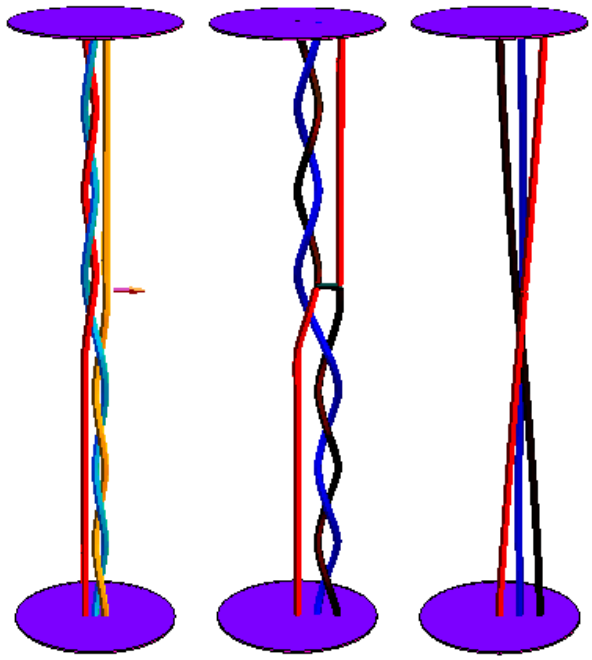

(a) (b) (c)

Figure 6.8: In figure (a) the braid has been relaxed so that the pressure force between the strings balances the curvature forces. The arrow points to the region of maximum stress. Figure (b) shows the structure of the braid right after a reconnection has been made. In figure (c), the relaxation code has again been used to reach a new minimum energy state.

6.6.3 Algebraic Simulation

We run simulations of braids undergoing both random input of crossings at the boundary planes, plus random reconnections in between sequences. We find that initially random braids evolve into a self-critical power law state. Figure 6.9 shows that the frequency distribution of the sequence size becomes a power law. In this case, we consider a braid word with size 358 and 1000 reconnections with 500 runs. This is a power law fit with exponent -3.06.

In figure 6.10 we demonstrate the power law fit for braid size 400 with 1000 reconnections and different number of runs. And figure 6.11 shows the power law fit for braid size 400 with 2000 reconnections.

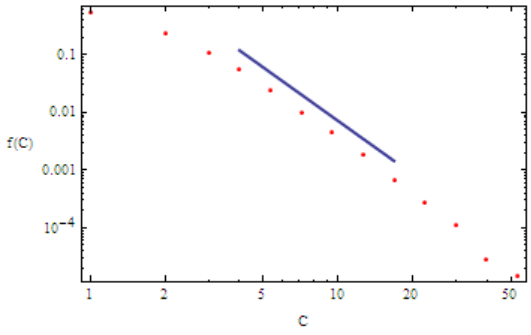

Figure 6.9: For braid size 358 with 1000 reconnections the distribution is a power law. The power law exponent is -3.06.

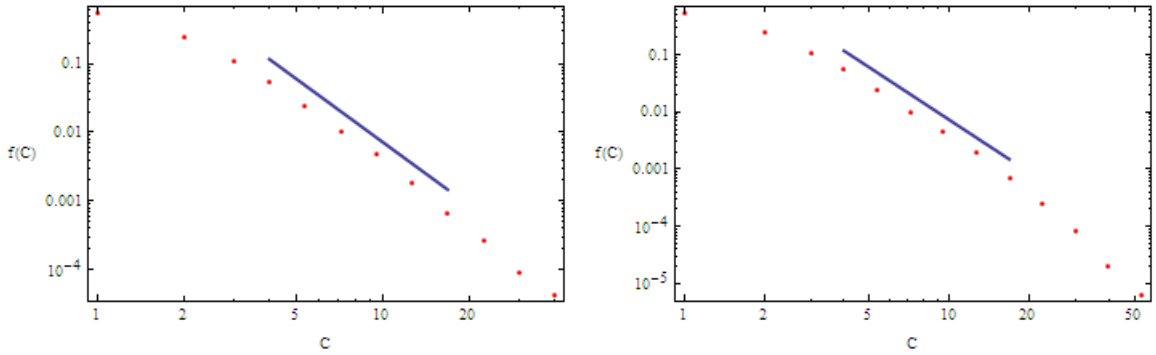

(a) Size = 400, reconnections = 1000, runs = 200 (b) Size = 400, reconnections = 1000, runs = 1000

Figure 6.10: Here we increase the braid size from 358 (figure 6.9) to 400, the distribution is a power law. (a) The power law exponent is -3.03. (b) The number of runs is increased from 200 (figure 6.10(a)) to 1000 (figure 6.10(b)) where the power law exponent is -3.02. The increase in the number of runs provides a better statistics.

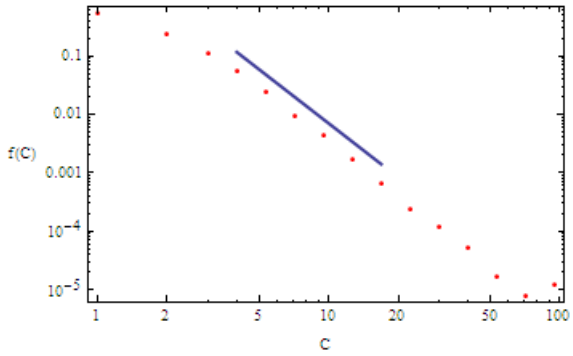

(a) Size = 400, reconnections = 2000, runs = 1000

Figure 6.11: The power law exponent for a braid with 400 crossings and 2000 reconnections is -3.06. The increase in the number of reconnections provides more opportunity for strings to relax to a critical state.

Figures 6.12 and 6.13 demonstrate the power law distribution of the braid sequence and energy release when the braid size is 400 with 1000 reconnections taking place.

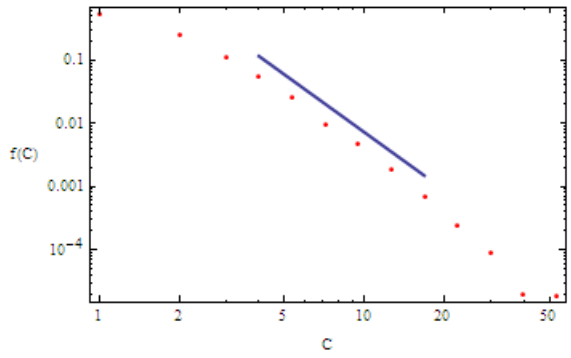

(a) Size = 400, reconnections = 1000, runs = 500

Figure 6.12: The power law exponent for a braid with 400 crossings and 1000 reconnections is -3.02.

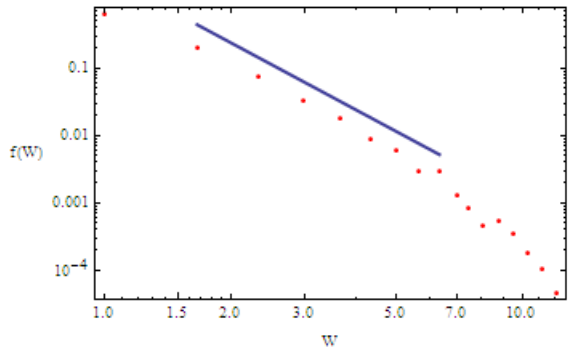

(a) Size = 400, reconnections = 1000, runs = 500

Figure 6.13: The distribution of energy releases. The best power law fit gives a slope of -3.32.

6.7 Conclusions

In this chapter, using braid theory, we have modelled coronal loops as collections of braided strings with large numbers of crossings. Reconnections simplify the braid structure while new crossings are introduced at the boundaries. We showed that the resulting solar flare distribution is a power law.

Our model is similar to a one dimensional forest fire model. It differs significantly from avalanche models since in avalanche models a small reconnection triggers more reconnection; this triggering has not been included in our model. The braid structure in our model is a self-organized critical state. Avalanche models attain a particular slope while our braid model attains a particular structure. Most of the self-organized critical models applied to solar physics bear relatively little resemblance to solar coronal structure. Our model is designed to reflect both input of structure at the photosphere and release of structure during reconnection.

The braid model certainly warrants more investigation since there is agreement between the theoretical results presented by others and our results. Also, using our model one can perhaps make testable predictions which can lead to a better understanding of energy release and flare distribution size. To expand our model, one way is allowing reconnection to trigger more reconnection, in fact making our model similar to avalanche models.

Appendix A

In order to introduce the energy budget, we first introduce a few technical results. The low-pass filtering operator is defined by

$$P_K : \qquad f(\mathbf{r}) \to f_K^<(\mathbf{r}), \tag{A.1}$$

and this operator sets to zero all Fourier components with wave-number greater than K. Some of the properties of P_K are as follows:
1. P_K is a projector, $P_K^2 = P_K$.
2. P_K commutes with ∇ and ∇^2. Also, P_K is self-adjoint for the L^2 inner product, where for all real periodic functions f and g ,

$$\langle f P_K g\rangle = \langle (P_K f) g\rangle = \sum_{k\le K} \hat{f}_k \hat{g}_{-k}. \tag{A.2}$$

3. High and low-pass filtered functions with the same cut-off wave-number K are orthogonal :

$$\langle f_K^> g_K^<\rangle = 0. \tag{A.3}$$

Relation 1 follows from the Fourier decompositions of f, ∇f and $\nabla^2 f$:

$$f = \sum_k \hat{f}_k\, e^{\mathrm{i}\mathbf{k}\cdot\mathbf{r}}, \qquad \nabla f = \sum_k (\mathrm{i}\mathbf{k})\hat{f}_{\mathrm{k}}\, \mathrm{e}^{\mathrm{i}\mathbf{k}\cdot\mathbf{r}}, \qquad \nabla^2 f = \sum_{\mathrm{k}} (-\mathrm{k}^2)\hat{f}_{\mathrm{k}}\, \mathrm{e}^{\mathrm{i}\mathbf{k}\cdot\mathbf{r}}. \tag{A.4}$$

Relations 2 and 3 are consequences of Parseval's identity:

$$\langle f g\rangle = \sum_k \hat{f}_k \hat{g}_{-k}. \tag{A.5}$$

To apply the above definitions to the Navier-Stokes equations, let us write them in a slightly more general form, including a forcing term:

$$\partial_t \mathbf{v} + \mathbf{v}\cdot\nabla\mathbf{v} = -\nabla p + \nu\nabla^2\mathbf{v} + \mathbf{f}, \tag{A.6}$$

$$\nabla\cdot\mathbf{v} = 0. \tag{A.7}$$

The force $\mathbf{f}$ is assumed to be periodic in the space variable. Also it may depend on the time and the velocity. Applying P_K to (A.6), using (1.37) and relation 1, we obtain

$$\begin{aligned} \partial_t \mathbf{v}_K^< + P_K(\mathbf{v}_K^< + \mathbf{v}_K^>) \cdot \nabla(\mathbf{v}_K^< + \mathbf{v}_K^>) &= -\nabla p_K^< + \nu \nabla^2 \mathbf{v}_K^< + \mathbf{f}_K^<, \\ \nabla \cdot \mathbf{v}_K^< &= 0. \end{aligned} \tag{A.8}$$

Now taking the scalar product of (A.8) with $\mathbf{v}_K^<$, averaging and using relations 1, 2 and 3, we obtain an energy budget of the low pass filtered velocity:

$$\begin{aligned} \partial_t \left\langle \frac{|\mathbf{v}_K^<|^2}{2} \right\rangle &+ \langle \mathbf{v}_K^< \cdot [(\mathbf{v}_K^< + \mathbf{v}_K^>) \cdot \nabla(\mathbf{v}_K^< + \mathbf{v}_K^>)] \rangle \\ &= -\langle \mathbf{v}_K^< \cdot \nabla p_K^< \rangle + \nu \left\langle \mathbf{v}^< \cdot \nabla^2 \mathbf{v}_K^< \right\rangle + \langle \mathbf{v}_K^< \cdot f_K^< \rangle . \end{aligned} \tag{A.9}$$

The above equation can be simplified using some of the transformations used in section 1.2.2. For instance, $\langle \mathbf{v}^< \cdot \nabla p_K^< \rangle = 0$ and $\nu \langle \mathbf{v}_K^< \cdot \nabla^2 \mathbf{v}_K^< \rangle = -\nu \left\langle |\omega_K^<|^2 \right\rangle$. The main difference is that now the contribution from the non-linear term in the Navier-Stokes equations does not vanish. When this term is expanded, it produces four terms, of which two are identically vanishing:

$$\langle \mathbf{v}_K^< \cdot (\mathbf{v}_K^< \cdot \nabla \mathbf{v}_K^<) \rangle = \langle \mathbf{v}_K^< \cdot (\mathbf{v}_K^> \cdot \nabla \mathbf{v}_K^<) \rangle = 0. \tag{A.10}$$

Equation (A.10) can be proved using incompressibility, equation (1.21) and equation (1.22). The vanishing of the leftmost side means that interactions among 'lesser' scales can not change the energy content of the lessers. Also, the vanishing of the middle term means that advection of lessers by greaters does not change the energy content of the lessers. After collecting the remaining terms from (A.9), we write the scale-by-scale energy budget equation as:

$$\partial_t \zeta_K + \Pi_K = -2\nu \, \Omega_K + \mathcal{F}_K, \tag{A.11}$$

where the cumulative energy between wave-number 0 and K is

$$\zeta_K \equiv \frac{1}{2} \left\langle |\mathbf{v}_K^<|^2 \right\rangle = \frac{1}{2} \sum_{k \le K} |\hat{\mathbf{v}}_k|^2 , \tag{A.12}$$

and the cumulative enstrophy is:

$$\Omega_K \equiv \frac{1}{2} \left\langle |\omega_K^<|^2 \right\rangle = \frac{1}{2} \sum_{k \le K} k^2 \, |\hat{\mathbf{v}}_k|^2 . \tag{A.13}$$

The cumulative energy injection (by the force) is:

$$\mathcal{F}_K \equiv \left\langle \mathbf{f}_K^< \cdot \mathbf{v}_K^< \right\rangle = \sum_{k \le K} \hat{\mathbf{f}}_k \cdot \hat{\mathbf{v}}_{-k}, \tag{A.14}$$

and the energy flux at wave-number K is:

$$\Pi_K \equiv \langle \mathbf{v}_K^< \cdot (\mathbf{v}_K^< \cdot \nabla \mathbf{v}_K^>) \rangle + \langle \mathbf{v}_K^< \cdot (\mathbf{v}_K^> \cdot \nabla \mathbf{v}_K^>) \rangle \,. \tag{A.15}$$

Equation (A.11) is interpreted as follows: the rate of change of the energy at scales down to $l = K^{-1}$ is equal to the energy injected at such scales by the force $\mathcal{F}_K$ minus the energy dissipated at such scales ($2\nu\,\Omega_K$) minus the flux of energy (Π_K) to smaller scales due to non-linear interactions. At high Reynolds numbers it is typical to have the energy injection confined to large-scales ($O(l_0)$) and the energy dissipation confined to small-scales ($O(l_d)$) with $l_d \ll l_0$.

It is traditional in turbulence theory to derive an energy budget equation in Fourier space under the assumptions of statistical homogeneity and isotropy. Since the scale-by-scale energy budget equation derived above makes no use of probabilistic tools, it is therefore applicable to a much wider range of situations [88].

Appendix B

A random function is a family of random variables that depend on one or several space or time variables. A random function $v(t, \varpi)$ is G_t-stationary if for all t and ϖ

$$v(t + h, \varpi) = v(t, G_h\varpi), \qquad \forall h \geq 0, \tag{B.1}$$

where the time-shift G_t is the map $G_t : \varpi \longmapsto \mathbf{v}(t)$. It also maps $\mathbf{v}(s)$ into $\mathbf{v}(s+t)$.

The most common practical method for analysing a stationary random function is to determine its power spectrum. Here, we introduce a definition of the power spectrum. Let $v(t, \varpi)$ be a centred and stationary random function and its Fourier variable denoted by f. We therefore have

$$v(t, \varpi) = \int_R e^{\mathrm{i}ft}\hat{v}(f, \varpi)\mathrm{d}f, \tag{B.2}$$

$$v_F^<(t, \varpi) = \int_{|f|\leq F} e^{\mathrm{i}ft}\hat{v}(f, \varpi)\mathrm{d}f, \quad F \geq 0, \tag{B.3}$$

where averages of $v_F^<(t, \varpi)$ are stationary. The Fourier transforms of homogeneous random functions are random distributions, so $\hat{v}(f, \varpi)$ is not an ordinary function of f, although $v_F^<(t, \varpi)$ is an ordinary function of t.

The cumulative energy spectrum is defined as

$$\zeta(F) \equiv \frac{1}{2}\left\langle [v_F^<(t)]^2 \right\rangle, \tag{B.4}$$

which, being assumed stationary, does not depend on the time variable. The factor $1/2$ is introduced into the definition in order to agree with the standard definition of the kinetic energy. $\zeta(F)$ may be interpreted as the mean kinetic energy in (temporal) scales greater than $\sim F^{-1}$. Using Parseval's theorem, the cumulative energy spectrum can be shown to be a non-decreasing function of the cut-off frequency F.

The energy spectrum of a stationary random function $v(t, \varpi)$ is defined by

$$E(f) \equiv \frac{\mathrm{d}}{\mathrm{d}f}\zeta(f) \geq 0, \tag{B.5}$$

where the positivity follows from the non-decreasing property. $E(f)\mathrm{d}f$ is interpreted as the contribution to the mean kinetic energy of those Fourier harmonics which have the absolute value of their frequency between f and $f + \mathrm{d}f$.

When $F \to \infty$, the filtered velocity field reduces to the unfiltered one. With that in mind and from (B.4) and (B.5) we have

$$\frac{1}{2}\left\langle v^2 \right\rangle = \int_0^\infty E(f)\mathrm{d}f. \tag{B.6}$$

Therefore, the mean kinetic energy (one-half of the variance of the random function) is the integral of the energy spectrum over all frequencies. Since the Fourier transform of $\mathrm{d}v/\mathrm{d}t$ is $if\hat{v}_f$, we obtain

$$\frac{1}{2}\left\langle \left(\frac{\mathrm{d}v(t,\varpi)}{\mathrm{d}t}\right)^2 \right\rangle = \int_0^\infty f^2 E(f)\mathrm{d}f. \tag{B.7}$$

And using the identity

$$\int_{-\infty}^{+\infty} e^{\mathrm{i}(f-\acute{f})t}\mathrm{d}t = 2\pi\delta(f - f'), \tag{B.8}$$

we have

$$E(f) = \frac{1}{2\pi}\int_{-\infty}^{+\infty} e^{\mathrm{i}fs}\Gamma(s)\mathrm{d}s, \tag{B.9}$$

where $\Gamma(s) = \langle \mathbf{v}(\mathbf{r}) \cdot \mathbf{v}(\mathbf{r}') \rangle$ and $s = |\mathbf{r} - \mathbf{r}'|$. The correlation function $\Gamma(s)$ and the energy spectrum are Fourier transforms of each other. Equation (B.9) is known as the Wiener-Khinchin formula. It also demonstrates that the Fourier transform of the correlation function of a stationary random function must be non-negative. Using the above definitions, the energy and helicity spectrum for a thin flux tube is discussed in chapter 3.

The equation (B.9) also results in an expression for the second order structure function, defined as the mean square of the velocity increment from time t to t' which is

$$\left\langle (v(t') - v(t))^2 \right\rangle = 2\int_{-\infty}^{+\infty} \left(1 - e^{if(t'-t)}\right) E(f)\mathrm{d}f, \tag{B.10}$$

where $E(f)$ is extended to negative frequencies by $E(-f) = E(f)$.

When a random function has stationary increments without being stationary (B.9) is not applicable, however (B.10) remains valid. A particularly relevant case for turbulence occurs when the energy spectrum $E(f)$ is a power law (Kolmogorov 1940):

$$E(f) = C\,|f|^{-n}\,, \qquad C > 0. \tag{B.11}$$

When the above equation is substituted into (B.6) this gives a divergent integral. The divergence happens either at high frequencies (ultraviolet divergence) when $n < 1$ or at low frequencies (infra-red divergence) when $n > 1$ or at both when $n = 1$. This suggests that there cannot exist a stationary random function with finite variance and a power law spectrum. Now if we substitute (B.11) into (B.10), we find that no divergence occurs as long as $1 < n < 3$. The calculation shows that

$$\begin{aligned} \left\langle (v(t') - v(t))^2 \right\rangle &= C A_n\,|t' - t|^{n-1}\,, \\ A_n &= 2\int_{-\infty}^{+\infty} (1 - e^{\mathrm{i}x})\,|x|^{-n}\,\mathrm{d}x. \end{aligned} \tag{B.12}$$

Therefore, $v(t)$ has stationary increments, in a mean square sense.

Random functions with stationary increments usually appear as limits of stationary random functions with an infra-red cut-off, when the cut-off frequency tends to zero. An example is the stationary Gaussian random function, called the 'Ornstein-Uhlenbeck process', which has the correlation function $\Gamma(t) = f_0^{-1} e^{-f_0|t|}$ and the spectrum $E(f) = (1/\pi)(f_0^2 + f^2)^{-1}$ [88].

We can extend everything presented in this section from the time domain into the spatial domain when the latter is unbounded. For instance, the cumulative spatial energy spectrum is defined by

$$\zeta(k) \equiv \frac{1}{2}\left\langle |\mathbf{v}_k^<(\mathbf{r})|^2 \right\rangle, \tag{B.13}$$

where $\mathbf{v}_k^<$ is the low-pass filtered vector velocity field containing all harmonics with wave-number less or equal to K. The spatial energy spectrum is then

$$E(k) \equiv \frac{\mathrm{d}\zeta(k)}{\mathrm{d}k}. \tag{B.14}$$

Although the space is three-dimensional, the variables k and K are wave-numbers, i.e. positive scalars. Therefore, the mean energy is obtained from $E(k)$ by the same one-dimensional integral as (B.6) substituting with the variable k in place of f.

We can also define a three-dimensional energy spectrum $E_{3D}(\mathbf{k})$ which is the three-dimensional Fourier transform of the spatial correlation function $\langle \mathbf{v}(\mathbf{r}) \cdot \mathbf{v}(\mathbf{r}') \rangle$. In the incompressible isotropic case, the Wiener-Khinchin formula reads

$$E(k) = 4\pi k^2 E_{3D}(k) = \frac{1}{\pi} \int_0^\infty k\rho\, \Gamma(\rho)\, \sin\, k\rho\, \mathrm{d}\rho, \tag{B.15}$$

where

$$\Gamma(\rho) \equiv \langle \mathbf{v}(\mathbf{r}) \cdot \mathbf{v}(\mathbf{r}') \rangle\,, \qquad \rho = |\mathbf{r} - \mathbf{r}'|\,. \tag{B.16}$$

Once we use L-periodic boundary conditions, the cumulative energy spectrum defined by (B.13) will change discontinuously with K because the only admissible wave-vectors are in $(2\pi/L)\mathbf{Z}^3$. Therefore , the energy spectrum $E(k)$ will be a sum of δ-functions. Also, the continuous case can be recovered by letting $L \to \infty$ and $2\pi n/L = k =$ constant (thus $n \to \infty$ as well).

Finally, we find the energy spectrum is a power law

$$E(k) \propto k^{-n}, \quad 1 < n < 3, \tag{B.17}$$

and the second order spatial structure function is also a power law:

$$\left\langle |\mathbf{v}(\mathbf{r}') - \mathbf{v}(\mathbf{r})|^2 \right\rangle \propto |\mathbf{r}' - \mathbf{r}|^{n-1}\,. \tag{B.18}$$

Appendix C

Kolmogorov worked with freely decaying turbulence (no driving force). He also assumed the existence of an inertial range of values for l: (i) sufficiently small to approximate the time-rate-of-change of the velocity correlation function for separation l by its value for zero separation, namely -2ϵ, and (ii) sufficiently large so that the dissipation term $\nu\nabla_l^2 \langle \mathbf{v}(\mathbf{r}) \cdot \mathbf{v}(\mathbf{r}+l)\rangle$ can be neglected. In the calculations presented by Uriel Frisch [88], he emphasizes that the turbulence is maintained by a driving force. With this, it follows from (1.56) that consistency is established if the following relations

$$K \gg K_c \sim l_0^{-1} \qquad \text{and} \qquad |2\nu\Omega_K| \ll \epsilon, \tag{C.1}$$

simultaneously exist. The range of wave-numbers for which the above conditions (C.1) are satisfied is, by definition, the inertial range. It is called the inertial range, because, at these wave-numbers, the dynamics are dominated by the inertia terms in the Navier-Stokes equations, i.e. all terms except the viscous and forcing terms. Considering (1.59), the second condition in (C.1) will be satisfied if

$$K \ll (\frac{\epsilon}{2\nu E})^{1/2} = (\frac{\Omega}{E})^{1/2} = \frac{\sqrt{5}}{\lambda}, \tag{C.2}$$

where E and Ω are the mean energy and mean enstrophy as defined before. The right-hand side is the inverse of the Taylor scale λ, defined as

$$\frac{1}{\lambda^2} = \frac{\Omega}{5E}. \tag{C.3}$$

For small ν, the Taylor scale $\lambda \propto \nu^{1/2}$ (since ϵ and E are assumed to stay finite). Therefore, when the viscosity is small, the inertial range extends from scales $\sim l_0$ down to at least scales $\sim \lambda \propto \nu^{1/2}$.

Next, we see that (1.64) is invariant under random Galilean transformations. In the absence of forcing and boundaries, the Navier-Stokes equations are invariant under Galilean transformations, since for any vector $\mathbf{U}$, if $\mathbf{v}(t, \mathbf{r})$ is a solution, so is

$$\mathbf{v}'(t, \mathbf{r}) \equiv \mathbf{v}(t, \mathbf{r} - \mathbf{U}t) + \mathbf{U}. \tag{C.4}$$

If $\mathbf{v}(t, \mathbf{r})$ is homogeneous and stationary, so is $\mathbf{v}'(t, \mathbf{r})$. However, isotropy is not preserved, since $\mathbf{U}$ introduces a preferred direction. Therefore, Galilean invariance cannot be easily used to test predictions of a theory of homogeneous and isotropic turbulence. To overcome this difficulty Kraichnan [122, 123, 124] considered taking $\mathbf{U}$ to be random and isotropically distributed. With such a Galilean transformation, all of the structure functions, and specially $S_3(l)$, remain invariant. In fact, the velocity-shift $\mathbf{U}$ cancels in the velocity increment and the shift $\mathbf{U}t$ in the spatial argument cancels by homogeneity. Also the mean dissipation ϵ is invariant. Therefore, as a result the whole four-fifths relation (1.64) remains invariant. It is important to note that the presence of a driving force breaks Galilean and random Galilean invariances of the Navier-Stokes equations, however this does not affect the derivation of the four-fifth law since the (single-time) correlations of the velocity and force are invariant under Galilean transformations.

Also, in deriving the four-fifths law, there are several limits taken: First, the limit $t \to \infty$ gives a statistical steady state. Second, the limit $\nu \to 0$ eliminates any residual dissipation at finite scales. Third, the limit $l \to 0$ eliminates the direct influence of large-scale forcing. The correct formulation of (1.64) is therefore

$$\lim_{l\to 0} \lim_{\nu\to 0} \lim_{t\to\infty} \frac{S_3(l)}{l} = -\frac{4}{5}\,\epsilon. \tag{C.5}$$

Note that attempts to take the limits in a different order result in difficulties. For instance, if we take $l \to 0$ before $\nu \to 0$, the third order structure function is expected to behave as l^3; in fact, in the presence of viscosity, for small separations the velocity increments will be linear in l because the flow is expected to be smooth. Whether or not the $\nu \to 0$ and the $t \to \infty$ limits can be interchanged depends on the smoothness of the solution to the three dimensional Euler equations (the Navier-Stokes equations with $\nu = 0$). If there are no singularities in finite time, then one can show that at any finite time, the energy dissipation tends to zero with the viscosity, and not to a finite positive limit as required for the derivation of the four-fifths law.

Finally, it is important to note that without the assumption of isotropy, a relation analogous to the four-fifths law can still be derived. With all the other assumptions remaining, it can be shown that in the limit of $\nu \to 0$ and for small l

$$-\frac{1}{4}\nabla_l \cdot \left\langle |\delta v(l)|^2\, \delta v(l) \right\rangle = \epsilon. \tag{C.6}$$

The above relation was also derived by Monin and Yaglom [157]. They addressed the interesting question as to what happens if the flow is homogeneous at all scales while

being isotropic only at small-scales. As a result of velocity increments appearing in (C.6), when l is small, the above equation should become equivalent to the four-fifths law (1.64). However, (1.64) involves exclusively longitudinal velocity increments, while (C.6) involves both longitudinal and transverse velocity increments.

Another important point is the case in which the flow is isotropic but has only homogeneous increments, as assumed in the K41 theory (section 1.3). One must point out that random functions with homogeneous increments can be considered as limits of strictly homogeneous random functions. If a small-scale flow with homogeneous isotropic increments can be embedded in a large-scale homogeneous isotropic flow, then the four-fifths law remains valid. The embedding flow does not need to be a solution of the Navier-Stokes equations, as long as it is incompressible [88].

Finally one can conclude that at the moment the best available experimental evidence supports the validity of the four-fifths law.

Bibliography

[1] A. Alexakis, P. D. Mininni, and A. Pouquet. Shell-to-shell energy transfer in magnetohydrodynamics. I. steady state turbulence. *Physical Review E*, 72:046301–1–046301–10, 2005.

[2] J. J. Aly and T. Amari. Current sheets in two-dimensional potential magnetic fields. III. Formation in complex topology configurations and application to coronal heating. *Astrophysics and Astronomy*, 319:699–719, 1997.

[3] S. K. Antiochos and R. B. Dahlburg. The implications of 3D for solar MHD modeling. *Solar Physics*, 174:5–19, 1997.

[4] V. Archontis, F. Moreno-Insertis, K. Galsgaard, A. Hood, and E. O'Shea. Emergence of magnetic flux from the convection zone into the corona. *Astronomy and Astrophysics*, 426:1047–1063, 2004.

[5] V. I. Arnold and E. I. Korkina. The growth of magnetic field in a three-dimensional steady incompressible flow (in Russian). *Vest. Mosk. Un. Ta. Ser. 1, Mat. Mec.*, 3:43–46, 1983.

[6] E. Artin. Theory of braids. *Ann. of Math*, 48:101, 1947.

[7] M. J. Aschwanden. An evolution of coronal heating models for active regions based on Yohkoh, Soho, and Trace observations. *The Astrophysical Journal*, 560:1035–1044, 2001.

[8] M. J. Aschwanden. An observational test that disproves coronal nanoflare heating models. *The Astrophysical Journal*, 672:L135–L138, 2008.

[9] M. J. Aschwanden, A. Winebarger, D. Tsliklauri, and H. Peter. The coronal heating paradox. *The Astrophysical Journal*, 659:1673–1681, 2007.

[10] M. Asgari-Targhi and M. A. Berger. Writhe in the stretch-twist-fold dynamo. *Geophysical and Astrophysical Fluid Dynamics*, 103:69–87, 2009.

[11] K. L. Babcock and R. M. Westervelt. Avalanches and self-organization in cellular magnetic-domain patterns. *Physical Review Letters*, 64:2168–2171, 1990.

[12] M. Baiesi, M. Paczuski, and A. L. Stella. Intensity thresholds and the statistics of the temporal occurrence of solar flares. *Cond-mat.stat-mech*, 2:0411342, 2005.

[13] P. Bak, K. Chen, and C. Tang. A forest-fire model and some thoughts on turbulence. *Physics Letters A*, 147:297–300, 1990.

[14] P. Bak, C. Tang, and K. Wiesenfeld. Self-organized criticality: An explanation of the 1/f noise. *Physical Review Letters*, 59:381–384, 1987.

[15] P. Bak, C. Tang, and K. Wiesenfeld. Self-organized criticality. *Physical Review A*, 38:364–374, 1988.

[16] P. D. Bangert, M. A. Berger, and R. Prandi. In search of minimal random braid configurations. *J. Phys. A: Math. Gen.*, 35:43–59, 2002.

[17] S. Bao and H. Zhang. Patterns of current helicity for the twenty-second solar cycle. *The Astrophysical Journal Letters*, 496:L43–L46, 1998.

[18] S. D. Bao, H. Q. Zhang, G. X. Ai, and M. Zhang. A survey of flares and current helicity in active regions. *Astronomy and Astrophysics Supplement Series*, 139:311–320, 1999.

[19] S. Basu. Seismology of the base of the solar convection zone. *Monthly Notices of the Royal Astronomical Society*, 288:572–584, 1997.

[20] G. K. Batchelor. Small-scale variation of convected quantities like temperature in turbulent fluid part 1 general discussion and the case of small conductivity. *Journal of Fluid Mechanics*, 5:113–133, 1959.

[21] G. K. Batchelor. The theory of homogeneous turbulence. *Cambridge University Press*, 1993.

[22] G. Bateman. MHD instabilities. *The MIT Press*, 1978.

[23] R. Beck, A. Brandenburg, D. Moss, A. Shukurov, and D. Sokoloff. Galactic magnetism: Recent developments and perspectives. *Annu. Rev. Astron. Astrophys*, 34:155–206, 1996.

[24] M. A. Berger. Rapid reconnection and the conservation of magnetic helicity. *Bulletin American Astron. Soc.*, 14:978, 1982.

[25] M. A. Berger. Braided flux ropes and coronal heating. *Geophysical Monograph, American Geophysical Union, Florida*, 251, 1989.

[26] M. A. Berger. Third-order invariants of randomly braided curves. *Topological Fluid Mechanics, edited by H. K. Moffatt and A. Tsinober, Cambridge University Press, Cambridge*, pages 440–448, 1990.

[27] M. A. Berger. Generation of coronal magnetic fields by random surface motions: I. mean square twist and current density. *Astronomy and Astrophysics*, 252:369–376, 1991.

[28] M. A. Berger. Generation of coronal magnetic fields by random surface motions. I - mean square twist and current density. *Astrophysics and Astronomy*, 252:369–376, 1991.

[29] M. A. Berger. Third order braid invariants,. *Journal of Physics A: Mathematical and General*, 24:4027–4036, 1991.

[30] M. A. Berger. Energy-crossing number relations for braided magnetic fields. *Physical Review Letters*, 70:705–708, 1993.

[31] M. A. Berger. Coronal heating by dissipation of magnetic structure. *Space Science Reviews*, 68:3–14, 1994.

[32] M. A. Berger. Magnetic helicity in a periodic domain. *Journal of Geophysical Research*, 102:2637–2644, 1997.

[33] M. A. Berger. Introduction to magnetic helicity. *Plasma Physics and Controlled Fusion*, 41:B167–B175, 1999.

[34] M. A. Berger and G. B. Field. The topological properties of magnetic helicity. *Journal of Fluid Mechanics*, 147:133–148, 1984.

[35] M. A. Berger and C. Prior. The writhe of open and closed curve. *J. Phys. A: Math. Gen.*, 39:8321–8348, 2006.

[36] M. A. Berger and P. H. Roberts. On the winding number problem with finite steps. *Advances in applied probability*, 20:261–274, 1988.

[37] M. A. Berger and A. Ruzmaikin. Rate of helicity production by solar rotation. *Journal of Geophysical Research*, 105:10481–10490, 2000.

[38] D. Biskamp. Magnetic reconnection in plasmas. *Cambridge University Press, Cambridge*, 2000.

[39] E. G. Blackman and A. Brandenburg. Doubly helical coronal ejections from dynamos and their role in sustaining the solar cycle. *The Astrophysical Journal Letters*, 584:L99–L102, 2003.

[40] E. G. Blackman and G. B. Field. Coronal activity from dynamos in astrophysical rotators. *Monthly Notices of the Royal Astronomical Society*, 318:724–732, 2000.

[41] A. Brandenburg. The inverse cascade and nonlinear alpha-effect in simulations of isotropic helical hydromagnetic turbulence. *The Astrophysical Journal*, 550:824–840, 2001.

[42] A. Brandenburg, W. Dobler, and K. Subramanian. Magnetic helicity in stellar dynamos: new numerical experiments. *Astronomische Nachrichten*, 323:99–122, 2002.

[43] A. Brandenburg, K. Enqvist, and P. Olesen. Large-scale magnetic fields from hydromagnetic turbulence in the very early universe. *Phys. Rev. D*, 54:1291–1300, 1996.

[44] A. Brandenburg, R. L. Jennings, . Nordlund, M. Rieutord, R. F. Stein, and I. Tuominen. Magnetic structures in a dynamo simulation. *Journal of Fluid Mechanics*, 306:325–352, 1996.

[45] A. Brandenburg, A. Nordlund, R. F. Stein, and U. Torkelsson. Dynamo-generated turbulence and large scale magnetic fields in a Keplerian shear flow. *The Astrophysical Journal*, 446:741–754, 1995.

[46] A. Brandenburg and K. Subramanian. Astrophysical magnetic fields and nonlinear dynamo theory. *Physics Reports*, 417:1–209, 2005.

[47] M. R. Brown, R. C. Canfield, and A. A. Pevtsov. Magnetic helicity in space and laboratory plasmas. *Geophys. Monograph 111, American Geophysical Union, Florida*, 1999.

[48] P. K. Browning and E. R. Priest. Heating of coronal arcades by magnetic tearing turbulence, using the Taylor-Heyvaerts hypothesis. *Astrophysics and Astronomy*, 159:129–141, 1986.

[49] E. Buchlin, P. J. Cargill, S. J. Bradshaw, and M. Velli. Profiles of heating in turbulent coronal magnetic loops. *Astronomy and Astrophysics*, 469:347–354, 2007.

[50] A. B. Burnette, R. C. Canfield, and A. A. Pevtsov. Photospheric and coronal currents in solar active regions. *The Astrophysical Journal*, 606:565–570, 2004.

[51] J. M. Carlson and J. S. Langer. Properties of earthquakes generated by fault dynamics. *Physical Review Letters*, 62:2632–2635, 1989.

[52] P. Charbonneau, S. McIntosh, H. Liu, and T. Bogdan. Reconnection of twisted flux tubes as a function of contact angle. *Solar Physics*, 203:321–353, 2001.

[53] S. Childress. New solutions of the kinematic dynamo problem. *Journal of Mathematical Physics*, 11:3063–3076, 1970.

[54] S. Childress, P. Collet, U. Frisch, A. D. Gilbert, H. K. Moffatt, and G. M. Zaslavsky. Report on workshop on small-diffusivity dynamos and dynamical systems. *Geophysical and Astrophysical Fluid Dynamics*, 52:263–270, 1990.

[55] S. Childress and A. D. Gilbert. Stretch, twist, fold: the fast dynamo. *Berlin: Springer*, 1995.

[56] D. Y. Chou and G. H. Fisher. Dynamics of anchored flux tubes in the convection zone. I - details of the model. *The Astrophysical Journal*, 341:533–548, 1989.

[57] A. R. Choudhuri and P. A. Gilman. The influence of the coriolis force on flux tubes rising through the solar convection zone. *The Astrophysical Journal*, 316:788–800, 1987.

[58] T. G. Cowling. The magnetic field of sunspots. *Monthly Notices of the Royal Astronomical Society*, 94:39–48, 1934.

[59] Călugăreanu. On isotopy classes of three dimensional knots and their invariants. *Czech. Math. J.*, 11:588–625, 1961.

[60] R. B. Dahlburg, S. K. Antiochos, and D. Norton. Magnetic flux tube tunneling. *Physical Review E*, 56:2094–2103, 1997.

[61] R. B. Dahlburg, J. A. Klimchuck, and S. K. Antiochos. An explanation for the "Switch-On" nature of magnetic energy release and its application to coronal heating. *The Astrophysical Journal*, 622:1191–1201, 2005.

[62] D. W. Datlowe, M. J. Elcan, and H. S. Hudson. OSO-7 observations of solar X-rays in the energy range 10-100 kev. *Solar Physics*, 39:155–174, 1974.

[63] P. A. Davidson. An introduction to magnetohydrodynamics. *Cambridge University Press, Cambridge, England*, 2001.

[64] O. Debliquy, M. K. Verma, and D. Carati. Energy fluxes and shell-to-shell transfers in three-dimensional decaying magnetohydrodynamic turbulence. *Physics of Plasmas*, 12:042309–1–042309–10, 2005.

[65] P. Démoulin, J. C. Henoux, E. R. Priest, and C. H. Mandrini. Quasi-separatrix layers in solar flares. I. method. *Astronomy and Astrophysics*, 308:643–655, 1996.

[66] P. Démoulin, C. H. Mandrini, L. van Driel-Gesztelyi, M. C. Lopez Fuentes, and G. Aulanier. The magnetic helicity injected by shearing motions. *Solar Physics*, 207:87–110, 2002.

[67] P. Démoulin, L. van Driel-Gesztelyi, C. H. Mandrini, J. A. Klimchuk, and L. Harra. The long-term evolution of AR 7978: Testing coronal heating models. *The Astrophysical Journal*, 586:592–605, 2003.

[68] B. R. Dennis. Solar hard X-ray bursts. *Solar Physics*, 100:465–490, 1985.

[69] B. R. Dennis. Solar flare hard X-ray observations. *Solar Physics*, 118:49–94, 1988.

[70] C. R. DeVore. Magnetic helicity generation by solar differential rotation. *The Astrophysical Journal*, 539:944–953, 2000.

[71] R. F. Dillon. Gravity and magnetic field correlation and related geometric topics. *Cambridge University, PhD thesis, Chapter 6*, 1974.

[72] P. Dmitruk and D. O. Gómez. Turbulent coronal heating and the distribution of nanoflares. *The Astrophysical Journal Letters*, 484:L83–L86, 1997.

[73] S. B. F. Dorch and A. Nordlund. On the transport of magnetic fields by solar-like stratified convection. *Astronomy and Astrophysics*, 365:562–570, 2001.

[74] B. Drossel and F. Schwabl. Self-organized critical forest-fire model. *Physical Review Letters*, 69:1629–1632, 1992.

[75] S. D'Silva and A. R. Choudhuri. A theoretical model for tilts of bipolar magnetic regions. *Astronomy and Astrophysics*, 272:621–633, 1993.

[76] S. F. Edwards. The statistical dynamics of homogeneous turbulence. *Journal of Fluid Mechanics*, 18:239–273, 1964.

[77] S. F. Edwards. Turbulence in hydrodynamics and plasma physics. *International Atomic Energy Agency, Vienna*, pages 595–623, 1965.

[78] G. Einaudi, M. Velli, H. Politano, and A. Pouquet. Energy release in a turbulent corona. *The Astrophysical Journal Letters*, 457:L113–L116, 1996.

[79] M. Epple. Orbits of asteroids, a braid, and the first link invariant. *Mathematical Intelligencer*, 20:45–52, 1998.

[80] R. Falewicz and P. Rudawy. X-type interactions of loops in the flare of 25 september 1997. *Astronomy and Astrophysics*, 344:981–990, 1999.

[81] E. Falgarone and T. Passot. Turbulence and magnetic fields in astrophysics. *Springer*, 2002.

[82] Y. Fan, G. H. Fisher, and E. E. Deluca. The origin of morphological asymmetries in bipolar active regions. *The Astrophysical Journal*, 405:390–401, 1993.

[83] F. Fárník, H. Hudson, and T. Watanabe. Spatial relations between preflares and flares. *Solar Physics*, 165:169–179, 1996.

[84] G. B. Field and E. G. Blackman. Dynamical quenching of the α^2 dynamo. *The Astrophysical Journal*, 572:685–692, 2002.

[85] E. N. Frazier and J. O. Stenflo. On the small-scale structure of solar magnetic fields. *Solar Physics*, 27:330–346, 1972.

[86] E. N. Frazier and J. O. Stenflo. On the small-scale structure of solar magnetic fields. *Solar Physics*, 27:330–346, 1972.

[87] M. H. Freedman and Z. X. He. Divergence-free fields: energy and asymptotic crossing number. *Ann. Math. Ser. 2*, 134:189–229, 1991.

[88] U. Frisch. Turbulence. *Cambridge University Press*, 1995.

[89] U. Frisch and R. Morf. Intermittency in nonlinear dynamics and singularities at complex times. *Physical Review A*, 23:2673–2705, 1981.

[90] Y. Gagne. Etude expérimentale de l'intermittence et des singularités dans le plan complexe en turbulence développée, Thèse de Docteur ès-Sciences Physiques, Université de Grenbole. 1987.

[91] D. Galloway and U. Frisch. A numerical investigation of magnetic field generation in a flow with chaotic streamlines. *Geophysical and Astrophysical Fluid Dynamics*, 29:13–18, 1984.

[92] R. K. Galloway, P. Helander, and A. L. MacKinnon. Cross-field diffusion of electrons in tangled magnetic fields and implications for coronal fine structure. *The Astrophysical Journal*, 646:615–624, 2006.

[93] K. Galsgaard and A. Nordlund. Heating and activity of the solar corona 1. boundary shearing of an initially homogeneous magnetic field. *Journal of Geophysical Research*, 101:13445–13460, 1996.

[94] K. Galsgaard and A. Nordlund. Heating and activity of solar corona 2. kink instability in a flux tube. *Journal of Geophysical Research*, 102:219–230, 1997.

[95] A. Gilbert. Magnetic helicity in fast dynamos. *Geophysical and Astrophysical Fluid Dynamics*, 96:135–151, 2002.

[96] W. M. Glencross. Heating of coronal material at X-ray bright points. *The Astrophysical Journal*, 199:L53–L56, 1975.

[97] M. L. Goldstein and D. A. Roberts. Magnetohydrodynamic turbulence in the solar wind. *Physics of Plasmas*, 6:4154–4160, 1999.

[98] P. Grassberger and H. Kantz. On a forest fire model with supposed self-organized criticality. *Journal of Statistical Physics*, 63:685–700, 1991.

[99] G. Halberstadt and J. P. Goedbloed. Alfven wave heating of coronal loops: photospheric excitation. *Astronomy and Astrophysics*, 301:559–576, 1995.

[100] G. E. Hale. On the probable existence of a magnetic field in sun-spots. *The Astrophysical Journal*, 28:315–343, 1908.

[101] G. E. Hale, F. Ellerman, S. B. Nicholson, and A. H. Joy. The magnetic polarity of sun-spots. *The Astrophysical Journal*, 49:153–178, 1919.

[102] Y. Hanaoka. A flare caused by interacting coronal loops. *The Astrophysical Journal*, 420:L37–L40, 1994.

[103] J. F. Hawley and S. A. Balbus. Transport in accretion disks. *Physics of Plasmas*, 6:4444–4449, 1999.

[104] W. Heisenberg. Zur statistischen theorie der turbulenz. *Zeitschrift für Physik*, 124:628–657, 1948.

[105] J. Heyvaerts and E. R. Priest. Coronal heating by reconnection in DC current systems - A theory based on Taylor's hypothesis. *Astronomy and Astrophysics*, 137:63–78, 1984.

[106] J. Heyvaerts, E. R. Priest, and D. M. Rust. An emerging flux model for the solar flare phenomenon. *The Astrophysical Journal*, 216:123–137, 1977.

[107] J. Heyvaerts, E. R. Priest, and D. M. Rust. An emerging flux model for the solar flare phenomenon. *The Astrophysical Journal*, 216:123–137, 1977.

[108] J. V. Hollweg. Energy and momentum transport by waves in the solar atmosphere, in "Advances in Space Plasma Physics". *ed. by B. Buti, World Scientific, Singapore*, 77–141, 1986.

[109] R. Howe, J. Christensen-Dalsgaard, F. Hill, R. W. Komm, R. M. Larsen, J. Schou, M. J. Thompson, and J. Toomre. Deeply penetrating banded zonal flows in the solar convection zone. *The Astrophysical Journal*, 533:L163–L166, 2000.

[110] D. Hughes, M. Paczuski, R. O. Dendy, P. Helander, and K. G. McClements. Solar flares as cascades of reconnecting magnetic loops. *Physical Review Letters*, 90:131101–131101.4, 2003.

[111] G. W. Inverarity and E. R. Priest. Turbulent coronal heating 3. Wave heating in coronal loops. *Astronomy and Astrophysics*, 302:567–577, 1995.

[112] R. Jain and S. Yashiro. Filling factors and magnetic field strengths of nanoflare-heated coronal active regions: Yohkoh and MDI observations. *Astronomy and Astrophysics*, 394:1111–1116, 2002.

[113] J. Jakimiec, M. Tomczak, R. Falewicz, K. J. H. Phillips, and A. Fludra. The bright loop-top kernels in Yohkoh X-ray flares. *Astronomy and Astrophysics*, 334:1112–1122, 1998.

[114] C. A. Jones and D. J. Galloway. Axisymmetric magnetoconvection in a twisted field. *Journal of Fluid Mechanics*, 253:297–326, 1993.

[115] L. Kadanoff, S. R. Nagel, L. Wu, and S. Zhou. Scaling and universality in avalanches. *Physical Review A*, 39:6524–6537, 1989.

[116] T. v. Kármán and L. Howarth. On the statistical theory of isotropic turbulence. *Proc. R. Soc. Lond. A*, 164, 192–215.

[117] J. T. Karpen, S. K. Antiochos, R. B. Dahlburg, and D. S. Spicer. The Kelvin-Helmholtz instability in photospheric flows: Effects on control heating and structure. *The Astrophysical Journal*, 403:769–779, 1993.

[118] A. P. Kazantsev. Enhancement of a magnetic field by a conducting fluid. *Soviet Journal of Experimental and Theoretical Physics*, 26:1031–1034, 1968.

[119] A. L. Kiplinger, B. R. Dennis, K. J. Frost, and L. E. Orwig. Recurrent pulse trains in the solar hard X-ray flare of 1980 june 7. *The Astrophysical Journal*, 273:783–794, 1983.

[120] J. A. Klimchuk. Magnetic reconnection in the solar atmosphere. *Asp Conf. Ser.*, 111:319, 1997.

[121] R. H. Kraichnan. The structure of isotropic turbulence at very high Reynolds numbers. *Journal of Fluid Mechanics*, 5:497–543, 1959.

[122] R. H. Kraichnan. Kolmogorov's hypotheses and Eulerian turbulence theory. *Physics of Fluids*, 7:1723–1734, 1964.

[123] R. H. Kraichnan. Lagrangian-history closure approximation for turbulence. *Physics of Fluids*, 8:575–598, 1965.

[124] R. H. Kraichnan. Lagrangian-history statistical theory for Burgers' equation. *Physics of Fluids*, 11:265–277, 1968.

[125] F. Krause. The cosmic dynamo: From t = - ∞ to Cowling's theorem. a review on history. *The cosmic dynamo: proceedings of the 157th Symposium of the International Astronomical Union held in Potsdam; F.R.G.; September 7-11; 1992. Edited by F. Krause, K. H. Radler, and Gunther Rudiger. International Astronomical Union. Symposium no. 157; Kluwer Academic Publishers; Dordrecht*, pages 487–499, 1993.

[126] F. Krause and K. H. Radler. Mean-field magnetohydrodynamics and dynamo theory. *Oxford: Pergamon Press*, 1980.

[127] P. P. Kronberg. Extragalactic magnetic fields. *Rep. Prog. Phys*, 57:325–382, 1994.

[128] R. M. Kulsrud. A critical review of galactic dynamos. *Annual Review of Astronomy and Astrophysics*, 37:37–64, 1999.

[129] J. K. Lawrence and C. J. Schrijver. Anomalous diffusion of magnetic elements across the solar surface. *The Astrophysical Journal*, 411:402–405, 1993.

[130] K. D. Leka, R. C. Canfield, A. N. McClymont, and L. van Driel-Gesztelyi. Evidence for current-carrying emerging flux. *The Astrophysical Journal*, 462:547–560, 1996.

[131] R. P. Lin, R. A. Schwartz, S. R. Kane, R. M. Pelling, and K. C. Hurley. Solar hard X-ray microflares. *The Astrophysical Journal*, 283:421–425, 1984.

[132] M. G. Linton, R. B. Dahlburg, and S. K. Antiochos. Reconnection of twisted flux tubes as a function of contact angle. *The Astrophysical Journal*, 553:905–921, 2001.

[133] M. G. Linton, R. B. Dahlburg, G. H. Fisher, and D. W. Longcope. Nonlinear evolution of kink-unstable magnetic flux tubes and solar delta-spot active regions. *The Astrophysical Journal*, 507:404–416, 1998.

[134] D. W. Longcope. Determining the source of coronal helicity through measurements of braiding and spin helicity fluxes in active regions. *Living Reviews of Solar Physics*, 2:7, 2005.

[135] D. W. Longcope, G. H. Fisher, and S. Arendt. The evolution and fragmentation of rising magnetic flux tubes. *The Astrophysical Journal*, 464:999–1011, 1996.

[136] D. W. Longcope, G. H. Fisher, and A. A. Pevtsov. Flux-tube twist resulting from helical turbulence: The sigma-effect. *The Astrophysical Journal*, 507:417–432, 1998.

[137] D. W. Longcope and I. Klapper. Dynamics of a thin twisted flux tube. *The Astrophysical Journal*, 488:443–453, 1997.

[138] D. W. Longcope, M. G. Linton, A. A. Pevtsov, G. H. Fisher, and I. Klapper. Magntic helicity in space and laboratory plasmas, ed. M. R. Brown, R. C. Canfield, A. A. Pevtsov. *Washington, D.C: AGU, 93*, 1999.

[139] D. W. Longcope and E. J. Noonan. Self-organized criticality from separator reconnection in solar flares. *The Astrophysical Journal*, 542:1088–1099, 2000.

[140] D. W. Longcope, B. Ravindra, and G. Barnes. Determining the source of coronal helicity through measurements of braiding and spin helicity fluxes in active regions. *The Astrophysical Journal*, 668:571–585, 2007.

[141] B. C. Low. Equilibrium and dynamics of coronal magnetic fields. *Annual Review of Astronomy and Astrophysics*, 28:491–524, 1990.

[142] E. T. Lu and R. J. Hamilton. Avalanches and the distribution of solar flares. *The Astrophysical Journal*, 380:L89–L92, 1991.

[143] E. T. Lu, R. J. Hamilton, J. M. McTiernan, and K. R. Bromund. Solar flares and avalanches in driven dissipative systems. *The Astrophysical Journal*, 412:841–852, 1993.

[144] E. T. Lu and V. Petrosian. The relative timing of microwaves and X-rays from solar flares. *The Astrophysical Journal*, 354:735–744, 1990.

[145] M. E. Machado, R. L. Moore, A. M. Hernandez, M. G. Rovira, M. J. Hagyard, and J. B. Smith. The observed characteristics of flare energy release. I - Magnetic structure at the energy release site. *The Astrophysical Journal*, 326:425–450, 1988.

[146] M. E. Machado, K. K. Ong, A. G. Emslie, G. Fishman, C. Meegan, R. B. Wilson, and W. S. Paciesas. *Adv. Space. Res*, 13:175, 1993.

[147] K. P. Macpherson and A. L. MacKinnon. One-dimensional percolation models of transient phenomena. *Physica A*, 243:1–13, 1997.

[148] F. Maggioni and R. L. Ricca. Writhing and coiling of closed filaments. *Proceedings-Royal Society. Mathematical, Physical and Engineering Sciences*, 462:3151–3166, 2006.

[149] B. B. Mandelbrot. Intermittent turbulence in self-similar cascades: divergence of high moments and dimension of the carrier. *Journal of Fluid Mechanics*, 62:331–358, 1974.

[150] C. H. Mandrini, P. Démoulin, and J. A. Klimchuk. Magnetic field and plasma scaling laws: Their implications for coronal heating models. *The Astrophysical Journal*, 530:999–1015, 2000.

[151] Z. Mikić. Magnetohydrodynamic modelling of the solar corona. *Physics of Fluids B*, 2:1450–1454, 1990.

[152] Z. Mikić, D. D. Schnack, and G. Van Hoven. Creation of current filaments in the solar corona. *The Astrophysical Journal*, 338:1148–1157, 1989.

[153] H. K. Moffatt. The degree of knottedness of tangled vortex lines. *Journal of Fluid Mechanics*, 35:117–129, 1969.

[154] H. K. Moffatt. Magnetic field generation in electrically conducting fluids. *Cambridge University Press*, 1978.

[155] H. K. Moffatt and M. R. E. Proctor. Topological constraints associated with fast dynamo action. *Journal of Fluid Mechanics*, 154:493–507, 1985.

[156] H. K. Moffatt and R. L. Ricca. Helicity and the călugăreanu invariant. *Proceedings-Royal Society. Mathematical and Physical Sciences*, 439:411–429, 1992.

[157] A. S. Monin and A. M. Yaglom. Statistical fluid mechanics, volume 2: Mechanics of turbulence. 1975.

[158] J. J. Moreau. Séminaire dánalyse convex montpellier, exposé 7. 1977.

[159] F. Moreno-Insertis and T. Emonet. The rise of twisted magnetic tubes in a stratified medium. *The Astrophysical Journal Letters*, 472:L53–L56, 1996.

[160] W. K. Mossner, B. Drossel, and F. Schwabl. Computer simulations of the forest-fire model. *Physica A*, 190(3-4):205–217, 1992.

[161] J. V. Neumann. Recent theories of turbulence, in collected works (1949-1963). *ed. A. H. Taub. Pergamon Press, New York (1963)*, 6:437–472.

[162] C. S. Ng and A. Bhattacharjee. Nonequilibrium and current sheet formation in line-tied magnetic fields. *Physics of Plasmas*, 5:4028–4040, 1998.

[163] E. Noether. Invariants variationsprobleme. *Gott. Nachr. Ges. Wiss. Zu*, JFM 46.0770.01:235–257, 1918.

[164] A. Nordlund, A. Brandenburg, R. L. Jennings, M. Rieutord, J. Ruokolainen, R. F. Stein, and I. Tuominen. Dynamo action in stratified convection with overshoot. *The Astrophysical Journal*, 392:647–652, 1992.

[165] K. O'Brien, L. Wu, and S. R. Nagel. Avalanches in three and four dimensions. *Physical Review A*, 43:2052–2055, 1991.

[166] L. Ofman, J. M. Davila, and R. S. Steinolfson. Coronal heating by the resonant absorption of Alfven waves: Wavenumber scaling laws. *The Astrophysical Journal*, 444:471–477, 1995.

[167] Y. Ono, A. Morita, M. Katsurai, and M. Yamada. Experimental investigation of three-dimensional magnetic reconnection by use of two colliding spheromaks. *Physics of Fluids B: Plasma Physics*, 5:3691–3701, 1993.

[168] M. Ossendrijver. The solar dynamo. *Astronomy and Astrophysics Review*, 11:287–367, 2003.

[169] M. Paczuski and D. Hughes. A heavenly example of scale free networks and self-organized criticality. *Con-mat.stat-mech*, 1:0311304, 2003.

[170] E. Parker. Tangential discontinuities in untidy magnetic topologies. *Physics of Plasmas*, 11:2328–2332, 2004.

[171] E. N. Parker. Topological dissipation and the small-scale fields in turbulent gases. *The Astrophysical Journal*, 174:499–510, 1972.

[172] E. N. Parker. Cosmical magnetic fields: their origin and their activity. *Oxford University Press*, 1979.

[173] E. N. Parker. Magnetic neutral sheets in evolving fields - part two - formation of the solar corona. *The Astrophysical Journal*, 264:642–647, 1983.

[174] E. N. Parker. Nanoflares and the solar X-ray corona. *The Astrophysical Journal*, 330:474–479, 1988.

[175] E. N. Parker. Solar and stellar magnetic fields and atmospheric structures: Theory. *Solar Physics*, 121:271–288, 1989.

[176] S. Patsourakos and J. A. Klimchuk. Coronal loop heating by nanoflares: the impact of the field-aligned distribution of the heating on loop observations. *The Astrophysical Journal*, 628:1023–1030, 2005.

[177] A. A. Pevtsov, R. C. Canfield, and A. N. McClymont. On the subphotospheric origin of coronal electric currents. *The Astrophysical Journal*, 481:973–977, 1997.

[178] A. A. Pevtsov, R. C. Canfield, and T. R. Metcalf. Latitudinal variation of helicity of photospheric fields. *The Astrophysical Journal*, 440:L109–L112, 1995.

[179] A. A. Pevtsov and S. M. Latushko. Current helicity of the large-scale photospheric magnetic field. *The Astrophysical Journal*, 528:999–1003, 2000.

[180] W. F. Pohl. DNA and differential geometry. *Mathematical Intelligencer*, 3:20–27, 1980.

[181] A. Pouquet, U. Frisch, and J. Léorat. Strong MHD helical turbulence and the nonlinear dynamo effect. *Journal of Fluid Mechanics*, 77:321–354, 1976.

[182] E. R. Priest. Solar magnetohydrodynamics. *Geophysics and Astrophysics Monographs*, 21, 1982.

[183] E. R. Priest, C. R. Foley, J. Heyvaerts, T. D. Arber, D. Mackay, J. L. Culhane, and L. W. Acton. A method to determine the heating mechanisms of the solar corona. *The Astrophysical Journal*, 539:1002–1022, 2000.

[184] E. R. Priest, J. F. Heyvaerts, and A. M. Title. A flux-tube tectonics model for solar coronal heating driven by the magnetic carpet. *The Astrophysical Journal*, 576:533–551, 2002.

[185] E. R. Priest, C. E. Parnell, and S. F. Martin. A converging flux model of an X-ray bright point and an associated canceling magnetic feature. *The Astrophysical Journal*, 427:459–474, 1994.

[186] M. Proctor. Dynamo action and the sun. 2006.

[187] K. H. Rädler and A. Brandenburg. Contributions to the theory of a two-scale homogeneous dynamo experiment. *Physical Review E*, 67:026401, 2003.

[188] A. Raoult, M. Pick, B. R. Dennis, and S. R. Kane. Solar flare development during the impulsive phase as deduced from correlated radio and hard X-ray observations. *The Astrophysical Journal*, 299:1027–1035, 1985.

[189] A. F. Rappazzo, M. Velli, G. Einaudi, and R. B. Dahlburg. Nonlinear dynamics of the parker scenario for coronal heating. *The Astrophysical Journal*, 677:1348–1366, 2008.

[190] G. O. Roberts. Spatially periodic dynamos. *Philosophical Transactions of the Royal Society of London*, 266:535–558, 1970.

[191] P. H. Roberts and A. M. Soward. Dynamo theory. *Annual Review of Fluid Mechanics*, 24:459–512, 1992.

[192] R. Rosner, B. C. Low, K. Tsinganos, and M. A. Berger. On the relationship between the topology of magnetic field lines and flux surfaces. *Geophysical and Astrophysical Fluid Dynamics*, 48:251–271, 1989.

[193] R. Rosner and N. O. Weiss. The origin of the solar cycle, in the solar cycle (ed. K. L. Harvey). *Astronomical society of the pacific, conference series 27*, pages 511–531, 1992.

[194] M. S. Ruderman, D. Berghmans, M. Goosens, and S. Poedts. Direct excitation of resonant torsional Alfven waves by foot-point motions. *Astrophysics and Astronomy*, 320:305–318, 1997.

[195] G. Rudiger. Differential rotation and stellar convection. Sun and solar-type stars. *Gordon and Breach, New York*, 1989.

[196] G. Rudiger and R. Hollerbach. The magnetic universe. geophysical and astrophysical dynamo theory. *Wiley-VCH, Weinheim*, 2004.

[197] D. M. Rust and et al. Mass ejections in solar flares. *Ed. P. A. Sturrock, (Boulder, CO: Colorado Assoc. Unive. Press)*, pages 273–339, 1980.

[198] D. M. Rust and A. Kumar. Evidence for helically kinked magnetic flux ropes in solar eruptions. *The Astrophysical Journal*, 464:L199–L202, 1996.

[199] D. M. Rust and B. J. LaBonte. Observational evidence of the kink instability in solar filament eruptions and sigmoids. *The Astrophysical Journal*, 622:L69–L72, 2005.

[200] A. A. Ruzmaikin. The solar cycle as a strange attractor. *Comments Astrophys*, 9:85–96, 1981.

[201] A. A. Ruzmaikin. Redistribution of magnetic helicity at the Sun. *Geophysical Research Letters*, 23:2649–2652, 1996.

[202] J. I. Sakai and S. Koide. Classification of magnetic reconnection during two current-loop coalescence. *Solar Physics*, 142:399–402, 1992.

[203] A. A. Schekochihin, S. C. Cowley, S. F. Taylor, J. L. Maron, and J. C. McWilliams. Simulations of the small scale turbulent dynamo. *The Astrophysical Journal*, 612:276–307, 2004.

[204] O. Schilling and Y. Zhou. Triadic energy transfers in non-helical magnetohydrodynamic turbulence. *Journal of Plasma Physics*, 68:389–406, 2002.

[205] J. Schou, J. Christensen-Dalsgaard, and M. J. Thompson. The resolving power of current helioseismic inversions for the Sun's internal rotation. *The Astrophysical Journal*, 385:L59–L62, 1992.

[206] M. Schüssler. Magnetic buoyancy revisited: Analytical and numerical results for rising flux tubes. *Astronomy and Astrophysics*, 71:79–91, 1979.

[207] N. Seehafer. Electric current helicity in the solar photosphere. *Solar Physics*, 125:219–232, 1990.

[208] N. Seehafer. Nature of the α effect in magnetohydrodynamics. *Physical Review E*, 53:1283–1286, 1996.

[209] K. Shibata, T. Nakamura, T. Matsumoto, K. Otsuji, T. J. Okamoto, N. Nishizuka, T. Kawate, H. Watanabe, S. Nagata, S. UeNo, R. Kitai, S. Nozawa, S. Tsuneta, Y. Suematsu, K. Ichimoto, T. Shimizu, Y. Katsukawa, T. D. Tarbell, T. E. Berger, B. W. Lites, R. A. Shine, and A. M. Title. Chromospheric anemone jets as evidence of ubiquitous reconnection. *Science*, 318:1591–1594, 2007.

[210] K. Shibata, S. Nozawa, and R. Matsumoto. Magnetic reconnection associated with emerging magnetic flux. *Publications of Astronomical Society of Japan*, 44:265–272, 1992.

[211] Y. Song and R. L. Lysak. Evaluation of twist helicity of flux-transfer event flux tubes. *J. Geophys. Res-Space Phys.*, 94:5273–5281, 1989.

[212] B. U. O. Sonnerup. Magnetopause reconnection rate. *Journal of Geophysical Research*, 79:1546–1549, 1974.

[213] A. M. Soward and S. Childress. Large magnetic Reynolds number dynamo action in a spatially periodic flow with mean motion. *Philosophical Transactions of the Royal Society of London. Series A*, 331:649–733, 1990.

[214] F. Spitzer. Some theorems concerning two dimensional Brownian motion. *Amer. Math. Soc. Trans.*, 87:187, 1958.

[215] H. C. Spruit. Motion of magnetic flux tubes in the solar convection zone and chromosphere. *Astronomy and Astrophysics*, 98:155–160, 1981.

[216] P. A. Sturrock, W. W. Dixon, J. A. Klimchuk, and S. K. Antiochos. Episodic coronal heating. *The Astrophysical Journal*, 356:L31–L34, 1990.

[217] P. A. Sturrock, P. Kaufman, R. L. Moore, and D. F. Smith. Energy release in solar flares. *Solar Physics*, 94:341–357, 1984.

[218] P. A. Sturrock and Y. Uchida. Coronal heating by stochastic magnetic pumping. *The Astrophysical Journal*, 246:331–336, 1981.

[219] K. Subramanian and A. Brandenburg. Magnetic helicity density and its flux in weakly inhomogeneous turbulence. *The Astrophysical Journal Letters*, 648:L71–L74, 2006.

[220] F. Tang. Flare morphologies and coronal field configurations. *Solar Physics*, 102:131–145, 1985.

[221] J. B. Taylor. Relaxation of toroidal plasma and generation of reverse magnetic fields. *Physical Review Letters*, 33:1139–1141, 1974.

[222] J. H. Thomas and N. O. Weiss. *Ann. Rev. Astron. Astrophys*, 42:517, 2004.

[223] J. H. Thomas, N. O. Weiss, S. M. Tobias, and N. H. Brummell. Downward pumping of magnetic flux as the cause of filamentary structures in sunspot penumbrae. *Nature*, 420:390–393, 2002.

[224] M. J. Thompson, J. Christensen-Dalsgaard, M. S. Miesch, and J. Toomre. The internal rotation of the Sun. *Annual Review of Astronomy and Astrophysics*, 41:599–643, 2003.

[225] S. M. Tobias. The solar dynamo. *Phil. Trans. R. Soc. Lond. A*, 360:2741–2756, 2002.

[226] S. M. Tobias, N. H. Brummell, T. L. Clune, and J. Toomre. Pumping of magnetic fields by turbulent penetrative convection. *The Astrophysical Journal*, 502:L177–L180, 1998.

[227] S. M. Tobias, N. H. Brummell, T. L. Clune, and J. Toomre. Transport and storage of magnetic field by overshooting turbulent compressible convection. *The Astrophysical Journal*, 549:1183–1203, 2001.

[228] T. Török and B. Kliem. The evolution of twisting coronal magnetic flux tubes. *Astronomy and Astrophysics*, 406:1043–1059, 2003.

[229] T. Török and B. Kliem. Confined and ejective eruptions of kink-unstable flux ropes. *The Astrophysical Journal*, 630:L97–L100, 2005.

[230] T. Török, B. Kliem, and V. S. Titov. Ideal kink instability of a magnetic loop equilibrium. *Astronomy and Astrophysics*, 413:L27–L30, 2004.

[231] K. C. Tsinganos. Sunspots and the physics of magnetic flux tubes. X - on the hydrodynamic instability of buoyant fields. *The Astrophysical Journal*, 239:746–760, 1980.

[232] S. I. Vainshtein, R. Z. Sagdeev, and R. Rosner. Stretch-twist-fold and ABC nonlinear dynamos: restricted chaos. *Physical Review E*, 56:1605–1622, 1997.

[233] S. I. Vainshtein, R. Z. Sagdeev, R. Rosner, and E. J. Kim. Fractal properties of the stretch-twist-fold magnetic dynamo. *Physical Review E*, 53:4729–4744, 1996.

[234] S. I. Vainshtein and Y. B. Zeldovich. Origin of magnetic fields in astrophysics. *Soviet Physics Uspekhi*, 15:159–172, 1972.

[235] G. Valori, B. Kliem, and R. Keppens. Extrapolation of a nonlinear force-free field containing a highly twisted magnetic loop. *Astronomy and Astrophysics*, 433:335–347, 2005.

[236] A. A. van Ballegooijen. Electric currents in the solar corona and the existence of magnetostatic equilibrium. *The Astrophysical Journal*, 298:421–430, 1985.

[237] A. A. van Ballegooijen. Cascade of magnetic energy as a mechanism of coronal heating. *The Astrophysical Journal*, 311:1001–1014, 1986.

[238] A. A. van Ballegooijen. Proc. ninth sacramento peak workshop on solar and coronal structure and dynamics, sunspot, New Mexico. 1987.

[239] A. A. van Ballegooijen. Photospheric motions as a source of twist in coronal magnetic fields. *Magnetic helicity in space and laboratory plasmas, Geophysical Monograph Series, ed. M. R. Brown, R. C. Canfield, A. A. Pevtsov*, 111:213–220, 1999.

[240] L. Van Driel-Gesztelyi, P. K. Manoharan, P. Démoulin, G. Aulanier, C. H. Mandrini, M. Lopez-Fuentes, B. Schmieder, S. Orlando, B. Thompson, and S. Plunkett. Initiation of CMEs: the role of magnetic twist. *Journal of Atmospheric and Solar-Terrestrial Physics*, 62:1437–1448, 2000.

[241] G. E. Vekstein and R. Jain. Signatures of a nanoflare heated solar corona. *Plasma physics and Controlled Fusion*, 45:535–545, 2003.

[242] G. E. Vekstein, E. R. Priest, and C. D. C. Steele. On the problem of magnetic coronal heating by turbulent relaxation. *The Astrophysical Journal*, 417:781–789, 1993.

[243] M. K. Verma. Field theoretic calculation of renormalized viscosity, renormalized resistivity, and energy fluxes of magnetohydrodynamic turbulence. *Physical Review E*, 64:026305–1–026305–4, 2001.

[244] M. K. Verma, A. Ayyer, and A. V. Chandra. Energy transfers and locality in magnetohydrodynamic turbulence. *Physics of Plasmas*, 12:082307–1–082307–7, 2005.

[245] L. Vlahos, M. Georgoulis, R. Kluiving, and P. Paschos. The statistical flare. *Astronomy and Astrophysics,*, 299:897–911, 1995.

[246] J. H. White. Self-linking and the Gauss integral in higher dimensions. *American Journal of Mathematics*, 91:693–728, 1969.

[247] L. M. Widrow. Origin of galactic and extragalactic magnetic fields. *Review of Modern Physics*, 74:775–823, 2002.

[248] L. Woltjer. *Proceedings of the National Academy of Sciences*, 44:833–841, 1958.

[249] A. Wright and M. A. Berger. The effect of reconnection upon the linkage and interior structure of magnetic flux tubes. *Journal of Geophysical Research*, 94:1295–1302, 1989.

[250] P. J. Xu. The genus of closed 3-braids. *Journal of knot theory and its ramifications*, 1:303–326, 1992.

[251] A. Yoshizawa, S.-I. Itoh, K. Itoh, and N. Yokoi. Dynamos and MHD theory of turbulence suppression. *Plasma Phys. Control. Fusion*, 46:R25–R94, 2004.

[252] T. A. Yousef and A. Brandenburg. Relaxation of writhe and twist of a bihelical magnetic field. *Astronomy and Astrophysics*, 407:7–12, 2003.

[253] I. Zayer, S. K. Solanki, and J. O. Stenflo. The internal magnetic field distribution and the diameters of solar magnetic elements. *Astronomy and Astrophysics*, 211:463–475, 1989.

[254] Y. B. Zeldovich, A. A. Ruzmaikin, S. A. Molchanov, and D. D. Sokoloff. Kinematic dynamo problem in a linear velocity field. *Journal of Fluid Mechanics*, 144:1–11, 1984.

[255] Y. B. Zeldovich, A. A. Ruzmaikin, and D. D. Sokoloff. Magnetic fields in astrophysics. *Gordon and Breach, New York*, 1983.

[256] J. B. Zirker and F. M. Cleveland. Avalanche models of active region heating and flaring. *Solar Physics*, 145:119–128, 1993.

[257] J. B. Zirker and F. M. Cleveland. Nanoflare mechanisms - twisting and braiding. *Solar Physics*, 144:341–347, 1993.

[258] E. G. Zweibel. Magnetohydrodynamics problems in the interstellar medium. *Physics of Plasmas*, 6:1725–1731, 1999.

[259] E. G. Zweibel and C. Heiles. Magnetic fields in galaxies and beyond. *Nature*, 385:131–136, 1997.